PONTIFÍCIA UNIVERSIDADE CATÓLICA
DO RIO DE JANEIRO

Miguel Ángel Ampuero Suárez

Topology Optimization for non-Newtonian Fluid-Flow Problems using the Virtual Element Method

Tese de Doutorado

Thesis presented to the Programa de Pós-graduação em Engenharia Mecânica of PUC-Rio in partial fulfillment of the requirements for the degree of Doutor em Ciência – Engenharia Mecânica.

Advisor   : Prof. Ivan Fábio Mota de Menezes
Co-Advisor: Prof. Juan Sergio Romero Sáenz

Rio de Janeiro
March 2020

Miguel Ángel Ampuero Suárez

Topology Optimization for non-Newtonian Fluid-Flow Problems using the Virtual Element Method

Thesis presented to the Programa de Pós-graduação em Engenharia Mecânica of PUC-Rio in partial fulfillment of the requirements for the degree of Doutor em Ciência – Engenharia Mecânica. Approved by the Examination Committee.

Prof. Ivan Fábio Mota de Menezes
Advisor
Departmento de Engenharia Mecânica — PUC-Rio

Prof. Juan Sergio Romero Sáenz
Co–Advisor
Departmento de Engenharia Mecânica — UFES

Prof. Anderson Pereira
Departamento de Engenharia Mecânica — PUC-Rio

Prof. Luiz Fernando Martha
Departamento de Engenharia Civil — PUC-Rio

Prof. Carlos Friedrich Loeffler Neto
Departamento de Engenharia Mecânica — UFES

Prof. Gláucio Hermogenes Paulino
Departamento de Engenharia Civil — GATech, EUA

Rio de Janeiro, March 17th, 2020

Miguel Ángel Ampuero Suárez

The author was born in february 17th, 1986 in Lima, Perú. In 2005, he started to study Mechanical-Electrical engineering at *Universidad Nacional de Ingeniería* (UNI), Lima-Perú, and graduated in 2010. In July 2013, he obtained the title professional of Mechanical Electrician engineer by *Colegio de Ingenieros del Perú* and in September of this year, he started his master's study in Mechanical engineering at PUC-Rio, RJ-Brazil. His master dissertation was entitled *"Topology optimization for eigenvalue problems using polygonal finite elements"* and was conducted under supervision of Prof. Ivan Menezes and Prof. Anderson Pereira. In March 2016, he started his doctoral research in applied mechanics area under supervision of Prof. Ivan Menezes (PUC-Rio) and Prof. Juan Romero (UFES). The results and contributions are presented in this work which focused in topology optimization applied to fluid-flow problems using the virtual element method (VEM).

I dedicate this work with great affection for my dear parents Paulino and Juana, my brothers Edwin and Jenifer, and my niece Fernanda, for being, my family, the great driving force that motivates me to continue.

Acknowledgments

Abstract

Ampuero Suárez, Miguel Ángel; Mota de Menezes, Ivan Fábio (Advisor); Romero Sáenz, Juan Sergio (Co-Advisor). **Topology Optimization for non-Newtonian Fluid-Flow Problems using the Virtual Element Method.** Rio de Janeiro, 2020. 89p. DSc. Thesis – Departamento de Engenharia Mecânica, Pontifícia Universidade Católica do Rio de Janeiro.

This work presents selected applications of topology optimization for non-Newtonian fluid flow problems using the virtual element method (VEM) in arbitrary two-dimensional domains. The objective is to design an optimal layout into a fluid flow domain to minimize dissipative energy governed by the Navier-Stokes-Brinkman and non-Newtonian Carreau-Yasuda model equations. The porosity approach proposed by (Borrvall and Petersson, 2003) [1] is used in the topology optimization formulation. To solve this problem numerically, the recently proposed VEM method is used. The key feature that distinguishes VEM from the standard finite element method (FEM) is that the interpolation functions in the interior of the elements do not need to be computed explicitly. This is because the integration is on lower-order polynomial and basis functions, and there is great flexibility by using a non-convex element. Therefore, the computation of the main element matrices and vectors are reduced to the evaluation of geometric quantities on the boundary of the elements. Finally, several numerical examples are provided to demonstrate the efficiency of the VEM compared to FEM and the applicability of the topology optimization to fluid flow problems.

Keywords

Topology optimization; Navier-Stokes-Brinkman equation; non-Newtonian fluids; Carreau-Yasuda model; Newton-Rapshon method; Virtual element method; Projection operators.

Resumo

Ampuero Suárez, Miguel Ángel; Mota de Menezes, Ivan Fábio (Orientador); Romero Sáenz, Juan Sergio (Coorientador). **Otimização Topológica para Problemas de Escoamento de Fluidos não Newtonianos usando o Método dos Elementos Virtuais**. Rio de Janeiro, 2020. 89p. Tese de Doutorado – Departamento de Engenharia Mecânica, Pontifícia Universidade Católica do Rio de Janeiro.

Este trabalho apresenta aplicações da técnica de otimização topológica para problemas de escoamento com fluidos não Newtonianos, usando o método dos elementos virtuais (VEM) em domínios bidimensionais arbitrários. O objetivo é projetar a trajetória ótima, a partir da minimização da energia dissipativa, de um escoamento governado pelas equações de Navier-Stokes-Brinkman e do modelo não Newtoniano de Carreau-Yasuda. A abordagem de porosidade proposta por (Borrvall e Petersson, 2003) [1] é usada na formulação do problema de otimização topológica. Para resolver este problema numericamente é usado o método VEM, recentemente proposto. A principal característica que diferencia o VEM do método dos elementos finitos (FEM) é que as funções de interpolação no interior dos elementos não precisam ser computadas explicitamente. Isso ocorre porque a integração é feita em funções polinomiais e bases de ordem inferior, permitindo assim uma grande flexibilidade no que diz respeito ao uso de elementos não convexos. Portanto, o cálculo das matrizes e vetores elementares se reduz à avaliação de grandezas geométricas nos contornos desses elementos. Finalmente, são apresentados exemplos numéricos representativos para demonstrar a eficiência do VEM em comparação com o FEM e a aplicabilidade da otimização topológica para esta classe de problemas de escoamento.

Palavras–chave

Otimização topológica; Equação de Navier-Stokes-Brinkman; Fluidos não-Newtonianos; Modelo de Carreau-Yasuda; Método de Newton-Raphson; Método dos elementos virtuais; Operadores de projeção.

Contents

List of Figures

Figure 6.16 - Optimized topologies of the horizontal channel (a) with or (b) without gravity using non-convex meshes (tess12 element).   81

List of Tables

Nomenclature

Upper-case Roman

Re	Reynolds number
E	Generic element (subset of $\mathbb{R}^n$)
∂E	Contour of the generic element
Γ_e	Domain boundaries of the element
$V_k(E)$	VEM space of order k on E
$P_k(\cdot)$	Polynomial space of order k
$[P_{k-1}(\cdot)]^2$	Polynomial vector space of order $k-1$
$H^k(\cdot)$	Sobolev spaces of order k
$C^0(\cdot)$	Space of continuous functions
Tol	Tolerance

Lower-case Roman

f_i	Load on the body
h_i	Load on the body surface
$\boldsymbol{f}$	Field strength vector applied
f	Objective function
g	Constraint function
$\partial f/\partial x$	Objective function gradient
$\partial g/\partial x$	Constraint function gradient
$(u,v)_{0,E}$	L^2-Inner product between two functions u an v defined on E
e	Generic edge of element E
x_c, y_c	Centroid of element E
$|e_i|$	Length of the ith edge e_i
$\boldsymbol{n}_i$	Normal vector of the ith edge e_i
$m_\alpha^{(k)}$	αth basis for $P_k(E)$
$\boldsymbol{m}_\alpha^{(k-1)}$	αth basis for $[P_{k-1}(E)]^2$
n_v	Dimension of $V_k(E)$
n_{p_k}	Dimension of $P_k(E)$
$n_{p_{k-1}}$	Dimension of $[P_{k-1}(E)]^2$

Lower-case Greek

$\overline{\alpha}$ Inverse permeability of the porous medium

Ω Fixed domain

$\partial\Omega$ Boundary domain

Ω_h Domain of the virtual element

Ω_e Domain of the element

ϕ_i ith shape funtion

Abbreviations

TO   Topological Optimization

NVS   Navier-Stokes

NVSB   Navier-Stokes-Brinkman

VEM   Virtual Element Method

FEM   Finite Element Method

OC   Optimality Criteria

MMA   Method of Moving Asymptotes

WRM   Weighted Residuals Methods

SFEM   Smoothed Finite Element Method

XFEM   Extended Finite Element Method

MFD   Mimetic Finite Difference

NRM   Newton-Raphson Method

LBM   Lattice Boltzmann Method

LSM   Level Set Method

WRM   Weighted Residual Methods

CVT   Centroidal Voronoi Tessellation

RND   Random Voronoi Meshes

DOFs   Degrees of freedom

"There is a driving force more powerful than steam, electricity and atomic energy: the will".

Albert Einstein.

1
Introduction

1.1
Motivation

Structural optimization problems can be classified into three types: sizing, shape, and topology optimization (Christensen and Klarbring, 2009) [17].

In sizing optimization, the shape of the structure is known, and the objective is to optimize the structure by adjusting the sizes of its components. Here, the design variables are the sizes of the structural elements, such as the diameter of a pipe or the thickness of a metal sheet. Figure 1.1(a) illustrates an example of size optimization where the diameters of the pipe elements are the design variables.

For shape optimization, the design variables are the external boundaries of the domain and/or the shapes of internal pre-existing holes. Therefore, the shape of the structure is modified in the optimization process. (See Figure 1.1(b)).
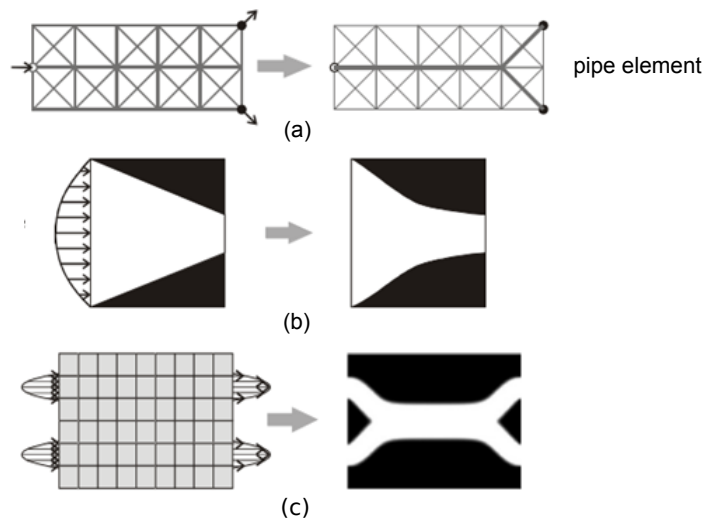
Figure 1.1: Three types of optimization: (a) sizing optimization, (b) shape optimization, and (c) topology optimization (Koga, 2010) [2].

Topology optimization is employed to find the optimal distribution of a material in a given domain, such that it minimizes specific performance measures and is subjected to a volume constraint, as illustrated in Figure 1.1(c). We emphasize that we will focus on topology optimization in this work.

In general, the optimization problem can be written as:

$$\begin{cases} \min_{\boldsymbol{x}} & f(\boldsymbol{x}), \ \boldsymbol{x} \in \mathbb{R}^n \\ \text{s.t.} & \\ & h_k(\boldsymbol{x}) = 0, \ k = 1, \ldots, m \\ & c_l(\boldsymbol{x}) \leq 0, \ l = 1, \ldots, p \\ & x_i^l \leq x_i \leq x_i^u, \ i = 1, \ldots, n \end{cases} \tag{1-1}$$

where $f(\boldsymbol{x})$ is the objective function (e.g. compliance, pressure drop, a given velocity), $h_k(\boldsymbol{x})$ and $c_l(\boldsymbol{x})$ are the equality and inequality constraints of the problem (e.g. displacements, stress, volume), $\boldsymbol{x}$ is the vector of the design variables (e.g. density of each element, viscosity), and x_i^l and x_i^u are the lower and upper bounds of the design variables, respectively.

When topology optimization is applied to fluid flow problems (e.g. the Stokes-Darcy equation), the idea is to design an optimal layout for the fluid flow in terms of a minimum value of the specified cost functional (e.g. the dissipated energy).

A strong formulation of the combined Stokes-Darcy equation, considering the applied forces on the fluid, is given by

$$\begin{cases} -\mu\nabla^2\boldsymbol{u} + \overline{\alpha}\boldsymbol{u} + \nabla p = \boldsymbol{f} \\ \nabla.\boldsymbol{u} = 0 \end{cases}, \tag{1-2}$$

where $\boldsymbol{u}$ is the velocity field, p is the pressure field, μ is the dynamic viscosity of the fluids (for Newtonian fluids, μ is constant), $\boldsymbol{f}$ is the external force field on the fluid, and $\overline{\alpha}$ is the inverse permeability of the porous medium, which allows one to model the solid and fluid regions (more details in Chapter 5.2).

A weak formulation of the problem can be obtained using the weighted residual methods (WRMs), where $\boldsymbol{v}$ and q are the velocity and pressure virtual weighting functions. From Equation (1-2), we have:

$$\begin{cases} a_\alpha(\boldsymbol{u}, \boldsymbol{v}) + b(\boldsymbol{v}, p) = l(\boldsymbol{v}), \forall \boldsymbol{u}, \boldsymbol{v} \in \boldsymbol{V} \\ b(\boldsymbol{u}, q) = 0, \ \forall q \in Q \end{cases}, \tag{1-3}$$

where

$$\begin{cases} a_\alpha(\boldsymbol{u}, \boldsymbol{v}) := -\mu \int_\Omega \nabla \boldsymbol{u} : \nabla \boldsymbol{v} d\Omega + \int_\Omega \overline{\alpha} \boldsymbol{u}.\boldsymbol{v} d\Omega \\ b(\boldsymbol{v}, p) := \int_\Omega p(\nabla.\boldsymbol{v}) d\Omega, \ b(\boldsymbol{u}, q) := \int_\Omega q(\nabla.\boldsymbol{u}) d\Omega. \\ l(\boldsymbol{v}) := \int_\Omega \boldsymbol{f}.\boldsymbol{v} d\Omega \end{cases}$$

The general formulation of the topology optimization to an incompressible Newtonian Stokes-Darcy fluid flow, neglecting external forces on the fluid, can be written as follows:

$$\begin{cases} \min_x \quad f = \frac{1}{2}\mu \int_\Omega \nabla \boldsymbol{u} : \nabla \boldsymbol{u} d\Omega + \frac{1}{2}\int_\Omega \overline{\alpha}(x)\boldsymbol{u}.\boldsymbol{u} d\Omega \\ \text{s.t.} \\ \qquad\qquad\qquad g = \int_\Omega x d\Omega - V \le 0 \\ \text{with} \\ \qquad\qquad \begin{cases} -\mu\nabla^2\boldsymbol{u} + \overline{\alpha}(x)\boldsymbol{u} + \nabla p = \boldsymbol{0} \\ \qquad\qquad\qquad \nabla.\boldsymbol{u} = 0 \end{cases}^, \\ \text{and} \\ \qquad\qquad\qquad 0 \le x \le 1. \end{cases} \qquad (1\text{-}4)$$

Here, the objective is to minimize the potential power of the Stokes-Darcy flow, expressed by the objective function f, subject to an upper bound V on the volume in the domain Ω, and x is a vector holding the design variables. This function, f, is composed of 2 terms, the first one corresponding to the dissipation due to viscous dissipative effects, while the second term corresponds to the dissipative effects of the porous media model (Koga, 2010) [2].

The Stokes-Darcy system of equations is used as a constraint in a design optimization problem, and is solved by the finite element method (FEM).

Figure 1.2 illustrates three examples of engineering applications often found in fluid mechanics literature, where the optimal layout of channel flow, minimizing drag with given velocities at the boundary, are shown as two-dimensional problems.
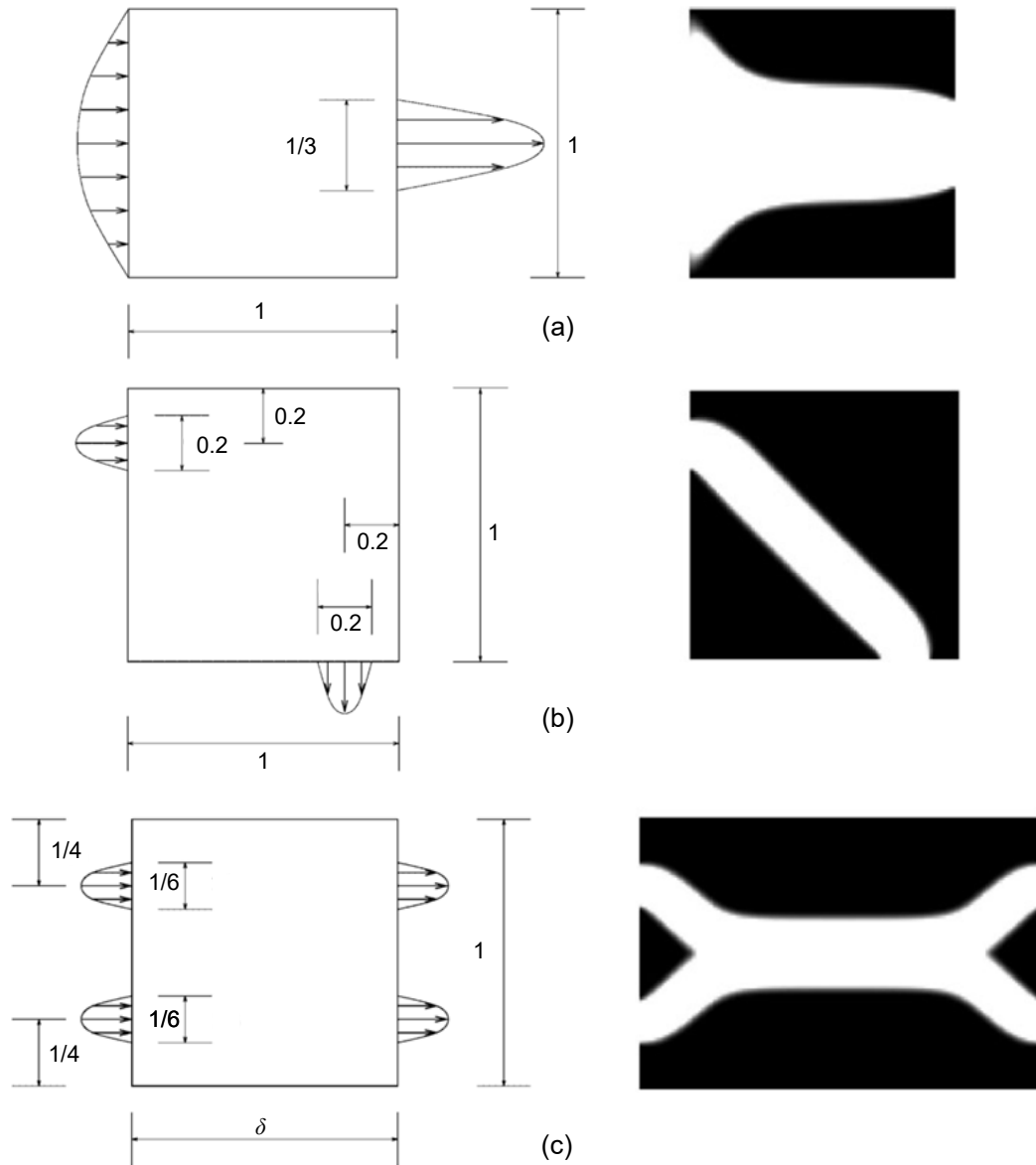
Figure 1.2: Design domain for the two-dimensional (a) diffuser, (b) pipe bends, and (c) double pipe (by $\delta >> 1$) topology optimizations, (Borvall and Petersson, 2003) [1].

We discretized the fluid flow domains into polygonal meshes. One of the main advantages of using polygonal elements is that they are naturally stable as illustrated in Figure 1.3 for a lid-driven cavity problem. As expected from the literature, the use of conventional Q4 elements leads to checkerboard layouts in the pressure field, Figure 1.3(a). However, for polygonal elements, no checkerboard patterns are observed, Figure 1.3(b)
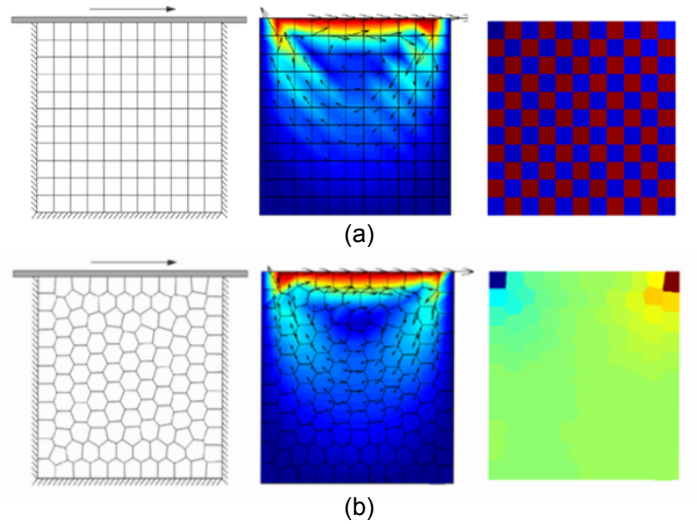
Figure 1.3: Velocity and pressure fields for a lid-driven cavity problem: (a) using Q4 elements and (b) using polygonal elements, (Talischi *et al.*, 2014) [3].

In the context of the topology optimization, we also use unstructured polygonal finite element meshes to avoid checkerboard layouts and one-node connections, (Talischi *et al.*, 2010) [18]. Figure 1.4 presents an example of topology optimization for compliance minimization using both standard regular quadrilateral elements and polygonal elements. Notice that the use of polygonal elements naturally eliminates the appearance of checkerboard patterns and one-node connections (see Pereira *et al.* (2010) [4] for more details),
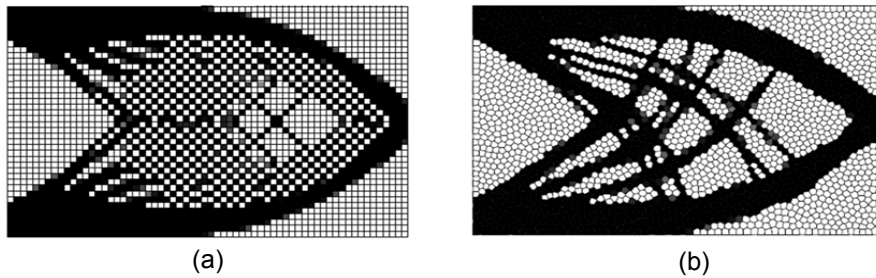
Figure 1.4: Topology optimization for compliance minimization using: (a) 2560 Q4 and (b) 2560 polygonal elements, [4].

The constrained geometry of the discretizations associated with standard triangles and quads can cause bias in the orientation of members, leading to mesh-dependent (sub-optimal) topology optimization designs. Figure 1.5 shows that this problem can be easily circumvented by using polygonal element meshes.
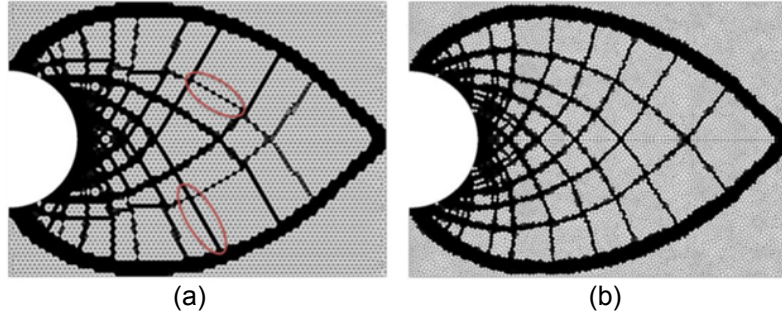
Figure 1.5: Topology optimization applied to the Michell domain cantilever problem; (a) using T6 elements and (b) using polygonal elements.

Recent literature, such as Talischi *et al.* (2016) [5], shows the effectiveness in the solution of topology optimization using polygonal elements for fluid problems solved with FEM and implemented with the educational computer code `Polytop`, [19]. Figure 1.6 illustrates a typical example of the diffuser problem for the minimization of dissipative energy on a Newtonian fluid governed by the Stokes-Darcy flow equations, neglecting external forces on the fluid.
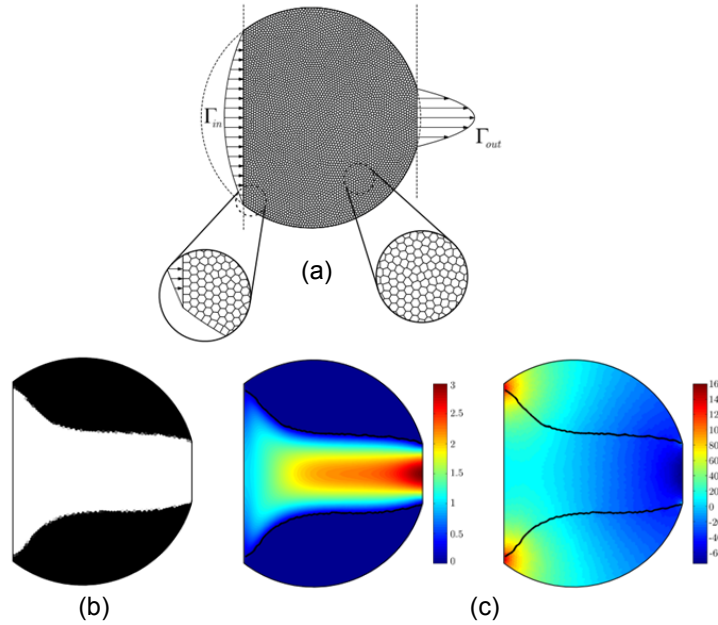
Figure 1.6: Solution to the diffuser problem. (a) Geometry and boundary condition using polygonal meshes, (b) optimal solution, and (c) velocity and pressure fields [5].

Virtual element method

"The Virtual element method (VEM) is a recent generalization of the Finite Element Method which is characterized by the capability of dealing with very general polygonal/polyhedral meshes and the possibility to easily

implement highly regular discrete spaces," (Beirão da Veiga et al., 2015) [20]. Some of the main advantages are that VEM does not use basis functions explicitly (so there is no need for numerical integration in the domain), only depends on the geometry's contour, and the domain can be discretized using convex and non-convex polygonal elements. These features offer significant flexibility to solve numerical problems in complex bi-dimensional domains with difficult mesh generation and can integrate into the topology optimization problem, resulting in very attractive computational performance

We remark that the main steps of the VEM solution is similar to the standard FEM solution (see Figure 1.7).
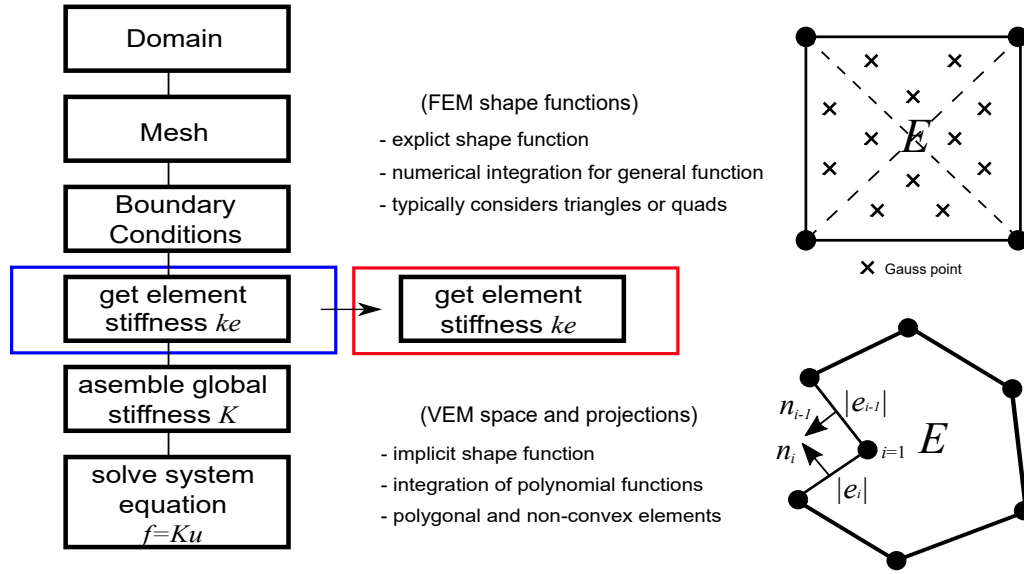
Figure 1.7: Main FEM-VEM differences on the standard solution implementation.

An interesting problem is taken from the work of (Torres, 2016) [6]. It consists of a comparative study of three numerical methods, VEM, FEM and smoothed FEM (SFEM), applied to solve elasticity problems in the context of topological optimization. A correction was made to the numerical integration of the FEM in polygonal meshes, increasing from 3 to 7 points per triangle to achieve the convergence level shown in Figure 1.8(a). Although a higher computational cost is observed (see Figure 1.8(b)) a good monotonic convergence is achieved.
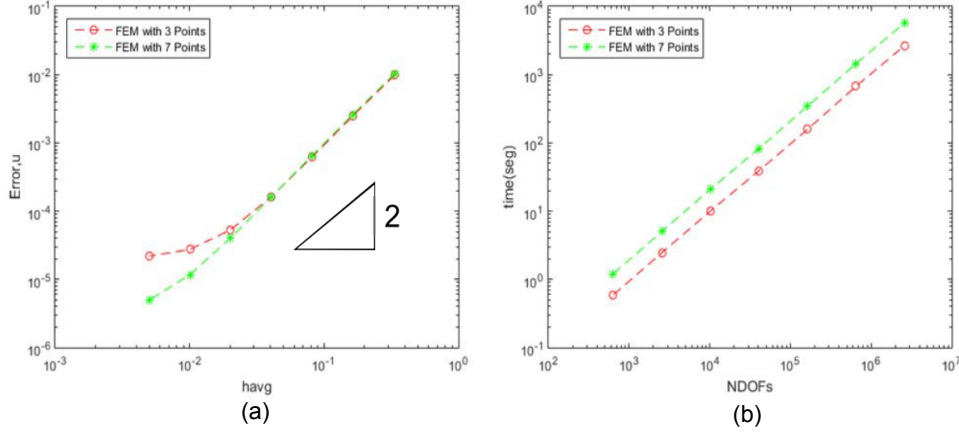
Figure 1.8: Convergence of the FEM with 3 (a) and 7 (b) integration points [6].

The performance of each numerical method is presented in Figure 1.9(a). Figure 1.9(b) shows the computational time for assembling the global stiffness matrix of each method. It is clear from Figure 1.9 that the VEM has proven to be very efficient in solving elasticity problems using polygonal meshes when compared to FEM and smoothed FEM.
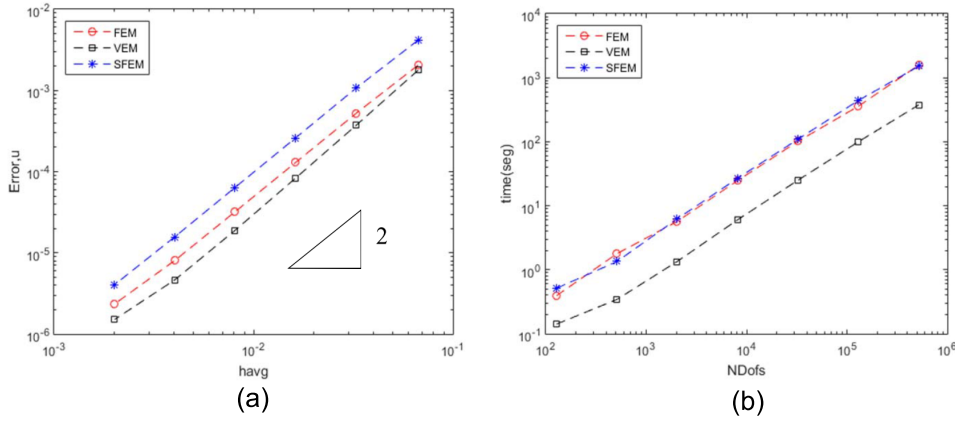
Figure 1.9: (a) Convergence of each method using polygonal meshes and (b) computational cost [6].

In the work of (Sutton, 2017) [7], the results of the VEM numerical solution of the classical Poisson problem using both discretized domains (convex and non-convex elements) were shown and the flexibility and efficiency of this method compared with the standard FEM was proven.

The strong formulation of the two-dimensional *Poisson problem* is written as follows:

$$\begin{cases} -\nabla^2 \boldsymbol{u} = \boldsymbol{f} \text{ in } \Omega \\ \quad \boldsymbol{u} = \boldsymbol{g} \text{ on } \partial\Omega \end{cases},$$

where the boundary, g, and loading function, f, are defined as:

$g = (1 - x)ysin(\pi x)$ and $f = 15sin(\pi x)sin(\pi y)$.

Figure 1.9 shows the numerical solution obtained using VEM in a square domain of 1x1 discretized with Voronoi-polygonal elements (Figure 1.10(a)), triangle and quad elements (Figure 1.10(b)), and non-convex elements (Figure 1.10(c)).
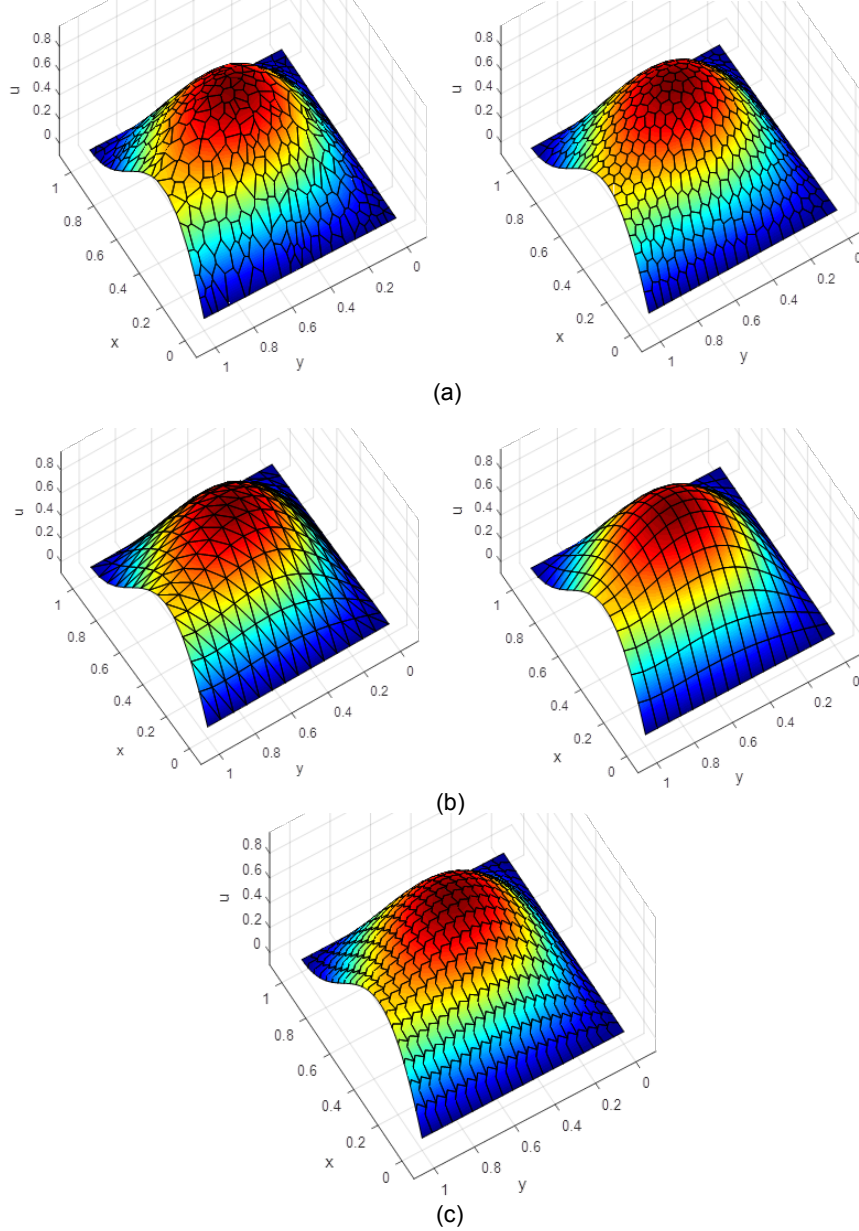
Figure 1.10: VEM numerical solution for the two-dimensional Poisson problem.(a) Voronoi-polygonal, (b) triangle & quads, and (c) non-convex elements [7].

Paulino and Gain [8] show numerical results in topology optimization for the elasticity problem by minimizing a compliance function subject to a

volume constraint using the VEM. Figure 1.11 illustrates the results of the optimal topology in different domains using non-convex elements.
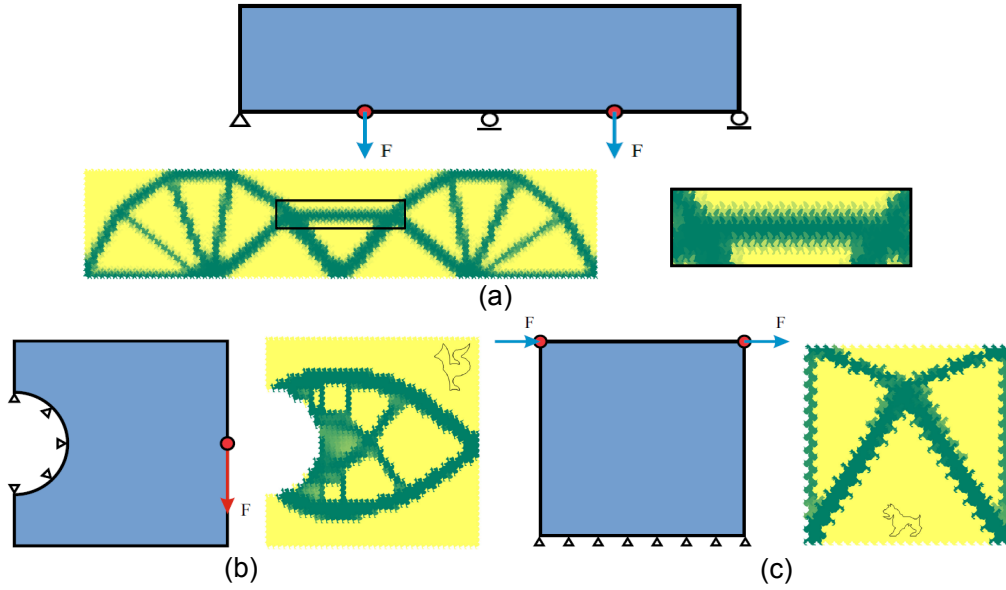
Figure 1.11: Two-dimensional linear elastic topology optimization examples using VEM method (by non-convex elements). (a) Bridge ,(b) cantilever beam, and (c) bracing system problem [8].

Recently, works on topology optimization were extended by non-Newtonian fluid flow problems using several numerical solvers such as FEM, the Lattice Boltzmann method (LBM), and the finite volume method (FVM). Detailed descriptions of previous work can be found in Chapter 1.2.

In summary, our contribution in this work is to provide detailed procedures of the proposed VEM method implemented in MATLAB® using lower-order elements, to solve non-Newtonian and incompressible Navier-Stokes-Brinkman (NVSB) differential equations, the Carreau-Yasuda equation, as a model of the non-Newtonian fluid, and to make a study of the convergence analysis of VEM and FEM. Further, we will compare the performance of these two methods with respect to computational efficiency. We will prove that the proposed VEM is a better solver that could be integrated into topology optimization for fluid flow problems. We will present several examples of two-dimensional fluid flow problems, which are available in the literature, to demonstrate the functionality and applicability of the proposed methodology.

Some relevant comments about VEM

The computation of the projection operator (see Section 3 for more details) can be computationally expensive, in particular, when variables such as

displacement, velocity, pressure fields, etc., are approximated with high-order functions (*i.e.*, $k \geq 2$).

Figure 1.11 shows element VEM spaces and degrees of freedom (DOF) using quadratic ($k = 2$) and cubic ($k = 3$) elements, (Beirão *et al.*, 2014 [9].)
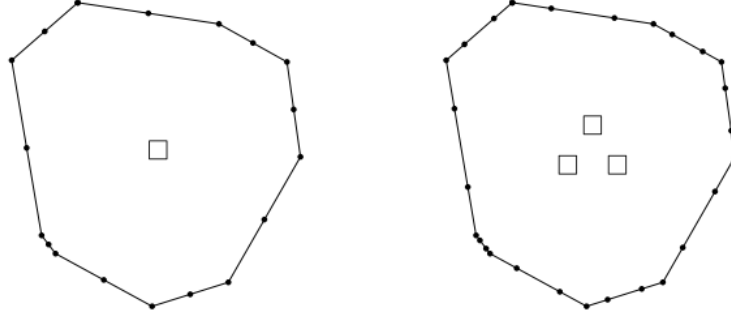
Figure 1.12: Element VEM spaces and degrees of freedom for $k = 2$ (left) and $k = 3$ (right), (Taken from: [9]).

From the strong formulation of the Poisson problem (Eq. (1-3)), it can be written in the weak formulation as follow:

$$a(\boldsymbol{u}, \boldsymbol{v}) := - \int_{\Omega} \nabla \boldsymbol{u} : \nabla \boldsymbol{v} d\Omega = \int_{\Omega} \boldsymbol{f}.\boldsymbol{v} d\Omega := l(\boldsymbol{v}). \qquad (1\text{-}5)$$

From Eq. (1-5), in the VEM method, the element level approximation is expressed as:

$$a_h^E := \underbrace{\int_E \Pi_E^0 \nabla \boldsymbol{u}_h \Pi_E^0 \nabla \boldsymbol{v}_h d\boldsymbol{x}}_{consistency} + \underbrace{\alpha S(\boldsymbol{u}_h - \Pi_E^\nabla \boldsymbol{u}_h, \boldsymbol{v}_h - \Pi_E^\nabla \boldsymbol{v}_h)}_{stability}, \qquad (1\text{-}6)$$

where the first and second term are called as consistency and stability term and Π_E^0 and Π_E^∇ are called as first and second virtual projection operators, respectively, (for more details see Chapter 3). In this problem, the value of the stability factor α is 1.

Therefore, in some cases we need to adjust this stability factor. As an example (taken from the work of Torres 2016 [6]), we show a typical cantilever problem, illustrated in Figure 1.13, where we want to obtain the maximum displacements, u, using the VEM. The governing equations of this problem are:

$$\begin{cases} \int_{-b}^{b} \sigma_{xy} dy = F \; ; x = 0 \\ \sigma_{xy} = \dfrac{3F(b^2 - y^2)}{4b^3} \end{cases},$$

and the analytical solution is given as:
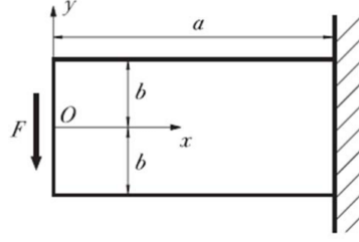
Figure 1.13: Geometry and boundary conditions of the cantilever beam problem with end loading,[10].

$$
\begin{cases}
u_x = \dfrac{3Fx^2y}{4Eb^3} + \dfrac{3F(1+\nu)y}{2Eb} + \dfrac{F(2+\nu)y^3}{4Eb^3} + A - Cy, \\
\qquad u_y = \dfrac{3F\nu xy^2}{4Eb^3} - \dfrac{Fx^3}{4Eb^3} + B + Cx
\end{cases}.
$$

with $u_x = 0; u_y = 0; \frac{\partial u_y}{\partial x} = 0;$ in $x = a, y = 0$, (taken from (Barber,2009 [10])). The author conducted a study to select the optimal stability factor by comparing with the minimum relative error of the FEM and VEM with respect to the analytical solution (see Figure 1.14). The author presented a semi-logarithmic graph of the norm error vs. stability factor, α, for a given number of polygonal elements in VEM and FEM. In this problem, the minimum norm error was obtained using a coefficient of $\alpha = 0.15$; therefore, the element stiffness matrix was adjusted with this factor.
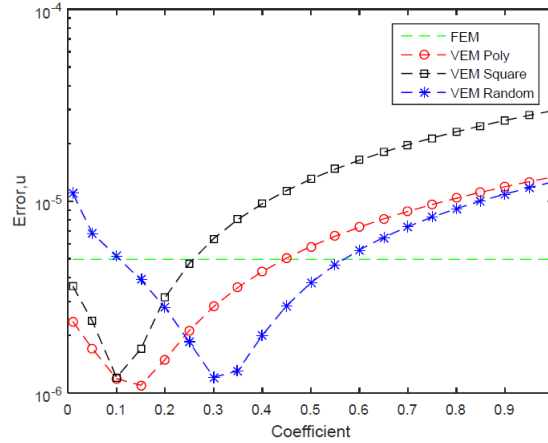
Figure 1.14: Stability factor analysis extracted from [6].

Based on previous works on virtual element applied for elastic problem (Artioli *et al.,* 2017, [21]), the parameter, α, is recommended to be selected as one-half of the trace of the consistent tangent matrix, *i.e.,* $tr(K)$. For VEM-inelastic problems, the choice of the parameter is equal to the trace of the consistent part of the stiffness matrix K, multiplied by a factor that is a

function of the poisson's ratio (ν). According to Taylor and Artioli, 2018 [22], the factor α is given as:

$$\alpha = \frac{3}{4} tr(K) \frac{1 - 2\nu}{1 + \nu}.$$

1.2
Previous work

The method of topology optimization for fluid flow problems first appeared in the literature in 2003. It was originally studied by Borrvall and Petersson [1], where numerical examples for the optimal layout of channel flows with minimized viscous drag, combining the Stokes and Darcy law equations considering laminar flow condition are presented in his works. Gersborg-Hansen *et al.* (2005) [23] applied topology optimization for microfluidic channel-layout problems and microelectromechanical device design, considering low Reynold numbers. They used the FEM to solve this numerical problem. Guest and Prévost (2006) [24] extended that work by introducing the stabilized FEM (Burman and Hansbo, (2007) [25]) to solve the Stokes-Darcy differential equation.

Until then, the inverse permeability material model was used as a design variable parameter by defining solid or fluid regions in the fluid domain. Wiker *et al.* (2007) [26] extended the viscosity as a dependent parameter of the design variables, where he presented numerical examples as channels in a tree-shaped structured that solved pure Darcy and Stokes-Darcy equations. Further, the gradient method was used in topology optimization with known optimizers such as optimality criteria (OC) and method of moving asymptotes (MMA). Challis and Guest (2009) [27] reported the level set method (LSM) (Wang *et al.,* (2007) [28]) to solve Stokes-Darcy topology optimization problems. Classic examples of the bi-dimensional domains, such as a diffuser, double-triple pipe, bend pipe, and manifolds optimization, were extended to three-dimensional optimization problems.

Topology optimization applied to Stokes-Darcy fluid flow problems has attracted interest from researchers, who have expanded their work to steady Navier-Stokes-Brinkman flow problems. Okkels *et al.* (2005) [29] presented micro-nanofluidic systems optimal designs, and Olesen *et al.* (2005) [30] studied and presented numerical examples of channels with reversed flow. Deng *et al.* (2011) [31] reported unsteady NVSB equations with low and moderate Reynolds numbers using FEM and integrated topology optimization problems and reproduced classical examples presented by (Borvall and Peterson)[1].

Kreissl *et al.,* (2011) [32],[33] studied a different way to approximate

the solution of the NVSB equation by applying the hydrodynamic Lattice Boltzmann method (LBM) (Chen and Doolen, 1998) [34] and applied steady and unsteady fluid flow problems. Then, they presented numerical results of NVSB optimal topology optimization problems using both LBM and LSM. A multiphase flow problem was studied by Kreissl and Maute (2012) [35], where they solved the problem by using the extended FEM (XFEM) (Chessa and Belytschko, 2003) [36], which is an attractive method for modeling discontinuous elements and combined topology optimization problems.

Deng *et al.*, (2013) [37], [38] reproduced topology optimization fluid flow problems considering external body forces on the fluid, such as gravitational, centrifugal, and Coriolis forces.

Authors such as (Romero and Silva, 2014) [39] and (L.F.N. Sá *et al.*, 2017) [40] extended the NVSB equation considering vorticity in the formulation. They presented the optimal design of a machine rotor (pump and turbine models).

Polygonal elements have been used by Pereira *et al.*, (2016) [5] on the FEM solution of the Stokes-Darcy problems. They compared and reproduced classical examples presented by (Borvall and Petersson, 2003 [1]) and demonstrated the effectiveness of the polygonal meshes on topology optimization fluid flow problems.

The Navier-Stokes-Brinkman equation was extended to consider a non-Newtonian fluid, solved with FEM, and used in the topology optimization method. Authors such as (Pingen and Maute, 2010) [11] used the Carreau-Yasuda formulation to model the non-Newtonian fluid; (Hyun *et al.*, 2014) [41] applied it to fluidic systems minimizing wall shear stress; (Zhang and Liu, 2015) [42] studied optimal arterial bypass configurations; (Zhang *et al.*, 2016) [43] extended it by using the power-law model as a non-Newtonian fluid; and (Romero and Silva, 2017) [44] reproduced applications of optimal flow machine rotor design by non-Newtonian fluid.

Recently, the VEM has attracted the interest of a diverse range of authors, and they have successfully applied VEM to solve numerically different problems, such as the elasticity problem. These authors include (Beirão da Veiga *et al.*, 2013) [45], (Gain et al., 2014) [46], (E. Artioli *et al.*, 2017) [47],[21] and (Chi *et al.*, 2017) [48]). VEM was used to solve the plate bending problem in (Brezzi and Marini, 2013) [49], the contact between two elastic bodies problem in (Wriggers *et al.*, 2016) [50], spectral problems in (Rivera and Mora, 2018) [51], cracking analysis in (Benedetto *et al.*, 2018) [52]. Fluid flow problems were tackled, using VEM, by (Sutton, 2017) [7] to solve the Poisson's equation, whereas (Antonietti *et al.*, 2014) [53], (Cangiani *et al.*, 2016) [54],

(Beirão da Veiga and Lovadina, 2017) [55], and (Ernesto and Gatica, 2017) [56] solved the Stokes-Darcy equation, and (Beirão da Veiga *et al.,* 2018) [57] solved the Navier-Stokes-Brinkman equation.

From topology optimization, VEM was used to solve two- and three-dimensional elasticity problems. Authors such as (Paulino and Gain, 2015) [8], (Gain *et al.,* 2015) [58], and (P.F. Antonietti *et al.,* 2016) [59], reproduced and compared VEM with FEM, and optimized structure design by minimizing compliance using non-convex elements.

Suárez *et al.*, 2018 [14] extended Stokes-Darcy topology optimization problems using VEM and lower-order elements, and reproduced examples presented by Borvall and Petersson, (2003) [1] and Pereira *et al.,* (2016) [5]. In this work, the author extended the non-Newtonian Navier-Stokes-Brinkman equation, using VEM and lower-order elements, with focus on topology optimization for fluid flow problems using Carreau-Yasuda to model the non-Newtonian fluid (Suárez et al.) [16].

1.3
Objectives of this thesis

The main objective of this thesis is to present several applications of topology optimization for fluid flow problems, specifically for incompressible non-Newtonian fluids governed by the Navier-Stokes-Brinkman and Carreau-Yasuda equations, using the VEM and lower-order elements in arbitrary two-dimensional domains.

The specific objectives are:

1. To develop a numerical solution for fluid flow problems using the VEM and to present some comparative studies with respect to its computational efficiency.

2. To solve topology optimization problems for representative numerical examples available in the literature.

1.4
Outline of this thesis

The remainder of this thesis is organized in seven chapters as follows: Firstly, Chapter 1 comprises this introduction. In Chapter 2, the theoretical background regarding the Navier-Stokes-Brinkman equation and Carreau-Yasuda model (non-Newtonian fluid) are briefly presented together with some theoretical background on the FEM. In the final subsection of Chapter 2, we show a verification of the FEM method by comparing results

with the literature. In Chapter 3, the VEM is explained in more detail and we present the main equations, matrices, and vectors of this method. In Chapter 4, convergence analysis examples are presented for both the FEM and VEM and we show the efficiency of this method for Newtonian and non-Newtonian (using the Carreau-Yasuda model) fluids in the NVSB problem. In Chapter 5, we describe the topology optimization method applied to non-Newtonian fluid flow. In chapter 6, we discuss the results obtained using several representative numerical examples available in the literature. Finally, in Chapter 7, we summarize the conclusions of this work and present suggestions and directions for future work.

2
Fluid flow problems

In this chapter, we briefly discuss the basic issues that are related to the computational steps to solve the Navier-Stokes-Brinkman equation for non-Newtonian fluids using the Carreau-Yasuda model. The domain is discretized based on the FEM, and we present the main vectors, matrices, and equations associated with these problems.

2.1
Navier-Stokes-Brinkman equation

The steady-state strong formulation of the Navier-Stokes-Brinkman equation (Gartling *et al.,* 2007) [60] is expressed as:

$$\begin{cases} -\eta(\dot{\gamma})\nabla^2\boldsymbol{u} + \overline{\alpha}\boldsymbol{u} + \nabla p + \rho\boldsymbol{u}.\nabla\boldsymbol{u} = \boldsymbol{f}, \text{ in } \Omega \\ \nabla.\boldsymbol{u} = 0 \\ \boldsymbol{u} = \boldsymbol{g}, \text{ on } \partial\Omega \end{cases} \tag{2-1}$$

where the first equation is due to the conservation of linear momentum and the second equation comes from the conservation of mass, where, considering general viscosity equation for non-Newtonian fluid, $\eta(\dot{\gamma})$ is a function dependent on the fluid velocity gradients $\nabla\boldsymbol{u}$, (more details in Section 2.1.1), ρ is the density of the fluid, $\overline{\alpha}$ is the inverse permeability of the porous medium, $\boldsymbol{u}$ the velocity field, p is the pressure field, and $\boldsymbol{f}$ is the external force field on the fluid (e.g., gravity, centrifugal and Coriolis forces, etc.).

Some important remarks regarding Equation (2-1): in the Stokes-Darcy problem, the non-linear term is neglected, (i.e., $\boldsymbol{u}.\nabla\boldsymbol{u} \approx 0$), the viscosity behavior is considered as Newtonian fluid, i.e., $\eta = \mu = cte$, and the parameter $\overline{\alpha}$ allows for the determination of the solid/fluid regions in domain Ω (more details are available in Chapter 5.2).

From Eq. (2-1), using the WRMs, the weak formulation expressed in bilinear form is:

$$\begin{cases} a(\boldsymbol{u}, \boldsymbol{v}) + a_\alpha(\boldsymbol{u}, \boldsymbol{v}) + b(\boldsymbol{v}, p) + c(\boldsymbol{w}; \boldsymbol{u}, \boldsymbol{v}) = l(\boldsymbol{v}), \forall \boldsymbol{u}, \boldsymbol{v}, \boldsymbol{w} \in \boldsymbol{V} \\ \qquad\qquad\qquad\qquad b(\boldsymbol{u}, q) = 0, \ \forall \boldsymbol{u} \in \boldsymbol{V}, \ \forall q \in Q \end{cases}, \quad (2\text{-}2)$$

where

$$\begin{cases} a(\boldsymbol{u}, \boldsymbol{v}) := -\int_\Omega \eta(\dot{\gamma}) \nabla \boldsymbol{u} : \nabla \boldsymbol{v} d\Omega, \ a_\alpha(\boldsymbol{u}, \boldsymbol{v}) := \int_\Omega \overline{\alpha} \boldsymbol{u}.\boldsymbol{v} d\Omega \\ \qquad b(\boldsymbol{v}, p) := \int_\Omega p(\nabla.\boldsymbol{v}) d\Omega, \ b(\boldsymbol{u}, q) := \int_\Omega q(\nabla.\boldsymbol{u}) d\Omega, \\ \qquad c(\boldsymbol{w}; \boldsymbol{u}, \boldsymbol{v}) := \rho \int_\Omega (\nabla \boldsymbol{u}) \boldsymbol{w}.\boldsymbol{v} d\Omega, \ l(\boldsymbol{v}) := \int_\Omega \boldsymbol{f}.\boldsymbol{v} d\Omega \end{cases}$$

$\boldsymbol{v}$ and q are the velocity and pressure virtual weighting functions, respectively, and the solution $(\boldsymbol{u}, p) \in \boldsymbol{V} \times Q$ $a : \boldsymbol{V} \times \boldsymbol{V} \to \mathbb{R}, a_\alpha : \boldsymbol{V} \times \boldsymbol{V} \to \mathbb{R}, b : \boldsymbol{V} \times Q \to \mathbb{R}, c : \boldsymbol{V} \times \boldsymbol{V} \times \boldsymbol{V} \to \mathbb{R}, l : \boldsymbol{V} \to \mathbb{R}$, respectively.

The velocity field, u_i, and pressure field, p, are approximated by a linear combination of the basis functions of the form

$$\begin{cases} u_i(\boldsymbol{x}) = \sum_{j=1}^{N} \phi_n(\boldsymbol{x}) u_i^n = \boldsymbol{\phi}^T \boldsymbol{u}, \ i = 1, 2 \\ \qquad p(\boldsymbol{x}) = \sum_{j=1}^{M} \chi_m(\boldsymbol{x}) p_m = \boldsymbol{\chi}^T \boldsymbol{p} \end{cases}, \quad (2\text{-}3)$$

where, $\boldsymbol{u}$ and $\boldsymbol{p}$ are vectors with nodal values of the components of velocity and pressure, respectively, and $\boldsymbol{\phi}$ and $\boldsymbol{\chi}$ are the vectors' interpolation function, respectively.

Substituting Eq.(2-3) into (2-2) we can re-write the formulation as follows:

$$\begin{cases} \boldsymbol{C}(\boldsymbol{u})\boldsymbol{u} + \boldsymbol{K}_\eta \boldsymbol{u} + \boldsymbol{K}_\alpha \boldsymbol{u} - \boldsymbol{Q}\boldsymbol{p} = \boldsymbol{F} \\ \qquad\qquad\qquad\qquad -\boldsymbol{Q}^T \boldsymbol{u} = 0 \end{cases}, \quad (2\text{-}4)$$

where, the expression of the main elementary matrices and vectors are:

$$\begin{cases} [\boldsymbol{K}_\eta]_{ij} = \int_{\Omega_e} \eta(\dot{\gamma}) \frac{\partial \boldsymbol{\phi}}{\partial x_i} \frac{\partial \boldsymbol{\phi}}{\partial x_j}^T dx, \ [\boldsymbol{K}_\alpha]_{ij} = \int_{\Omega_e} \overline{\alpha} \boldsymbol{\phi} \boldsymbol{\phi}^T dx \\ \qquad \boldsymbol{C}_j(\boldsymbol{u}_j) = \rho \int_{\Omega_e} \boldsymbol{\phi} \left(\boldsymbol{\phi}^T \boldsymbol{u}_j \right) \frac{\partial \boldsymbol{\phi}}{\partial x_j}^T dx, \ i, j = 1, 2., \\ \boldsymbol{Q}_i = \int_{\Omega_e} \frac{\partial \boldsymbol{\phi}}{\partial x_i} \boldsymbol{\chi}^T dx, \ \boldsymbol{F}_i = \int_{\Omega_e} \rho \boldsymbol{\phi} f_i dx + \oint_{\Gamma_e} h_i \boldsymbol{\phi} ds \end{cases} \quad (2\text{-}5)$$

and in the global matrix form, is expressed as:

$$\underbrace{\begin{bmatrix} C(\boldsymbol{u}) + \boldsymbol{K} & -\boldsymbol{Q} \\ -\boldsymbol{Q}^T & 0 \end{bmatrix}}_{\tilde{\boldsymbol{K}}} \underbrace{\begin{bmatrix} \boldsymbol{u} \\ \boldsymbol{p} \end{bmatrix}}_{U} = \underbrace{\begin{bmatrix} \boldsymbol{F} \\ \boldsymbol{0} \end{bmatrix}}_{\tilde{\boldsymbol{F}}}, \text{ with } \boldsymbol{u} = [\boldsymbol{u}_1, \boldsymbol{u}_2]^T \text{ and } \boldsymbol{K} = \boldsymbol{K}_\eta + \boldsymbol{K}_\alpha.$$

(2-6)

From Eq. (2-6), $\tilde{\boldsymbol{K}}$ is symmetric and is known as system stiffness matrix. The resulting nonlinear systems equation, $\tilde{\boldsymbol{K}}(\boldsymbol{U})\boldsymbol{U} = \tilde{\boldsymbol{F}}$, is solved using the Newton-Raphson method (NRM) (Burden and Faires, 2000) [61] as follows. First, we define the residual vector, $\boldsymbol{R}$, as:

$$\boldsymbol{R}(\boldsymbol{U}) = \tilde{\boldsymbol{K}}(\boldsymbol{U})\boldsymbol{U} - \tilde{\boldsymbol{F}} = \boldsymbol{0}. \qquad (2\text{-}7)$$

Using the first-order Taylor expansion, $\boldsymbol{R}$ is expressed as:

$$\boldsymbol{R}(\boldsymbol{U}) = \boldsymbol{R}(\boldsymbol{U}^n) + \left.\frac{\partial \boldsymbol{R}}{\partial \boldsymbol{U}}\right|_{\boldsymbol{U}^n} \Delta \boldsymbol{U} + \cdots = \boldsymbol{0},$$

then,

$$\boldsymbol{R}(\boldsymbol{U}^n) = -\left.\frac{\partial \boldsymbol{R}}{\partial \boldsymbol{U}}\right|_{\boldsymbol{U}^n} (\Delta \boldsymbol{U}) = -\boldsymbol{J}(\boldsymbol{U}^n)(\boldsymbol{U}^{n+1} - \boldsymbol{U}^n).$$

The matrix $\boldsymbol{J}$ is known as the Jacobian matrix and the solution is expressed as:

$$\boldsymbol{U}^{n+1} = \boldsymbol{U}^n - \boldsymbol{J}^{-1}(\boldsymbol{U}^n)\boldsymbol{R}(\boldsymbol{U}^n), \qquad (2\text{-}8)$$

where, $\boldsymbol{U}^{n+1} = [\boldsymbol{u}_1, \boldsymbol{u}_2, \boldsymbol{p}]^T$ are the unknown velocity and pressure vectors. The respective algorithm steps are shown in Algorithm 1.

Algorithm 1 : Newton-Rapshon method

1: **Initialization:** given $\boldsymbol{U} = \boldsymbol{U}^n$;
2: **while** $|\boldsymbol{R}(\boldsymbol{U}) < Tol|$ **do**
3:     $\boldsymbol{J}\Delta\boldsymbol{U} = -\boldsymbol{R}$;
4:     $\boldsymbol{U}^{n+1} = \boldsymbol{U}^n + \Delta\boldsymbol{U}$
5: **end while**

More details about the formulations of the residual vector $\boldsymbol{R}(\boldsymbol{U})$ and Jacobian matrix $\boldsymbol{J}(\boldsymbol{U})$ (Eq. (2-5)) are given in the work by (Suárez et $al.$) [16]. After obtaining the residual vector, $\boldsymbol{R}$, and matrix, $\boldsymbol{J}$, we use Eq. (2-8) to solve the non-linear Navier-Stokes-Brinkman equation. The flowchart solution is presented in Figure 2.1.
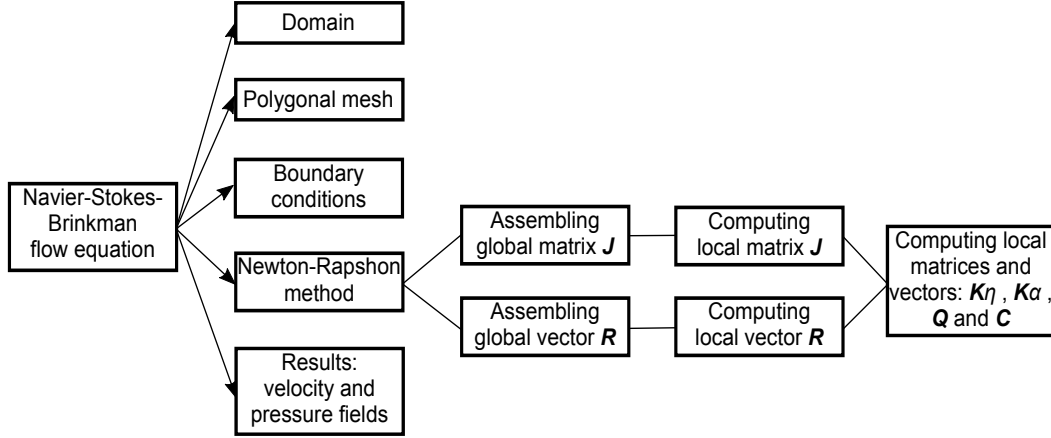
Figure 2.1: General flowchart for the solution of the Navier-Stokes-Brinkman flow equation using Newton-Raphson method.

In Chapter 3, we will show how compute the main elementary matrices and vectors shown in Eq. (2-5) with focus on the VEM.

The main references of this section is Carvalho and Valerio, (2012) [62].

2.1.1
Carreau-Yasuda model for a non-Newtonian fluid

Generalized Newtonian models are used to describe permanent shear flows; they describe non-Newtonian viscosity, but not the effects of normal stress, time-dependent effects, or elastic effects. At present, it is widely used in industry. Non-Newtonian viscosity and its enormous variation with the shear rate is central to the description of flows of interest.

In general, for an incompressible fluid, the viscous stress tensor ($\boldsymbol{\tau}$) is expressed as:

$$\boldsymbol{\tau} = 2\eta(\dot{\gamma})\boldsymbol{D}, \tag{2-9}$$

where $\boldsymbol{D} = \frac{1}{2}(\nabla\boldsymbol{U} + \nabla\boldsymbol{U}^T)$ is the strain-rate tensor. For the particular Newtonian fluid case, the viscosity has a constant behavior, ($i.e., \eta = \mu = cte$), see Figure 2.2 .

The generalized non-Newtonian viscosity $\eta(\dot{\gamma})$ is obtained from empirical relations, the simplest relation for $\eta(\dot{\gamma})$ is the expression known as the power-law, expressed as

$$\eta(\dot{\gamma}) = m\dot{\gamma}^{n-1},$$

that depends on two parameters, where m and n are constants that characterize the fluid. This simple relationship describes the non-Newtonian viscosity curve in the log-log viscosity diagram versus shear rate for many materials. A better fit can be obtained using the Carreau-Yasuda model.

In this work, we focus on non-Newtonian fluid flow and we use the Carreau-Yasuda model, for being one of the most used model in the literature

([11], [13], [63] and [64]), where the viscosity, η, is a function of the shear rate, $\dot{\gamma}$, as:

$$\eta(\dot{\gamma}) = \eta_\infty + (\eta_0 - \eta_\infty)[1 + (\lambda\dot{\gamma})^a]^{\frac{n-1}{a}}, \qquad (2\text{-}10)$$

where the main parameters for this model are: η_0, η_∞ (max-min value of viscosity η), n is the power law exponent, and λ, a are dimensionless numbers. Depending on the type of fluid, these parameters can vary and are obtained experimentally. According to Cho and Kenssey (1991) [63] and Pingen and Maute (2010) [11], for blood, the constants in the Carreau-Yasuda model are $\lambda = 1.902s$, $n = 0.22$, $a = 1.5$, $\eta_0 = 0.056$, and $\eta_\infty = 0.00345$Pa-s. Figure 2.2 shows the behavior of the blood viscosity using the Carreau-Yasuda model.
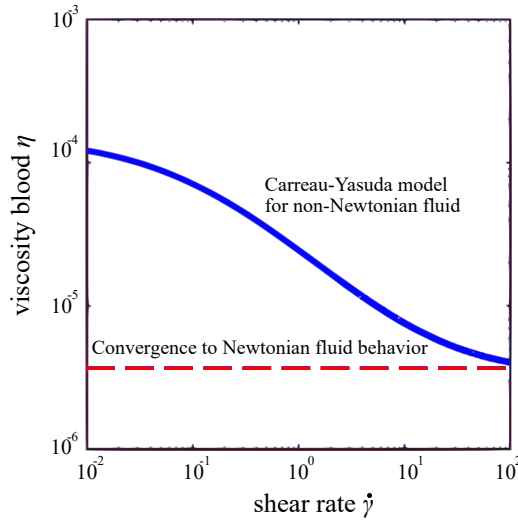
Figure 2.2: Log-log plot of the viscosity vs. shear rate for blood fluid flow using the Carreau-Yasuda model. Extracted from (Pingen and Maute, 2010) [11].

The magnitude of the shear rate, $\dot{\gamma}$, is expressed as

$$\dot{\gamma} = \sqrt{2\left[D_{11}^2 + D_{22}^2 + 2D_{12}^2\right]} =$$
$$\sqrt{2\left(\frac{\partial \boldsymbol{u}_1}{\partial x}\right)^2 + 2\left(\frac{\partial \boldsymbol{u}_2}{\partial y}\right)^2 + \left(\frac{\partial \boldsymbol{u}_1}{\partial y} + \frac{\partial \boldsymbol{u}_2}{\partial x}\right)^2}. \qquad (2\text{-}11)$$

and is substituted in Eq. (2-10).

Consideration:*Sensitivity analysis of the fluid viscosity*

For a non-Newtonian fluid, from Equation (2-7), the expression of the Jacobian matrix, $\boldsymbol{J}$, must be re-formulated by considering the sensitivity of the viscosity $\eta(\dot{\gamma})$ as follows:

$$\boldsymbol{J} = \frac{\partial \boldsymbol{R}}{\partial \boldsymbol{U}} = \tilde{\boldsymbol{K}}(\boldsymbol{U}) + \frac{\partial \tilde{\boldsymbol{K}}(\boldsymbol{U})}{\partial \boldsymbol{U}}\boldsymbol{U}, \qquad (2\text{-}12)$$

where, $\tilde{\boldsymbol{K}}(\boldsymbol{U}) = \boldsymbol{C}(\boldsymbol{U}) + \eta(\dot{\gamma})\boldsymbol{K}_\eta + \boldsymbol{K}_\alpha$ and using the chain rule, we have:

$$\frac{\partial \tilde{\boldsymbol{K}}(\boldsymbol{U})}{\partial \boldsymbol{U}} = \frac{\partial \boldsymbol{C}(\boldsymbol{U})}{\partial \boldsymbol{U}} + \frac{\partial \eta(\dot{\gamma})}{\partial \dot{\gamma}}\frac{\partial \dot{\gamma}}{\partial \boldsymbol{U}}\boldsymbol{K}_\eta, \qquad (2\text{-}13)$$

therefore, the final expression of the Jacobian matrix, $\boldsymbol{J}$, is

$$\boldsymbol{J} = \tilde{\boldsymbol{K}}\left(\boldsymbol{U}\right) + \left(\frac{\partial \boldsymbol{C}(\boldsymbol{U})}{\partial \boldsymbol{U}} + \frac{\partial \eta(\dot{\gamma})}{\partial \dot{\gamma}}\frac{\partial \dot{\gamma}}{\partial \boldsymbol{U}}\boldsymbol{K}_\eta\right)\boldsymbol{U}.$$

where the terms $\frac{\partial \eta(\dot{\gamma})}{\partial \dot{\gamma}}$ and $\frac{\partial \dot{\gamma}}{\partial \boldsymbol{U}}$ can be calculated as follows:

From Eq. (2-10), we derived the viscosity $\eta(\dot{\gamma})$ with respect the shear rate $\dot{\gamma}$ and we obtain:

$$\frac{\partial \eta(\dot{\gamma})}{\partial \dot{\gamma}} = (n-1)\lambda(\eta_0 - \eta_\infty)\left[1 + (\lambda\dot{\gamma})^a\right]^{\frac{n-1}{a}}(\lambda\dot{\gamma})^{a-1}. \quad (2\text{-}14)$$

From Eq. (2-11), we have:

$$\begin{aligned}
\frac{\partial \dot{\gamma}}{\partial \boldsymbol{u}_1} &= \dot{\gamma}^{-1}\left[2\frac{\partial u}{\partial x}\frac{\partial \phi}{\partial x} + \left(\frac{\partial u}{\partial y} + \frac{\partial v}{\partial x}\right)\frac{\partial \phi}{\partial y}\right] \\
\frac{\partial \dot{\gamma}}{\partial \boldsymbol{u}_2} &= \dot{\gamma}^{-1}\left[2\frac{\partial v}{\partial y}\frac{\partial \phi}{\partial y} + \left(\frac{\partial u}{\partial y} + \frac{\partial v}{\partial x}\right)\frac{\partial \phi}{\partial x}\right]
\end{aligned}. \quad (2\text{-}15)$$

Finally, Eq. (2-15) can be expressed in matrix form as $\frac{\partial \dot{\gamma}}{\partial \boldsymbol{U}} = \boldsymbol{M}_g\boldsymbol{U}$, where:

$$\boldsymbol{M}_g = \begin{bmatrix} 2\frac{\partial \phi}{\partial x}\frac{\partial \phi}{\partial x}^T + \frac{\partial \phi}{\partial y}\frac{\partial \phi}{\partial y}^T & \frac{\partial \phi}{\partial y}\frac{\partial \phi}{\partial x}^T \\ \frac{\partial \phi}{\partial x}\frac{\partial \phi}{\partial y}^T & 2\frac{\partial \phi}{\partial y}\frac{\partial \phi}{\partial y}^T + \frac{\partial \phi}{\partial x}\frac{\partial \phi}{\partial x}^T \end{bmatrix}.$$

3
Virtual element method

In this Chapter, we present the theoretical background on the VEM in more detail, and we discuss concepts related to polynomial space and projection operators. Further, we present the main steps of the computation of the main elementary matrices and vectors of the Navier-Stokes-Brinkman and non-Newtonian Carreau-Yasuda equations, focusing on the VEM and considering lower-order elements.

3.1
2D virtual element space

The Domain $\Omega \subset \mathbb{R}^2$ is partitioned in polygonal elements E (either convex or non-convex), and we define discretized domain Ω_h. Therefore, the global VEM space V_h is defined as:

$$V_h = \left\{ v_h \in H^1(\Omega_h) : v_h|_E \in V_k(E), \forall E \subset \Omega_h \right\}.$$

For each polygonal, E, we define a local finite element VEM space $V_k(E)$, using the lower-order element ($k = 1$) as:

$$V_k(E) = V_1(E) = \left\{ v \in H^1(E) : \nabla v = 0, v \in C^0(\partial E), v|_e \in P_1(e) \right\},$$
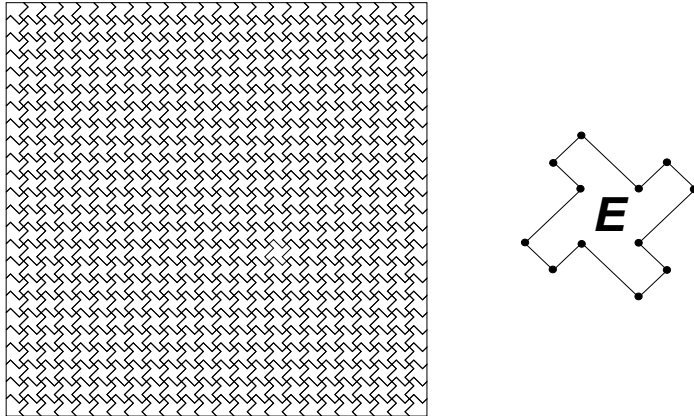
Figure 3.1: Example of partitioned domain Ω_h in non-convex elements E using tess12 elements (a non-convex polygonal element with 12 vertices). (Taken from [8]).

where, we highlight the following:

(i) v_h is a polynomial of lower-order on each edge e of E, *i.e.*, $v_h|_e \in P_1(e)$ (Polynomial space on each edge e of E);

(ii) v_h on ∂E is globally continuous *i.e.*, $v_h|_{\partial E} \in C^0(\partial E)$;

(iii) a polynomial of lower-order satisfies (i), (ii) so $P_1(E)$ is a subspace of $V_1(E)$, more details in the reference by (Beirão da Veiga *et al.*, 2014), [9].

Defining VEM basis functions by the lower-order element
($k = 1$)

By linear polynomial space, $P_k(E)$, the set of basis functions, $m_\alpha^{(k)}, \alpha = 1, \ldots, n_{p_k}$, are defined as

$$m_1^{(1)} = 1, \ m_2^{(1)} = \frac{x - x_C}{h_E}, \ m_3^{(1)} = \frac{y - y_C}{h_E}, \tag{3-1}$$

where n_{p_k} is the dimension of $P_k(E)$ and $n_{p_k} = 3$ is the dimension of $P_k(E)$ The respective gradients of $P_k(E)$ are

$$\nabla m_1^{(1)} = \begin{bmatrix} 0 \\ 0 \end{bmatrix}, \ \nabla m_2^{(1)} = \frac{1}{h_E} \begin{bmatrix} 1 \\ 0 \end{bmatrix}, \ \nabla m_3^{(1)} = \frac{1}{h_E} \begin{bmatrix} 0 \\ 1 \end{bmatrix}. \tag{3-2}$$

In vectorial polynomial space $[P_{k-1}(E)]^2$, the set of basis functions is made from the canonical two-dimensional basis vector $\boldsymbol{m}_\alpha^{(k-1)}, \alpha = 1, \ldots, n_{\boldsymbol{p}_{k-1}}$ defined as:

$$\boldsymbol{m}_1^{(0)} = \begin{bmatrix} 1 \\ 0 \end{bmatrix} \text{ and } \boldsymbol{m}_2^{(0)} = \begin{bmatrix} 0 \\ 1 \end{bmatrix}, \tag{3-3}$$

where $n_{\boldsymbol{p}_{k-1}}$ is the dimension of $[P_{k-1}(E)]^2$ and $n_{\boldsymbol{p}_{k-1}} = 2$.
x_c and y_c are the coordinates of the centroid of the element E, $|E|$ is the element area, and $h_E = |E|^{1/2}$ is the average element size.
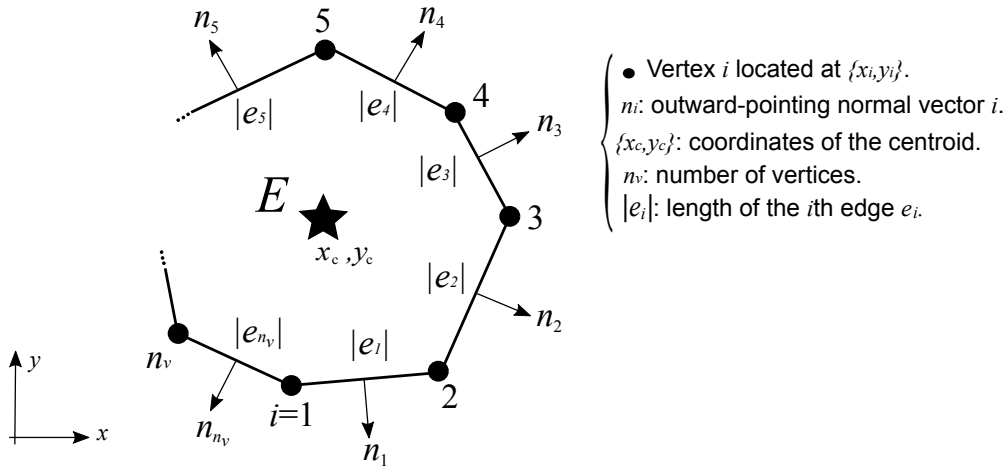
Figure 3.2: Details of the element VEM spaces and the degrees of freedom of a given element E, [14].

3.2
Virtual element projection $\Pi_E^0 \nabla v$

The first projection operator $\Pi_E^0 \nabla v$, which projects the gradient of v (∇v) in vectorial polynomial space $[P_{k-1}(E)]^2$, satisfies the orthogonality condition ([59],[60]) with:

$$< \nabla v - \Pi_E^0 \nabla v, \boldsymbol{p} >= 0, \ \forall \boldsymbol{p} \in [P_{k-1}(E)]^2,$$

The inner product $(<,>)$, satisfies the following expression:

$$\int_E \Pi_E^0 \nabla v \boldsymbol{p} d\boldsymbol{x} = \int_E \nabla v \boldsymbol{p} d\boldsymbol{x}, \ \forall \boldsymbol{p} \in [P_{k-1}(E)]^2.$$

By applying the divergence theorem we have:

$$\int_E \Pi_E^0 \nabla v \boldsymbol{p} d\boldsymbol{x} = \int_E \nabla v \boldsymbol{p} d\boldsymbol{x} = \oint_{\partial E} v \boldsymbol{p} \boldsymbol{n} ds - \int_E v \nabla . \boldsymbol{p} d\boldsymbol{x},$$
$$\forall \boldsymbol{p} \in [P_{k-1}(E)]^2. \tag{3-4}$$

By introducing a set of shape functions, $\phi_i(\boldsymbol{x}), i = 1, \ldots, n_v$, for the local VEM space, $V_h(E)$, we can express $\Pi_E^0 \nabla v$ as

$$\Pi_E^0 \nabla v = \sum_{i=1}^{n_v} \Pi_E^0 \nabla \phi_i(\boldsymbol{x}) V_i, \tag{3-5}$$

where V_i is the ith DOF of the functions in $V_h(E)$. Therefore, using the basis Eq. (3-3) and shape Eq. (3-5) functions, Eq. (3-4) can be rewritten as:

$$\int_E \Pi_E^0 \nabla \phi_i \boldsymbol{m}_\alpha^{(k-1)} d\boldsymbol{x} = \int_E \nabla \phi_i \boldsymbol{m}_\alpha^{(k-1)} d\boldsymbol{x} = \oint_{\partial E} \phi_i \boldsymbol{m}_\alpha^{(k-1)} \boldsymbol{n} ds -$$
$$\int_E \phi_i \nabla . \boldsymbol{m}_\alpha^{(k-1)} d\boldsymbol{x}, \ \alpha = 1, \ldots, n_{\boldsymbol{p}_{k-1}}. \tag{3-6}$$

We can also express $\Pi_E^0 \nabla \phi_i$ using the set of basis $\boldsymbol{m}_\alpha^{(k-1)}$ for $[P_{k-1}(E)]^2$ as:

$$\Pi_E^0 \nabla \phi_i(\boldsymbol{x}) = \sum_{\beta=1}^{n_{\boldsymbol{p}_{k-1}}} S_{i\beta} \boldsymbol{m}_\beta^{(k-1)}(\boldsymbol{x}). \tag{3-7}$$

Finally, Eq. (3-6) can be rewritten as:

$$\sum_{\beta=1}^{n_{\boldsymbol{p}_{k-1}}} S_{i\beta} \underbrace{\int_E \boldsymbol{m}_\beta^{(k-1)} \boldsymbol{m}_\alpha^{(k-1)} d\boldsymbol{x}}_{\boldsymbol{M}} = \underbrace{\oint_{\partial E} \phi_i \boldsymbol{m}_\alpha^{(k-1)} \boldsymbol{n} ds - \int_E \phi_i \nabla . \boldsymbol{m}_\alpha^{(k-1)} d\boldsymbol{x}}_{\boldsymbol{R}},$$
$$i = 1, \ldots, n_v \text{ and } \alpha = 1, \ldots, n_{\boldsymbol{p}_{k-1}}. \tag{3-8}$$

From Eq. (3-8), we can build the matrices $\boldsymbol{M}$ and $\boldsymbol{R}$ to compute the matrix $\boldsymbol{S}$ as:

$$\boldsymbol{S} = \boldsymbol{R}\boldsymbol{M}^{-1}. \tag{3-9}$$

3.3
Virtual element projection $\Pi_E^\nabla v$

The second projection operator, $\Pi_E^\nabla v$, which projects v onto lineal polynomial space, $P_k(E)$, satisfies the orthogonality condition as:

$$< \nabla(v - \Pi_E^\nabla v), \nabla p >= 0, \ \forall p \in P_k(E),$$

The inner product $(<, >)$, satisfies the following expression:

$$\int_E \nabla \Pi_E^\nabla v \nabla p d\boldsymbol{x} = \int_E \nabla v \nabla p d\boldsymbol{x}, \ \forall p \in P_k(E).$$

Applying the divergence theorem, we have

$$\int_E \nabla \Pi_E^\nabla v \nabla p d\boldsymbol{x} = \int_E \nabla v \nabla p d\boldsymbol{x} = \oint_{\partial E} v \nabla p \boldsymbol{n} ds - \int_E v \Delta p d\boldsymbol{x}, \tag{3-10}$$
$$\forall p \in P_k(E).$$

We can express $\Pi_E^\nabla v$ using the shape functions, ϕ_i, as:

$$\Pi_E^\nabla v = \sum_{i=1}^{n_v} \Pi_E^\nabla \phi_i(\boldsymbol{x}) V_i. \tag{3-11}$$

Therefore, using Equations Eq. (3-1), Eq. (3-2), and Eq. (3-10), Eq. (3-11) can be rewritten as:

$$\int_E \nabla \Pi_E^\nabla \phi_i \nabla m_\alpha^{(k)} d\boldsymbol{x} = \int_E \nabla \phi_i \nabla m_\alpha^{(k)} d\boldsymbol{x} = \oint_{\partial E} \phi_i \nabla m_\alpha^{(k)} \boldsymbol{n} ds -$$
$$\int_E \phi_i \Delta m_\alpha^{(k)} d\boldsymbol{x}, \ \alpha = 1, \ldots, n_{p_k}. \tag{3-12}$$

We can also express $\Pi_E^\nabla \phi_i$ in terms of the basis set, $m_\alpha^{(k)}$ for $P_k(E)$ as:

$$\Pi_E^\nabla \phi_i = \sum_{\alpha=1}^{n_{p_k}} S_{i\alpha}^\nabla m_\alpha^{(k)}. \tag{3-13}$$

By combining the basis in Eq. (3-3) and shape functions of Eq. (3-13), we obtain:

$$\sum_{\beta=2}^{n_{p_k}} S_{i\beta}^\nabla \underbrace{\int_E \nabla m_\beta^{(k)} \nabla m_\alpha^{(k)} d\boldsymbol{x}}_{\boldsymbol{M}^\nabla} = \underbrace{\oint_{\partial E} \phi_i \nabla m_\alpha^{(k)} \boldsymbol{n} ds - \int_E \phi_i \Delta m_\alpha^{(k)} d\boldsymbol{x}}_{\boldsymbol{R}^\nabla}, \tag{3-14}$$
$$i = 1, \ldots, n_v \text{ and } \alpha = 1, \ldots, n_{p_k}.$$

From Eq. (3-14), we can build matrices $\boldsymbol{M}^\nabla$ and $\boldsymbol{R}^\nabla$ and compute the matrix $\boldsymbol{S}^\nabla$ as

$$\boldsymbol{S}^\nabla = \boldsymbol{R}^\nabla (\boldsymbol{M}^\nabla)^{-1}. \tag{3-15}$$

Main remarks: considering lower-order element ($k = 1$), the second term of the second member of Eqs. (3-8) and Eq. (3-14) can be neglected, *i.e.*, $\nabla.\boldsymbol{m}_\alpha^{(0)} = 0$ and $\Delta m_\alpha^{(1)} = 0$, resulting in very short computational time to obtain a solution of the linear system of equations.

Additionally, from Eq. (3-13)), we can express $\Pi_E^\nabla \phi_i(\boldsymbol{x})$ in terms of the shape funtions $\phi_i, i = 1, ..., n_v$ as:

$$\Pi_E^\nabla \phi_i(\boldsymbol{x}) = \sum_{i=1}^{n_v} P_{ij}^\nabla \phi_j(\boldsymbol{x}). \tag{3-16}$$

Using the set of basis functions $m_\alpha^{(k)}$, for $P_k(E)$ as:

$$m_\alpha^{(k)}(\boldsymbol{x}) = \sum_{j=1}^{n_v} G_{\alpha j}^\nabla \phi_j(\boldsymbol{x}), \tag{3-17}$$

and substituting Eq. (3-17) into Eq. (3-13), we obtain:

$$\Pi_E^\nabla \phi_i = \sum_{\alpha=1}^{n_{pk}} S_{i\alpha}^\nabla \sum_{j=1}^{n_v} G_{\alpha j}^\nabla \phi_j(\boldsymbol{x}) = \sum_{\alpha=1}^{n_{pk}} \sum_{j=1}^{n_v} \underbrace{S_{i\alpha}^\nabla G_{\alpha j}^\nabla}_{P_{ij}^\nabla} \phi_j(\boldsymbol{x}). \tag{3-18}$$

Comparing with Eq. (3-16), we obtain the $\boldsymbol{P}^\nabla$ matrix as:

$$\boldsymbol{P}^\nabla = \boldsymbol{S}^\nabla \boldsymbol{G}^\nabla, \tag{3-19}$$

where S^∇ is obtained by Eq. (3-15) and:

$$\boldsymbol{G}^\nabla = \begin{bmatrix} 1 & \dots & 1 \\ m_2^{(1)}(\boldsymbol{x}_1) & \dots & m_2^{(1)}(\boldsymbol{x}_{n_v}) \\ m_3^{(1)}(\boldsymbol{x}_1) & \dots & m_3^{(1)}(\boldsymbol{x}_{n_v}) \end{bmatrix},$$

where $m_\alpha^{(1)}(\boldsymbol{x}_i)$, $i = 1, \dots, n_v$, $\alpha = 1, \dots, n_{p_k}$ indicates the αth basis function for $P_k(E)$ evaluated at position $\boldsymbol{x}_i$ of the ith vertex.

VEM computation of main elementary matrices and vectors of the Navier-Stokes-Brinkman and Carreau-Yasuda equations

Now, from Eq. (2-5), the main element matrices ($\boldsymbol{K}_\eta, \boldsymbol{K}_\alpha, \boldsymbol{C}$) and vectors ($\boldsymbol{Q}, \boldsymbol{F}$) can be computed using virtual element projections $\Pi_E^0 \nabla \phi_i$ and $\Pi_E^\nabla \phi_i$ as follows.

Computing $\{\boldsymbol{K}_\eta\}_h$:

The global $\{\boldsymbol{K}_\eta\}_h$ matrix is defined as

$$\{\boldsymbol{K}_\eta\}_h(\boldsymbol{u}_h, \boldsymbol{v}_h) := \sum_{E \in \Omega_h} \{\boldsymbol{K}_\eta\}_h^E(\boldsymbol{u}_h, \boldsymbol{v}_h),$$

and, the discrete element matrix $\{\boldsymbol{K}_\eta\}_h^E$ is expressed as

$$\{\boldsymbol{K}_\eta\}_h^E(\boldsymbol{u}_h, \boldsymbol{v}_h) := (\Pi_E^0 \nabla \boldsymbol{u}_h, \Pi_E^0 \nabla \boldsymbol{v}_h)_{0,E} + S^E(\boldsymbol{u}_h - \Pi_E^\nabla \boldsymbol{u}_h, \boldsymbol{v}_h - \Pi_E^\nabla \boldsymbol{v}_h)$$

$$\text{(3-20)}$$

where, $\{\boldsymbol{K}_\eta\}_h^E : \boldsymbol{V}_h^E \times \boldsymbol{V}_h^E \to \mathbb{R}.$

Therefore,

$$\{\boldsymbol{K}_\eta\}_h^E(\phi_i, \phi_j) = \int_E \Pi_E^0 \nabla \phi_i \Pi_E^0 \nabla \phi_j d\boldsymbol{x} + \alpha \boldsymbol{S}^*(\phi_i - \Pi_E^\nabla \phi_i, \phi_j - \Pi_E^\nabla \phi_j). \quad \text{(3-21)}$$

With substitution of Eq. (3-7) into the first term of Eq. (3-21), the consistency term can be expressed as:

$$\int_E \Pi_E^0 \nabla \phi_i \Pi_E^0 \nabla \phi_j d\boldsymbol{x} = \boldsymbol{C}_\eta \sum_{\alpha=1}^{n_{p_{k-1}}} \sum_{\beta=1}^{n_{p_{k-1}}} S_{i\alpha} S_{j\beta} \int_E \boldsymbol{m}_\beta^{(k-1)} \boldsymbol{m}_\alpha^{(k-1)} d\boldsymbol{x} = \boldsymbol{SMC}_\eta \boldsymbol{S}^T,$$

$$\text{(3-22)}$$

where:

$$\boldsymbol{C}_\eta = \eta(\dot{\gamma}) \begin{bmatrix} 2 & 0 & 0 \\ 0 & 2 & 0 \\ 0 & 0 & 1 \end{bmatrix}.$$

Substituting Eqs. (3-13) and (3-19) in the second term of Eq. (3-21), the stability term is given by

$$\boldsymbol{S}^*(\phi_i - \Pi_E^\nabla \phi_i, \phi_j - \Pi_E^\nabla \phi_j) = \alpha_E(\delta_{ik} - P_{ik}^\nabla)(\delta_{jk} - P_{jk}^\nabla)$$
$$= \alpha(\boldsymbol{I} - \boldsymbol{P}^\nabla)(\boldsymbol{I} - \boldsymbol{P}^\nabla)^T,$$

$$\text{(3-23)}$$

where α is the stability factor and takes the value of 1 for Navier-Stokes problems (more comments will be presented at the end of this chapter.)

We highlight that, from Eq. (3-22), the local viscosity must be computed first. When this value is constant and different in each element, the formulation of the viscosity is described by Eqs. (2-10) and (2-11) through Eq. (2-9) and it only depends on the local velocity gradients. Then, from Eq. (3-7), we can express these velocity gradients as a function of the virtual element projection as follows:

$$\begin{cases} \dfrac{\partial \boldsymbol{u}_1}{\partial x} = (\Pi_E^0 \nabla \phi_i)_x^T \boldsymbol{u}_1 = \begin{bmatrix} S_{11} \\ S_{21} \\ \vdots \\ S_{n_v 1} \end{bmatrix} \begin{bmatrix} u_1^1, ..., u_1^{n_v} \end{bmatrix} \\[40pt] \dfrac{\partial \boldsymbol{u}_1}{\partial y} = (\Pi_E^0 \nabla \phi_i)_y^T \boldsymbol{u}_1 = \begin{bmatrix} S_{12} \\ S_{22} \\ \vdots \\ S_{n_v 2} \end{bmatrix} \begin{bmatrix} u_1^1, ..., u_1^{n_v} \end{bmatrix} \end{cases}$$

$$\text{(3-24)}$$

and

$$\begin{cases} \dfrac{\partial \boldsymbol{u}_2}{\partial x} = (\Pi_E^0 \nabla \phi_i)_x^T \boldsymbol{u}_2 = \begin{bmatrix} S_{11} \\ S_{21} \\ \vdots \\ S_{n_v 1} \end{bmatrix} \begin{bmatrix} u_2^1, ..., u_2^{n_v} \end{bmatrix} \\[3em] \dfrac{\partial \boldsymbol{u}_2}{\partial y} = (\Pi_E^0 \nabla \phi_i)_y^T \boldsymbol{u}_2 = \begin{bmatrix} S_{12} \\ S_{22} \\ \vdots \\ S_{n_v 2} \end{bmatrix} \begin{bmatrix} u_2^1, ..., u_2^{n_v} \end{bmatrix} \end{cases} . \tag{3-25}$$

Computing $\{\boldsymbol{K}_\alpha\}_h$:

The global $\{\boldsymbol{K}_\alpha\}_h$ matrix is defined as:

$$\{\boldsymbol{K}_\alpha\}_h(\boldsymbol{u}_h, \boldsymbol{v}_h) := \sum_{E \in \Omega_h} \{\boldsymbol{K}_\alpha\}_h^E(\boldsymbol{u}_h, \boldsymbol{v}_h),$$

and, the discrete element matrix $\{\boldsymbol{K}_\alpha\}_h^E$ is expressed as:

$$\{\boldsymbol{K}_\alpha\}_h^E(\boldsymbol{u}_h, \boldsymbol{v}_h) := (\Pi_E^\nabla \boldsymbol{u}_h, \Pi_E^\nabla \boldsymbol{v}_h)_{0,E}, \tag{3-26}$$

where, $\{\boldsymbol{K}_\alpha\}_h^E : \boldsymbol{V}_h^E \times \boldsymbol{V}_h^E \to \mathbb{R}$. Therefore:

$$\{\boldsymbol{K}_\alpha\}_h^E(\phi_i, \phi_j) = \int_E \overline{\alpha} \Pi_E^\nabla \phi_i . \Pi_E^\nabla \phi_j d\boldsymbol{x}. \tag{3-27}$$

Substituting Eq. (3-13) into Eq. (3-27), we obtain:

$$\int_E \overline{\alpha} \Pi_E^\nabla \phi_i \Pi_E^\nabla \phi_j d\boldsymbol{x} = \overline{\alpha} \sum_{\alpha=1}^{n_{p_k}} \sum_{\beta=1}^{n_{p_k}} S_{i\alpha}^\nabla S_{j\beta}^\nabla \int_E m_\beta^{(k)} . m_\alpha^{(k)} d\boldsymbol{x} = \overline{\alpha} |E| \boldsymbol{N} \boldsymbol{N}^T, \tag{3-28}$$

where

$$\boldsymbol{N} = \begin{bmatrix} S_{11}^\nabla & S_{12}^\nabla & S_{13}^\nabla \\ S_{21}^\nabla & S_{22}^\nabla & S_{23}^\nabla \\ \vdots & \vdots & \vdots \\ S_{n_v 1}^\nabla & S_{n_v 2}^\nabla & S_{n_v 3}^\nabla \end{bmatrix} \begin{bmatrix} m_1^{(1)}(\boldsymbol{x}_c) \\ m_2^{(1)}(\boldsymbol{x}_c) \\ m_3^{(1)}(\boldsymbol{x}_c) \end{bmatrix} \text{ and } \boldsymbol{x}_C = [x_c, y_c]. \tag{3-29}$$

Computing $\{\boldsymbol{Q}_h\}_h$:

The global $\{\boldsymbol{Q}\}_h$ vector is defined as:

$$\{\boldsymbol{Q}\}_h(\boldsymbol{u}_h, \boldsymbol{q}_h) := \sum_{E \in \Omega_h} \{\boldsymbol{Q}\}_h^E(\boldsymbol{u}_h, \boldsymbol{q}_h),$$

and the discrete element vector $\{\boldsymbol{Q}\}_h^E$ is expressed as:

$$\{\boldsymbol{Q}\}_h^E(\boldsymbol{u}_h) := (\nabla . \Pi_E^\nabla \boldsymbol{v}_h)_{0,E}, \tag{3-30}$$

where, $\{\boldsymbol{Q}\}_h^E : \boldsymbol{V}_h^E \times \boldsymbol{q}_h^E \to \mathbb{R}$. Therefore, substituting Eq. (3-13) into Eq. (3-31), we obtain:

$$\{\boldsymbol{Q}\}_h^E(\phi_i) = \int_E \nabla.\Pi_E^\nabla \phi_i dx = \sum_{\alpha=1}^{n_{p_k}} S_{i\alpha}^\nabla \nabla.m_\alpha^{(k)} \tag{3-31}$$

or

$$\{\boldsymbol{Q}\}_h^E = \begin{bmatrix} S_{11}^\nabla & S_{12}^\nabla & S_{13}^\nabla \\ S_{21}^\nabla & S_{22}^\nabla & S_{23}^\nabla \\ \vdots & \vdots & \vdots \\ S_{n_v1}^\nabla & S_{n_v2}^\nabla & S_{n_v3}^\nabla \end{bmatrix} \begin{bmatrix} \nabla.m_1^{(1)} \\ \nabla.m_2^{(1)} \\ \nabla.m_3^{(1)} \end{bmatrix} = \frac{1}{h_E} \begin{bmatrix} S_{12}^\nabla \\ S_{13}^\nabla \\ \vdots \\ S_{n_v2}^\nabla \\ S_{n_v3}^\nabla \end{bmatrix}, \ i = 1, ..., n_v. \tag{3-32}$$

Computing $\{\boldsymbol{C}\}_h$:

The global $\{\boldsymbol{C}\}_h$ matrix is defined as:

$$\{\boldsymbol{C}\}_h(\boldsymbol{w}_h; \boldsymbol{u}_h, \boldsymbol{v}_h) := \sum_{E \in \Omega_h} \{\boldsymbol{C}\}_h^E(\boldsymbol{w}_h; \boldsymbol{u}_h, \boldsymbol{v}_h),$$

and, the discrete element matrix $\{\boldsymbol{C}\}_h^E$ is expressed as:

$$\{\boldsymbol{C}\}_h^E(\boldsymbol{u}_l) := (\rho\Pi_E^\nabla \phi_i; \Pi_E^\nabla \phi_j \boldsymbol{u}_l, \Pi_E^0 \nabla \phi_i)_{0,E} \tag{3-33}$$

where, $\{\boldsymbol{C}\}_h^E : \boldsymbol{V}_h^E \times \boldsymbol{V}_h^E \times \boldsymbol{V}_h^E \to \mathbb{R}$. Therefore:

$$\boldsymbol{C}_h^E(\boldsymbol{u}_l) = \rho \int_E \Pi_E^\nabla \phi_i \left(\Pi_E^\nabla \phi_j \boldsymbol{u}_l\right) \Pi_E^0 \nabla \phi_i d\boldsymbol{x}, \ l = 1, 2. \tag{3-34}$$

Substituting Eqs. (3-7) and (3-13) into Eq. (3-34), we obtain:

$$\boldsymbol{C}_h^E(\boldsymbol{u}_l) = \rho|E| \sum_{\alpha=1}^{n_{p_k}} S_{i\alpha}^\nabla m_\alpha^{(k)} \left(\sum_{\beta=1}^{n_{p_k}} S_{i\beta}^\nabla m_\beta^{(k)} \boldsymbol{u}_l\right) \sum_{w=1}^{n_{p_{k-1}}} S_{iw} m_w^{(k-1)} d\boldsymbol{x}, \tag{3-35}$$

From Eq. (3-29), we can express Eq. (3-35) in the simple vector form as $\boldsymbol{C}_h^E(\boldsymbol{u}_l) = \rho|E|\boldsymbol{N} \left(\boldsymbol{N}^T \boldsymbol{u}_l\right) \tilde{\boldsymbol{S}}$, where we define vector $\tilde{\boldsymbol{S}}$ as:

$$\tilde{\boldsymbol{S}} = \begin{bmatrix} S_{11} & S_{12} \\ S_{21} & S_{22} \\ \vdots & \vdots \\ S_{n_v1} & S_{n_v2} \end{bmatrix} \begin{bmatrix} \boldsymbol{m}_1^{(0)} \\ \boldsymbol{m}_2^{(0)} \end{bmatrix} = \begin{bmatrix} S_{11} \\ S_{12} \\ \vdots \\ S_{n_v1} \\ S_{n_v2} \end{bmatrix}.$$

Finally, we observe that for $l = 1, 2$ we have $\boldsymbol{C}_h^E(\boldsymbol{u}_l) = \boldsymbol{C}_{1h}^E(\boldsymbol{u}_1) + \boldsymbol{C}_{2h}^E(\boldsymbol{u}_2)$, then:

$$\boldsymbol{C}_{1h}^E(\boldsymbol{u}_1) = \rho|E|\boldsymbol{N}\left(\boldsymbol{N}^T\boldsymbol{u}_1\right) \begin{bmatrix} S_{11} \\ S_{21} \\ \vdots \\ S_{n_v1} \end{bmatrix} \text{ and } \boldsymbol{C}_{2h}^E(\boldsymbol{u}_2) = \rho|E|\boldsymbol{N}(\boldsymbol{N}^T\boldsymbol{u}_2) \begin{bmatrix} S_{12} \\ S_{22} \\ \vdots \\ S_{n_v2} \end{bmatrix}.$$

(3-36)

Computing $\{\boldsymbol{F}\}_h$:

The global $\{\boldsymbol{F}\}_h$ vector is defined as:

$$\{\boldsymbol{F}\}_h(\boldsymbol{v}_h) := \sum_{E\in\Omega_h} \{\boldsymbol{F}\}_h^E(\boldsymbol{v}_h),$$

and, the discrete element vector $\{\boldsymbol{F}\}_h^E$ is expressed as:

$$\{\boldsymbol{F}\}_h^E(\boldsymbol{v}_h) := (f\Pi_E^\nabla \boldsymbol{v}_h)_{0,E}, \tag{3-37}$$

where, $\{\boldsymbol{F}\}_h^E : \boldsymbol{V}_h^E \to \mathbb{R}$. Therefore, substituting Eq. (3-13) into Eq. (3-37), we have

$$\{\boldsymbol{F}\}_h^E(\phi_j) = \int_E f\Pi_E^\nabla \phi_j d\boldsymbol{x} = \sum_{\alpha=1}^{n_{p_k}} f S_{j\alpha}^\nabla m_\alpha^{(k)}(\boldsymbol{x}_c) = |E|f(\boldsymbol{x}_c)\boldsymbol{S}^\nabla m_\alpha^{(1)}(\boldsymbol{x}_c). \tag{3-38}$$

where the value of the basis $m_\alpha^{(1)}$ at the centroid element $\boldsymbol{x}_c$ is $m_\alpha^{(1)}(\boldsymbol{x}_c) = [1\ 0\ 0]^T$ and $f(\boldsymbol{x}_c)$ is the loading source term function. Besides, we use one point of integration at the centroid and the weight as the area of the element $|E|$.

In brief, from Eq. (2-5), the expressions of the main elementary matrices and vectors of the NVSB equation with focus on the VEM is:

$$\begin{cases} \{\boldsymbol{K}_\eta\}_h^E = \boldsymbol{SMC}_\eta\boldsymbol{S}^T + \alpha(\boldsymbol{I}-\boldsymbol{P}^\nabla)(\boldsymbol{I}-\boldsymbol{P}^\nabla)^T, \ \{\boldsymbol{K}_\alpha\}_h^E = \overline{\alpha}|E|\boldsymbol{NN}^T, \\[2mm] \boldsymbol{C}_h^E(\boldsymbol{u}_l) = \rho|E|\boldsymbol{N}\left(\boldsymbol{N}^T\boldsymbol{u}_1\right) \begin{bmatrix} S_{11} \\ S_{21} \\ \vdots \\ S_{n_v1} \end{bmatrix} + \rho|E|\boldsymbol{N}(\boldsymbol{N}^T\boldsymbol{u}_2) \begin{bmatrix} S_{12} \\ S_{22} \\ \vdots \\ S_{n_v2} \end{bmatrix}, l = 1,2. \\[2mm] \{\boldsymbol{Q}\}_h^E = \dfrac{1}{h_E} \begin{bmatrix} S_{12}^\nabla \\ S_{13}^\nabla \\ \vdots \\ S_{n_v2}^\nabla \\ S_{n_v3}^\nabla \end{bmatrix}, \ \{\boldsymbol{F}\}_h^E = |E|f(\boldsymbol{x}_c)\boldsymbol{S}^\nabla m_\alpha^{(1)}(\boldsymbol{x}_c). \end{cases}$$

(3-39)

The main references of this section are based on the works of Ahmad et al., (2013) [65], Beirão da Veiga et al., (2013)[66], Beirão da Veiga et al., (2014) [9], (2016) [67]; Gain *et al.* (2014) [46], Paulino and Gain (2015) [8], Brener *et*

al. (2017) [68].

3.4
VEM verification

Channel flow problem for non-Newtonian fluid: Consider the channel flow domain problem, studied by Siebert and Fodor (2009) [13]. Blood properties are density, $\rho = 1.056 \text{gr}/cm^3$, and the viscosity parameters for the Carreau-Yasuda model, are shown in Table (3.1).

Table 3.1: Carrea-Yasuda parameters for blood fluid.

parameter	value
a	2
n	0.3568
λ	3.313
η_0	0.56 poise
η_∞	0.035 poise

The geometry and boundary conditions are illustrated in Figure 3.3, for two maximum inlet velocities, 2.5 cm/s and 80 cm/s, and the outlet pressure is zero.
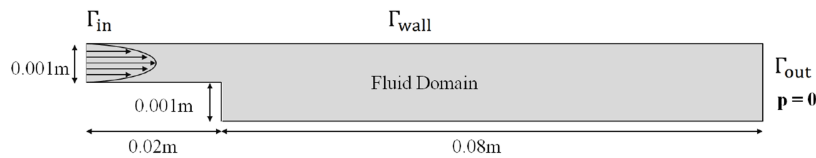
Figure 3.3: Channel flow problem.(Extracted from Kian, (2017) [12].)

The numerical results, using 4,000 polygonal elements, of the velocity field for the Newtonian and non-Newtonian (Carreau-Yasuda) model, are shown in Figure 3.4 and 3.5, respectively. Figure 3.6 shows a comparison of the velocity profiles at the outlet.
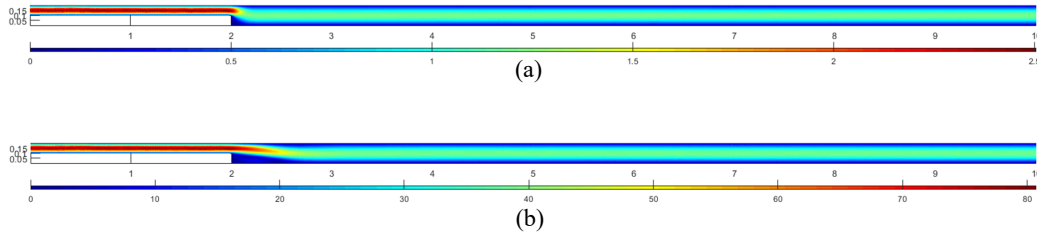
Figure 3.4: Velocity field for the Newtonian model for inlet center line velocities: (a) 2.5 cm/s, and (b) 80 cm/s.
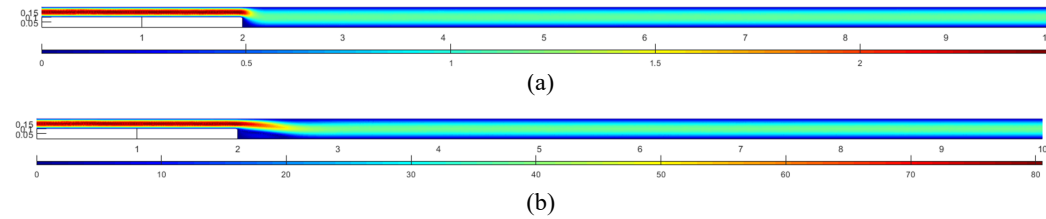
Figure 3.5: Velocity field for the non-Newtonian model (Carreau Yasuda) for inlet center line velocities: (a) 2.5 cm/s, and (b) 80 cm/s.
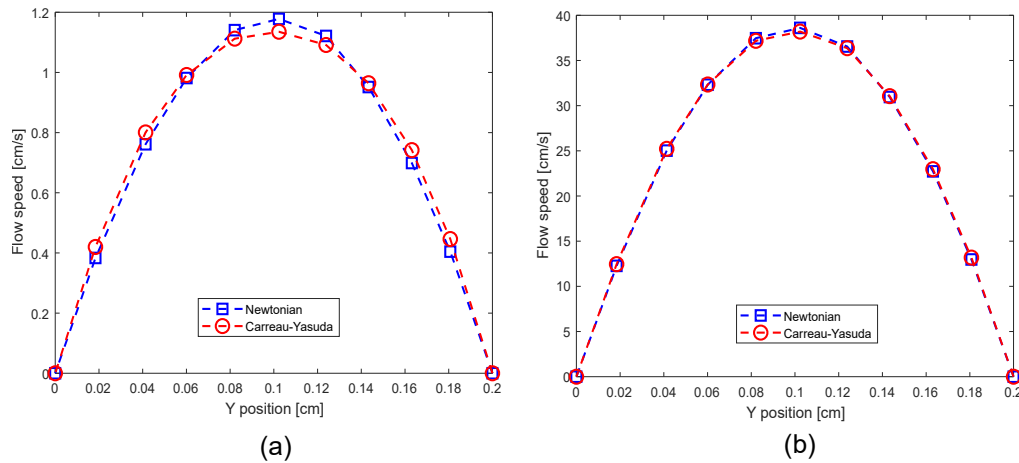
Figure 3.6: Comparison between the velocity profiles at the outlet for the Newtonian and non-Newtonian (Carreau-Yasuda) models by inlet speed of (a) 2.5 cm/s and (b) 80 cm/s.

From Siebert and Fodor [13], velocity fields for the Carreau model for inlet center line velocities of 0.025m/s and 0.8m/s are shown in Figure 3.7(a) and the comparison between the velocity profiles at the outlet for the Newtonian and Carreau-Yasuda models are shown in Figure 3.7(b). The results presented here were obtained using the COMSOL Multiphysics 3.5 package [13].
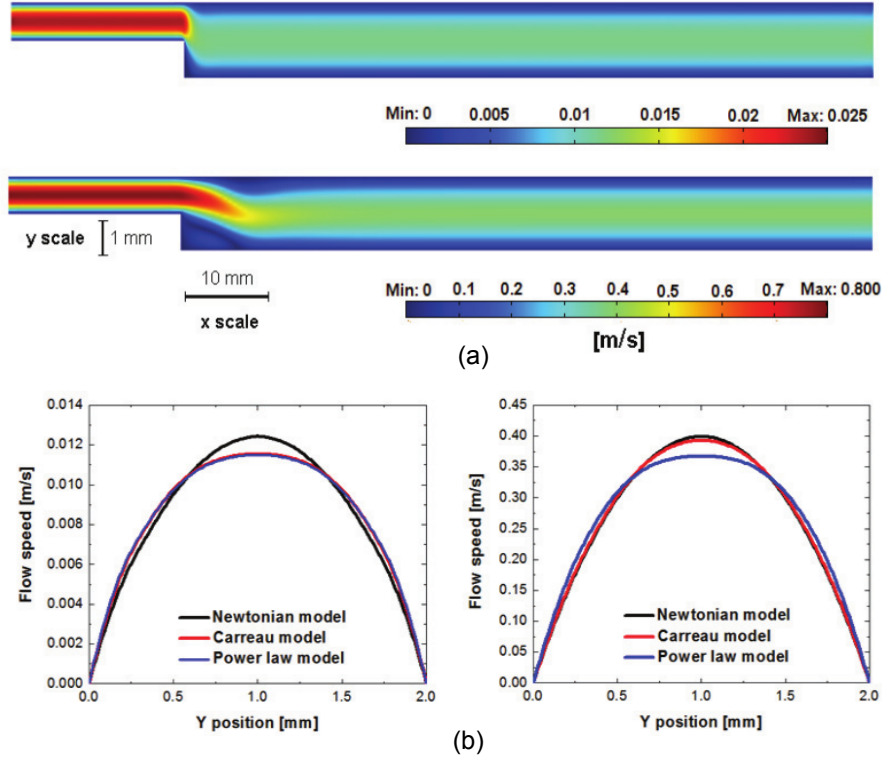
Figure 3.7: Results obtained using COMSOL software [13]. (a) Velocities field for the Carreua-Yasuda model and (b) Velocity profiles.

Relevant comments on the Virtual Element Method:

The general Navier-Stokes-Brinkman equation presents terms such as: transient, diffusive, convective, and source term, where for lower Reynold numbers (laminar flow), the diffusive term, which contains the Laplacian of velocity ($\Delta \boldsymbol{u}$) and viscosity $\eta(\dot{\gamma})$, as a function of velocity gradient, (see Eq.(2-1)), is the most dominant term in the differential equation:

$$E.D.: \quad \underbrace{\frac{\partial(\rho\boldsymbol{\phi})}{\partial t}}_{transient} + \underbrace{div(\rho\boldsymbol{u}\boldsymbol{\phi})}_{convective} = \underbrace{div(\Gamma grad\boldsymbol{\phi})}_{diffusive} + \underbrace{S}_{source}.$$

where $\boldsymbol{\phi} = \boldsymbol{u}$ and $\Gamma = \eta(\dot{\gamma})$.

From the VEM formulation of the diffusive term, Eq.(3-21), it contains two main terms: consistency and stability. For the consistency term, the non-Newtonian viscosity field using the Carreau-Yasuda model, is obtained using the information of the local velocity gradients. The viscosity results, (similar to the pressure field), is a low order term (constant) in each element and, therefore, it can come out of the integral, allowing us to calculate the diffusive term in the element in the same traditional way. It is important to mention that, in the FEM, the viscosity is computed in each integration point of the element. This process is computationally expensive compared to the

VEM method, where the viscosity is a constant value for each element.

From Section 3.4 and Chapter 4, the stability factor was defined by comparing the analytical and FEM numerical solutions of Newtonian and non-Newtonian fluid-flow tests, with errors in the order below 10^{-4}. The stability factor was set as unity.

From the discrete problem, the bilinear form of the local a^E is:

$$a^E(u,v) := (u,v)_{0,E}, \forall u, v \in H^1(E), \ a^E : H^1(E) \times H^1(E) \to \mathbb{R}$$

the discrete counterpart of a^E is:

$$a_h^E(\boldsymbol{u}_h, \boldsymbol{v}_h) := \underbrace{(\Pi_E^0 \nabla \boldsymbol{u}_h, \Pi_E^0 \nabla \boldsymbol{v}_h)_{0,E}}_{consistency} + \underbrace{\alpha S^E(\boldsymbol{u}_h - \Pi_E^\nabla \boldsymbol{u}_h, \boldsymbol{v}_h - \Pi_E^\nabla \boldsymbol{v}_h)}_{stability},$$

$$V_h^E \times V_h^E \to \mathbb{R},$$

where

$$a_h(\boldsymbol{u}_h, \boldsymbol{v}_h) := \sum_{E \in \Omega_h} a_h^E(\boldsymbol{u}_h, \boldsymbol{v}_h), \ \forall u_h, v_h \in V_h,$$

here, a_h is the discrete counterpart of the global a.

The local discrete bilinear form satisfy the following expressions:

(a) *Polynomial consistency*,

$$a_h^E(u_h, p) = a^E(u_h, p), \ \forall u_h \in V_h^E \text{ and } p \in \wp,$$

expressing the fact that the method is exact when the solution is a piecewise linear polynomial with respect to the mesh, providing the accuracy of the method.

(b) *Stability*, there exists two positive constants α_* and α^*, independent of h and E, such that [7],[9]:

$$\alpha_* a^E(v_h, v_h) \leq a_h^E(v_h, v_h) \leq \alpha^* a^E(v_h, v_h), \ \forall v_h \in V_h^E.$$

4
Convergence analysis of VEM-FEM

In this Chapter, we present and discuss the results of the convergence study on the Navier-Stokes-Brinkman solution, using the lower-order element, VEM and FEM methods, and Newtonian and non-Newtonian (using by the Carreau-Yasuda model) fluids. Numerical results presented were implemented in MATLAB®, and adapting and incorporating codes in the `PolyTop` (See Talischi *et al.*, 2012 [19] and Pereira *et al.*, 2016 [5]). In Chapter 4.1 we show results of convergence tests applied to a Newtonian fluid and in Chapter 4.2 we present results using a non-Newtonian fluid.

4.1
Work methodology

First, we defined a polygonal discretization of the domain using the mesh generator `Polymesher` (Talischi *et al.*, 2012) [15]. Then, numerical results for the fluid flow problem considering both Newtonian and non-Newtonian Carreau-Yasuda cases were obtained and the velocities and pressures were compared to the analytical solution, for successive mesh refinement. We used the expression for the numerical error presented in (Fish and Belytschko, 2007) [69], given by:

$$\|error\|_{L^2} = \|\boldsymbol{u}^{ex}(x) - \boldsymbol{u}^h(x)\| = \left(\int_{\Omega} \left(\boldsymbol{u}^{ex}(x) - \boldsymbol{u}^h(x) \right)^2 d\boldsymbol{x} \right)^{\frac{1}{2}}, \qquad (4\text{-}1)$$

where u^{ex} represents the exact solution and u^h represents the approximate solution using the VEM and FEM. From Eq. (4-1), this error can be considered as a measure of the mean square error. Finally, we compared the numerical solution of the VEM and FEM with respect to their computational performance.

The vector $\mathbf{u}^h$ denotes the displacement field obtained by interpolating the VEM and FEM dofs using the Wachspress shape functions (Talischi *et al.*, [70]) and, we used 7 Gauss points for each triangle that defines a polygonal element.

From Beirão da Veiga *et al.*, [57], in order to compute the errors, we consider the computable error quantities of the velocity gradients, velocity

and pressure as:

$$error(\boldsymbol{u}, H^1) := \left(\sum_{E \in \Omega_h} \| \nabla \boldsymbol{u}^{ex}(x) - \nabla \boldsymbol{u}^h(x) \|^2 \right)^{\frac{1}{2}}$$

$$error(\boldsymbol{u}, L^2) := \left(\sum_{E \in \Omega_h} \| \boldsymbol{u}^{ex}(x) - \boldsymbol{u}^h(x) \|^2 \right)^{\frac{1}{2}}. \tag{4-2}$$

$$error(p, L^2) := \| p^{ex}(x) - p^h(x) \|$$

For the numerical tests we used two different types of domains defined as Test 01: quad domain and Test 02: lid-driven cavity domain.

4.2
Convergence tests using Newtonian fluid

The numerical results were obtained using a machine with an Intel Core$i7 - 8700$ CPU @3.20 GHz, 16.0 GB RAM, Microsoft Windows 10 64-bit operating system, and running MATLAB® $R2018b$ version as follows.

Test 01: A square domain of unit dimensions 1x1 is used (Figure 4.1). We consider a unit value of the viscosity and density and we choose the components of the load vector $\boldsymbol{f} = [f_x, f_y]$ as $f_x = 2x^3 + y - 2$ and $f_y = 2yx^2 + x$, such that the analytical solutions for velocity and pressure are:

$$\boldsymbol{u}(x, y) = \begin{bmatrix} x^2 \\ -2xy \end{bmatrix}, \ p(x, y) = xy.$$
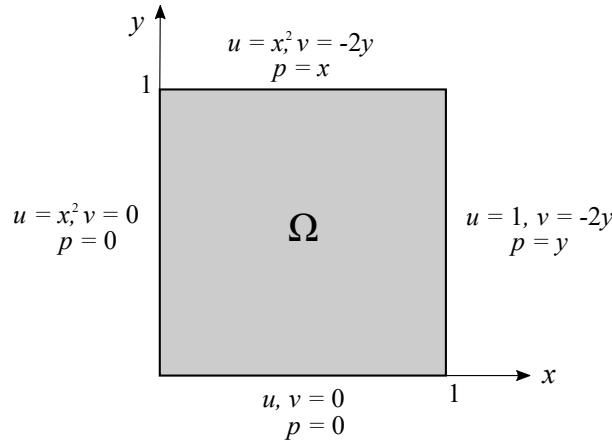
Figure 4.1: Geometry and boundary conditions of Test 01.

Test 02: A square domain of unit dimension 1x1 is also used (Figure 4.2) and the values of viscosity and density are set to 1. The boundary condition, in terms of velocity, is $\boldsymbol{u}(x, 1) = 16(x^4 - 2x^3 + x^2)$ and we choose the components of the load vector $\boldsymbol{f} = [0, f_y]$ as $f_y = -8[24S(x) + 2s'(x)g''(y) + s'''(x)g(y)] -$

$64[S_2(x)G_1(y) - g(y)g'(y)S_1(x)]$ such that the analytical solution for velocity and pressure are:

$$\boldsymbol{u}(x,y) = \begin{bmatrix} 8s(x)g'(y) \\ -8s'(x)g(y) \end{bmatrix},$$

$$p(x,y) = 8(S(x)g'''(y) + s'(x)g'(y)) + 64S_2(x)(g(y)g''(y) - [g'(y)]^2),$$

where,

$$s(x) = x^4 - 2x^3 + x^2, \ g(y) = y^4 - y^2,$$

$$S(x) = \int s(x)dx, \ S_1(x) = s(x)s''(x) - [s'(x)]^2,$$

$$S_2(x) = \int s(x)s'(x)dx, \ G_1(y) = g(y)g'''(y) - g'(y)g''(y).$$
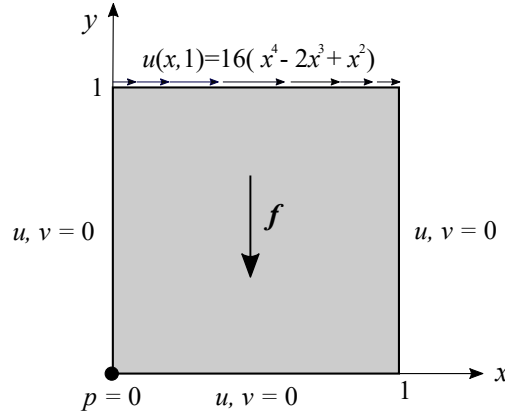
Figure 4.2: Geometry and boundary conditions of Test 02.

We emphasize that the analytical solution of the lid-driven cavity problem (Test 02) was studied by Shih *et al.*, (1989) [71] and Miller, (1995) [72] with a Newtonian fluid. The authors completed an extensive literature review and could not find examples of the analytical solution for the non-Newtonian case.

Now, we show the results in the following Tables (4.1-4.2) and Figure (4.3-4.5).

Table 4.1: Numerical errors in VEM and FEM solutions for the Newtonian case of Test 01.

	h	$error(\boldsymbol{u}, L^2)$	$error(p, L^2)$	rate $\boldsymbol{u}$	rate p
	1/5	6.6246e-03	6.5112e-02	-	-
	1/10	1.5409e-03	3.3630e-02	2.0344	0.9216
VEM	1/20	3.5612e-04	1.6726e-02	2.0526	0.9787
	1/40	9.5249e-05	8.4168e-03	1.8795	0.9788
	1/80	2.2340e-05	4.3348e-03	2.0807	0.9521
	1/5	6.5697e-03	6.2261e-02	-	-
	1/10	1.4730e-03	3.1442e-02	2.0857	0.9530
FEM	1/20	3.4180e-04	1.5874e-02	2.0470	0.9577
	1/40	8.9796e-05	7.8734e-03	1.9050	0.9993
	1/80	2.1753e-05	4.1653e-03	2.0343	0.9136
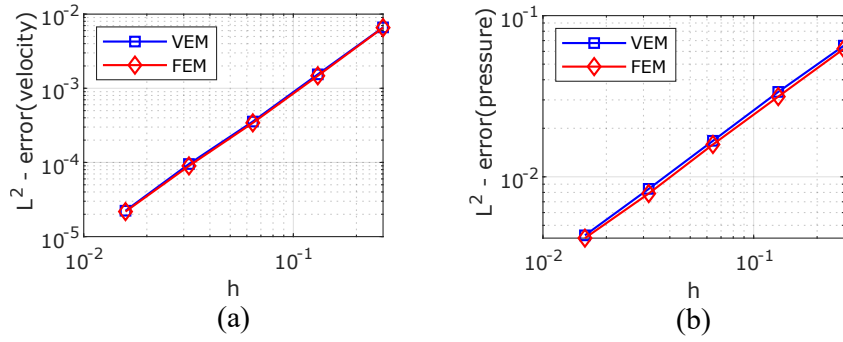
Figure 4.3: Convergence analysis for the Newtonian case of Test 01: (a) velocity and (b) pressure.

Table 4.2: Numerical errors in VEM and FEM solutions for the Newtonian case of Test 02.

	h	$error(\boldsymbol{u}, L^2)$	$error(p, L^2)$	rate $\boldsymbol{u}$	rate p
	1/5	4.0028e-02	6.3530e-01	-	-
	1/10	9.0208e-03	2.6784e-01	2.0413	1.1832
VEM	1/20	2.4766e-03	1.3542e-01	1.8185	0.9594
	1/40	6.3577e-04	6.5796e-02	1.9367	1.0281
	1/80	1.5330e-04	3.2459e-02	2.0434	1.0150
	1/5	4.0071e-02	6.7542e-01	-	-
	1/10	8.8597e-03	2.7234e-01	2.0675	1.2443
FEM	1/20	2.4280e-03	1.3613e-01	1.8210	0.9755
	1/40	6.2290e-04	6.5891e-02	1.9376	1.0335
	1/80	1.5116e-04	3.2614e-02	2.0343	1.0103
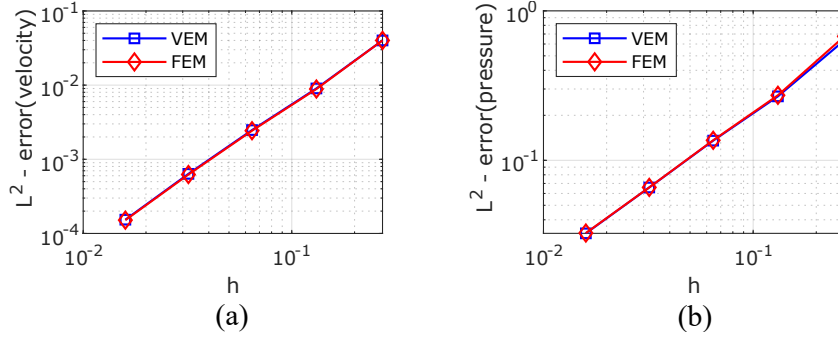
Figure 4.4: Convergence analysis for the Newtonian case of Test 02: (a) velocity and (b) pressure.
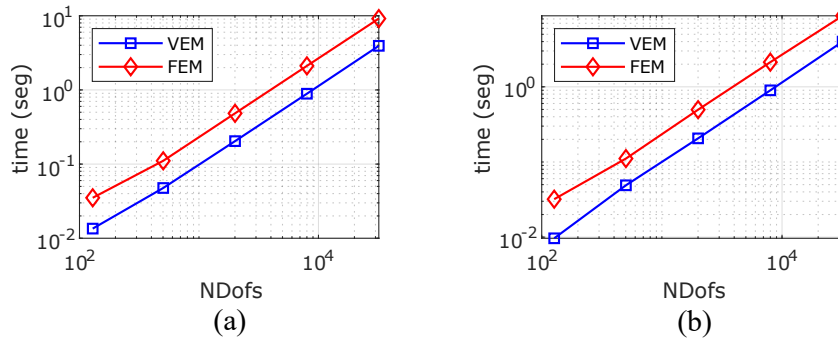
Figure 4.5: CPU time for the Newtonian case: (a) Test 01 and (b) Test 02.

4.3
Convergence tests using a non-Newtonian Carreau-Yasuda model fluid

Solution strategy:

Based on the analytical solution of Newtonian case of the Test 01 and Test 02, we take this solution $\{\boldsymbol{u}, p\}$, compute the gradient of the velocities and substitute them in the formulation of the Carreau-Yasuda model to obtain viscosity field, $\eta(\dot{\gamma})$. Next, we substitute in the formulation of the Navier-Stokes-Brinkman equation. The idea is to obtain the expression of the analytical load term $\boldsymbol{f}$ that satisfies this equations simultaneously. Then, this analytical formulation is set as the boundary condition in the numerical implementation in order to obtain the numerical velocity and pressure field's solution, respectively.

Test 01:
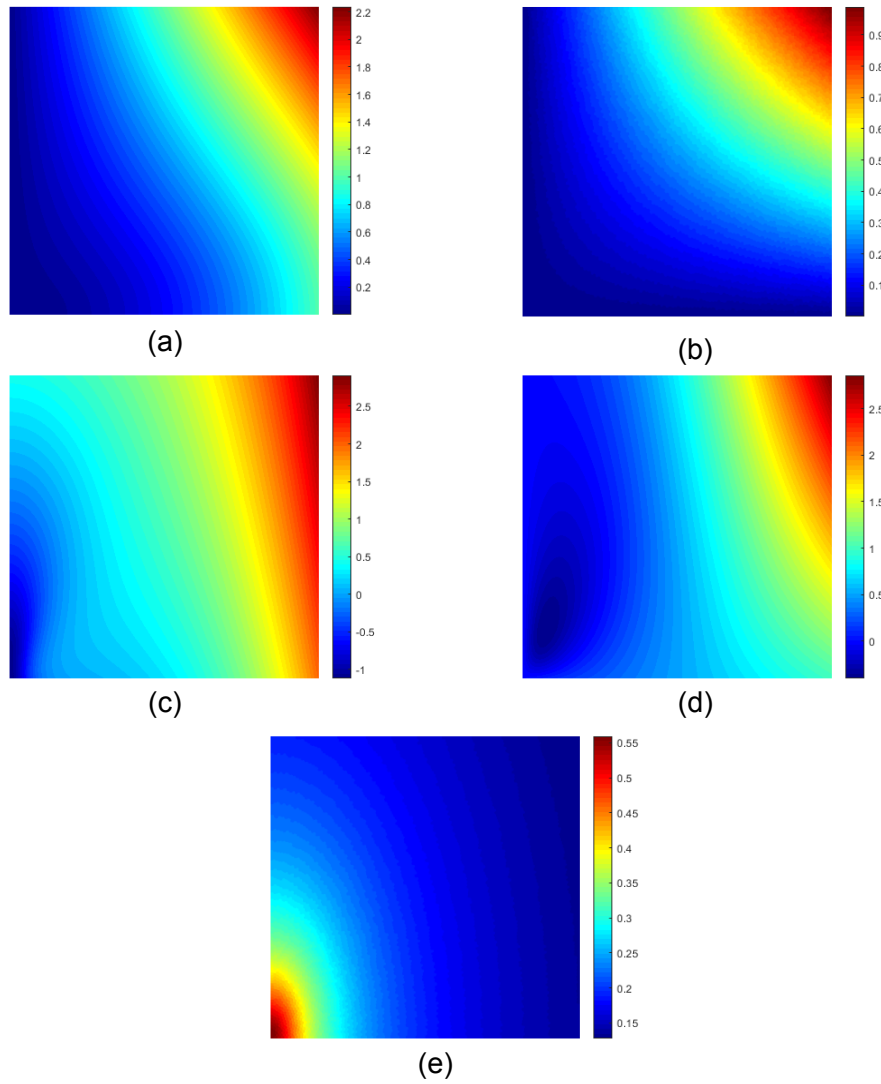
Figure 4.6: Graphics of the solution contour from Test 01: (a) velocity field, $\boldsymbol{u}$, (b) pressure field, p, (c) load field, f_x, (d) load field, f_y, and (e) viscosity field, $\eta(\dot{\gamma})$.

Figure 4.6 and 4.7 show the analytical solution of the velocity field, $\boldsymbol{u}$, and pressure field, p, of both domains (Test 01 and 02), and the load field, $\boldsymbol{f}$, and viscosity field, $\eta(\dot{\gamma})$, in the non-Newtonian Carreau-Yasuda model are shown in Figure 4.6(c-e) and 4.7(c-e), respectively.

Test 02:
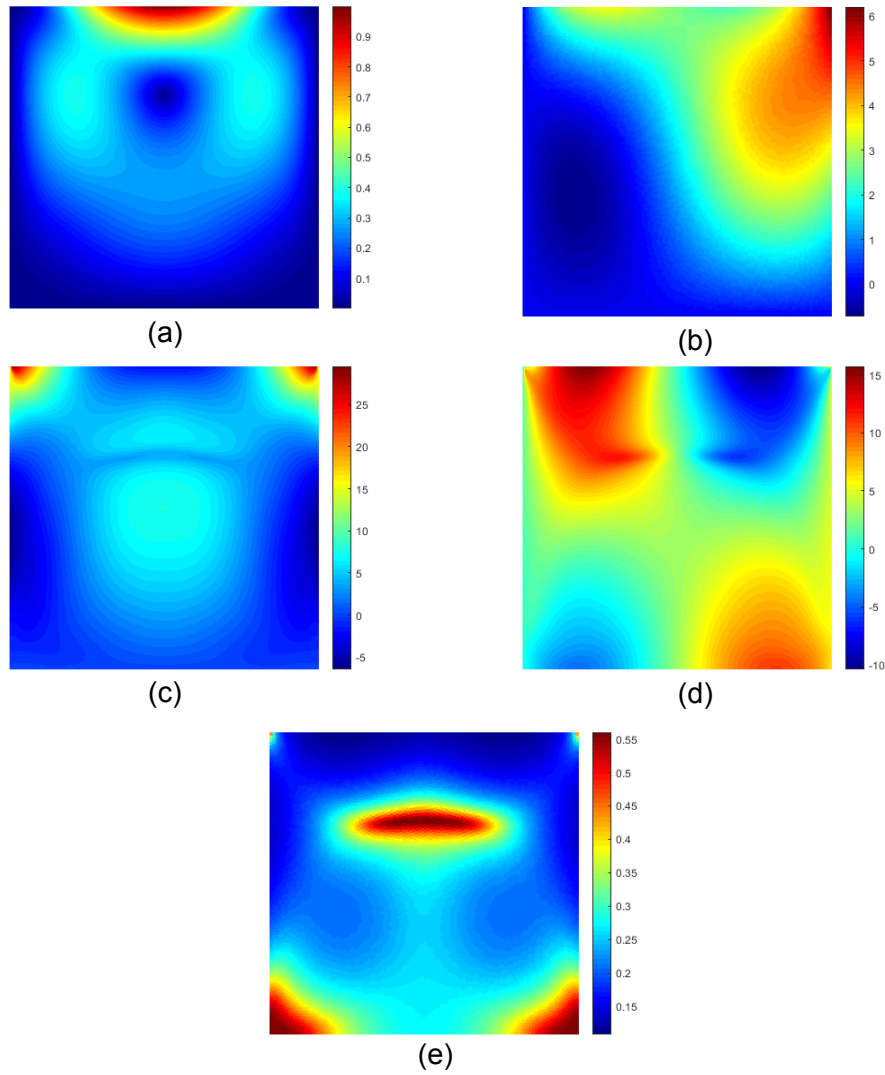
Figure 4.7: Graphics of the solution contour from Test 02: (a) velocity field, $\boldsymbol{u}$, (b) pressure field, p, (c) load field, f_x, (d) load field, f_y, and (e) viscosity field, $\eta(\dot{\gamma})$.

The numerical results of the Test 01 and 02, using the non-Newtonian Carreau-Yasuda model, are presented in Tables 4.3 and 4.4, respectively.

Table 4.3: Numerical errors in VEM and FEM solutions for the non-Newtonian Carreau-Yasuda case of Test 01.

	h	$error(\boldsymbol{u}, L^2)$	$error(p, L^2)$	rate $\boldsymbol{u}$	rate p
	1/5	6.6602e-03	6.4311e-02	-	-
	1/10	1.8453e-03	3.4526e-02	1.7529	0.8495
VEM	1/20	6.1407e-04	1.5777e-02	1.5637	1.1130
	1/40	1.9773e-04	9.0519e-03	1.6183	0.7934
	1/80	4.7168e-05	4.1826e-03	2.0627	1.1112
	1/5	7.2100e-03	6.3947e-02	-	-
	1/10	1.9753e-03	3.3757e-02	1.7683	0.8725
FEM	1/20	5.5944e-04	1.6251e-02	1.7928	1.0389
	1/40	1.9472e-04	9.1609e-03	1.5072	0.8186
	1/80	4.5955e-05	4.4236e-03	2.0781	1.0478
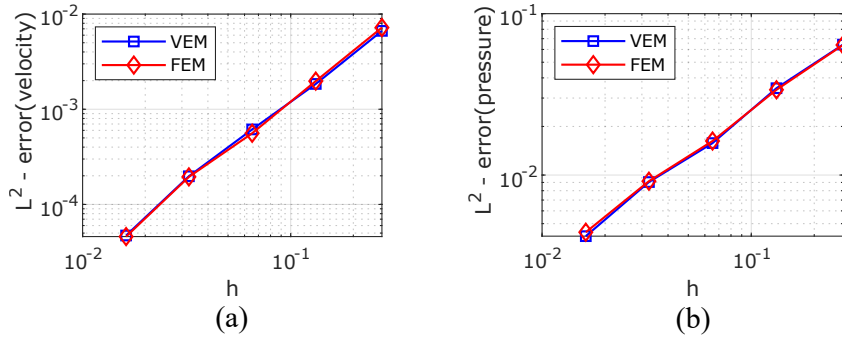
Figure 4.8: Test 01: Convergence analysis for the non-Newtonian case using polygonal meshes: (a) velocity and (b) pressure.

Table 4.4: Numerical errors in VEM and FEM solutions for the non-Newtonian Carreau-Yasuda case of Test 02.

|	h	$error(\boldsymbol{u}, L^2)$	$error(p, L^2)$	rate $\boldsymbol{u}$	rate p
	1/5	5.6431e-02	6.1986e-01	-	-
	1/10	1.7952e-02	3.0601e-01	1.5764	0.9716
	1/20	4.8547e-03	1.3799e-01	1.8306	1.1149
VEM	1/40	1.3795e-03	6.9057e-02	1.8090	0.9953
	1/80	3.8174e-04	3.3705e-02	1.8435	1.0292
	1/160	9.2862e-05	1.6281e-02	2.0338	1.0469
	1/5	5.2918e-02	5.5680e-01	-	-
	1/10	1.7655e-02	2.9584e-01	1.5109	0.8704
	1/20	3.8167e-03	1.3628e-01	2.1441	1.0850
FEM	1/40	1.0921e-03	6.8855e-02	1.7990	0.9816
	1/80	2.7728e-04	3.3972e-02	1.9670	1.0137
	1/160	6.9520e-05	1.6936e-02	1.9903	1.0015
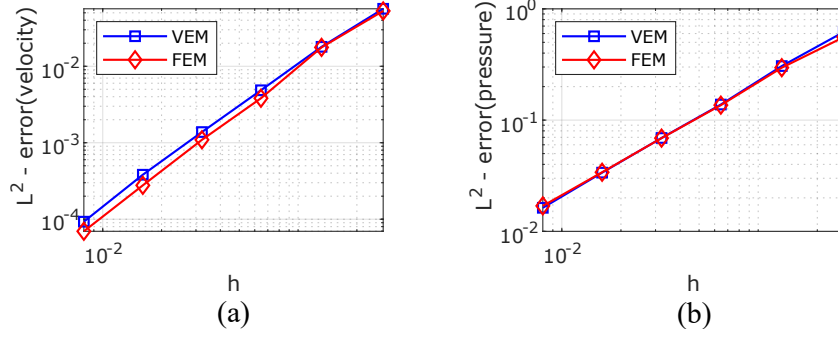
Figure 4.9: Convergence analysis for the non-Newtonian Carreau-Yasuda case of Test 02: (a) velocity and (b) pressure.
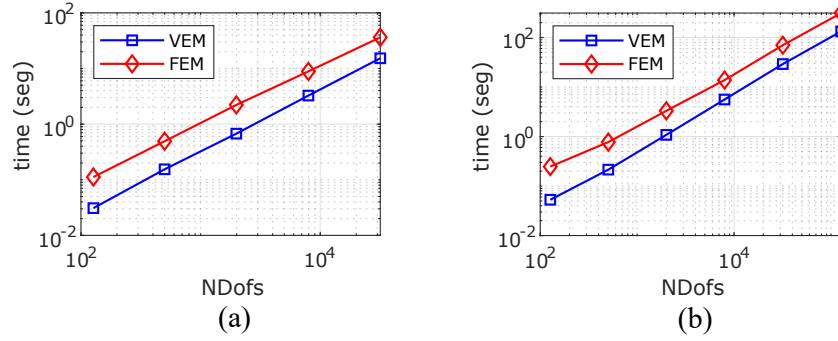

Figure 4.10: CPU time for the non-Newtonian Carreau-Yasuda case: (a) Test 01 and (b) Test 02.

Comments from the experimental tests:

Figures 4.3 and 4.4 (Newtonian case) and Figures 4.8 and 4.9 (non-Newtonian Carreau-Yasuda case) show the logarithm of the error norm as a function of the logarithm of the size polygonal element h. We remark that for linear elements, the error varies linearly with the size of the element, where in the velocity case, if the size of the element is reduced by half, the error decreases by a factor of 2, and for the pressure case, this factor is 1 (see Tables 4.1-4.4). We also remark that the numerical convergence presents a monotonic behavior and the results are stable for different sizes of polygonal elements.

Finally, from Figures 4.5 and 4.10, we show the computational time of the NVSB numerical solution (Test 01 and 02) against the number of DOFs to evaluate the computational performance of the VEM and FEM.

Therefore, the VEM method using lower-order polygonal elements proved to be very efficient in solving NVSB fluid flow problems, for both Newtonian and non-Newtonian Carreau-Yasuda model cases.

5
Topology optimization

In this Chapter, we discuss the topology optimization problem for the Navier-Stokes-Brinkman equation using the Carreau-Yasuda formulation as a non-Newtonian fluid model. In Section 5.1 we present the formulation of the objective and constraint functions, while in Section 5.2 we describe the material model interpolation used in this problem. In Section 5.3, we derive the sensitivities of the objective function with respect to the design variables, and finally in Section 5.4, we present the numerical implementation.

5.1
Formulation

We define an objective function, f, which is the minimization of the dissipative energy subject to the volume constraint function, g, of the optimization problem, as follows:

$$\begin{cases} \min_{x} \quad f = \dfrac{1}{2}\int_{\Omega} \eta(\dot{\gamma})\nabla \boldsymbol{u} : \nabla \boldsymbol{u} d\Omega + \dfrac{1}{2}\int_{\Omega} \overline{\alpha}(x)\boldsymbol{u}.\boldsymbol{u} d\Omega \\[2mm] \text{s.t.} \\[2mm] \qquad\qquad\qquad\qquad g = \int_{\Omega} x d\Omega - V \leq 0, \\[2mm] \text{with} \\[2mm] \qquad \begin{cases} -\eta(\dot{\gamma})\nabla^2 \boldsymbol{u} + \overline{\alpha}(x)\boldsymbol{u} + \nabla p + \rho \boldsymbol{u}.\nabla \boldsymbol{u} = \boldsymbol{0} \\[2mm] \qquad\qquad\qquad\qquad\qquad \nabla.\boldsymbol{u} = 0 \end{cases}, \\[2mm] \text{and} \\[2mm] \qquad\qquad\qquad\qquad 0 \leq x \leq 1. \end{cases} \quad (5\text{-}1)$$

We remark that the expression of the objective function is given neglecting any external forces on the fluid (such as gravitational and Coriolis forces). It has two terms, where the first term corresponds to dissipation due of the viscous dissipative effects and the second term is the porous media model. Term x represents the design variables for the optimization problem, and V is an upper bound for the final volume to be achieved in the solution.

The main steps of the topology optimization for non-Newtonian

Carreau-Yasuda fluid flow problems are shown in Figure 5.1, where, first of all, we discretized the fluid flow domain using polygonal meshes considering boundary conditions of velocity and pressure and parameters of the fluid. Then the Navier-Stokes-Brinkman system of equations and formulation of the non-Newtonian fluid (Carreau-Yasuda model) are solved using the VEM. The gradients of the objective and constraint functions are obtained analytically and used in the MMA - Method of Moving Asymptotes - (provided by K. Svanberg, (1987) [73], (1995) [74], (2002) [75] and implemented here in MATLAB®) as the optimizer to obtain the new design variables. Finally, we used a material model interpolation to obtain the fluid/solid distribution in all domains. The optimization process is completed when the optimal topology solution is achieved.
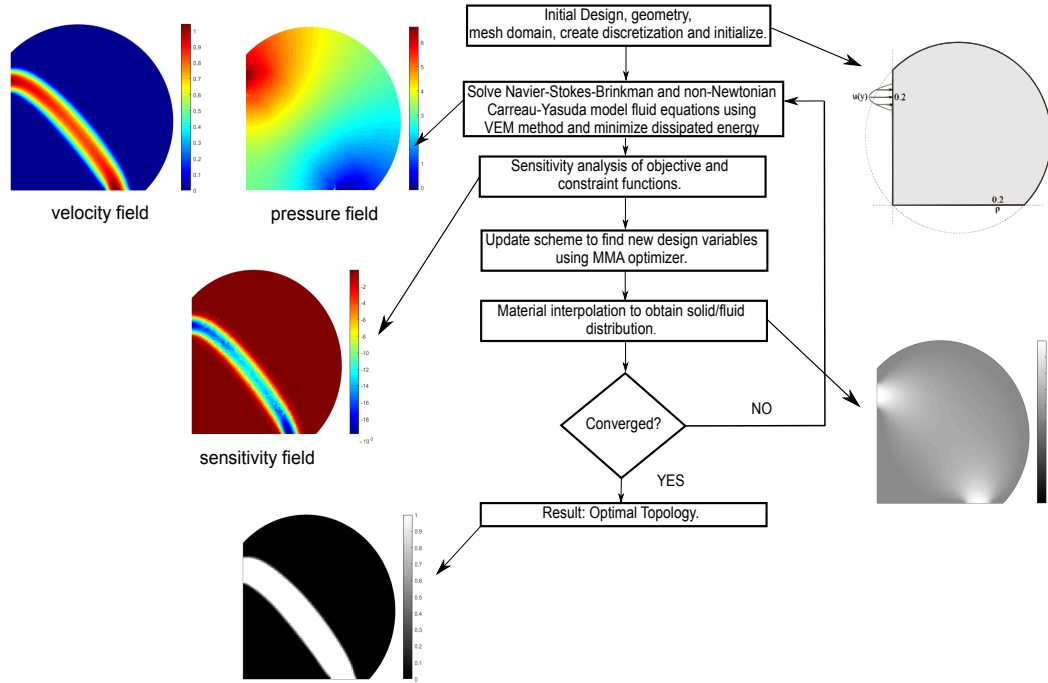

Figure 5.1: Flowchart for the optimal topology solution of the classic pipe-bending problem.

5.2
Material model interpolation

The scheme of the material model interpolation function, $\overline{\alpha}$, which depends on the design variable, x, is expressed as

$$\overline{\alpha}(x) = \alpha_U + (\alpha_L - \alpha_U)x\left[\frac{1+q}{x+q}\right],\qquad(5\text{-}2)$$

where the parameters $\alpha_U = 2.5\eta/0.01^2$ and $\alpha_L = 2.5\eta/100^2$ are defined as the upper and lower value of $\overline{\alpha}$, respectively, η is the viscosity of the fluid, and q is the penalization coefficient (Borrvall and Petersson, 2003) [1].

Note that when the design variable value ($x \approx 1$) we have that ($\overline{\alpha} = \alpha_L$) i.e., the behavior of the fluid is free flow. On the other hand, when the design variable value ($x \approx 0$) we have ($\overline{\alpha} = \alpha_U$), then the behavior of the fluid is restricted to solid regions. Figure 5.2 shows the behavior of the material model interpolation function of the design variable, x, and penalization coefficient, q.
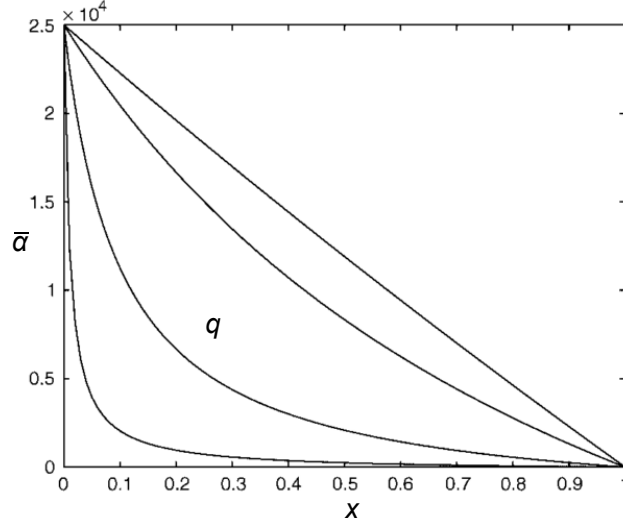
Figure 5.2: Material interpolation $\overline{\alpha}$, as a function of design variable field, x, for different values of the penalization coefficient, $q = \{0.01, 0.1, 1, 10\}$, [1].

5.3
Sensitivity analysis of the objective function

From Eq. (5-1), the objective function f, that corresponds to the minimization of the dissipative energy due to the effects of viscous and porous media, is expressed as:

$$f = \frac{1}{2}\boldsymbol{u}^T(\eta(\dot{\gamma})\boldsymbol{K}_\eta + \boldsymbol{K}_\alpha)\boldsymbol{u} = \frac{1}{2}\boldsymbol{z}^T\boldsymbol{C}\boldsymbol{z}. \tag{5-3}$$

where,

$$\boldsymbol{C} = \begin{bmatrix} \eta(\dot{\gamma})\boldsymbol{K}_\eta + \boldsymbol{K}_\alpha & 0 \\ 0 & 0 \end{bmatrix}, \tilde{\boldsymbol{K}} = \begin{bmatrix} \boldsymbol{C}(\boldsymbol{u}) + \boldsymbol{K}_\eta + \boldsymbol{K}_\alpha & -\boldsymbol{Q} \\ -\boldsymbol{Q} & 0 \end{bmatrix}, \boldsymbol{z} = \begin{bmatrix} \boldsymbol{u} \\ p \end{bmatrix}$$

Differentiating Eq. (5-3) with respect to the design variable x, we obtain the expression of the sensitivity of the objective function as:

$$\frac{\partial f}{\partial x} = \frac{1}{2}\left\{ \left(\frac{\partial \boldsymbol{z}}{\partial x}\right)^T \boldsymbol{C}\boldsymbol{z} + \boldsymbol{z}^T\frac{\partial \boldsymbol{C}}{\partial x}\boldsymbol{z} + \boldsymbol{z}^T\boldsymbol{C}\frac{\partial \boldsymbol{z}}{\partial x} \right\} = \frac{1}{2}\boldsymbol{z}^T\frac{\partial \boldsymbol{C}}{\partial x}\boldsymbol{z} + \boldsymbol{z}^T\boldsymbol{C}\frac{\partial \boldsymbol{z}}{\partial x}. \tag{5-4}$$

Now, from Eq. (2-7), the residual vector $\boldsymbol{R}$, is given by

$$\boldsymbol{R} = \tilde{\boldsymbol{K}}\boldsymbol{z} - \tilde{\boldsymbol{F}}, \tag{5-5}$$

where,

$$\tilde{\boldsymbol{K}} = \begin{bmatrix} \boldsymbol{C}(\boldsymbol{u}) + \boldsymbol{K}_\eta + \boldsymbol{K}_\alpha & -\boldsymbol{Q} \\ -\boldsymbol{Q} & 0 \end{bmatrix}, \quad \tilde{\boldsymbol{F}} = \begin{bmatrix} \boldsymbol{F} \\ \boldsymbol{0} \end{bmatrix}.$$

Deriving the residual vector $\boldsymbol{R}$, with respect to design variable x, we obtain

$$\frac{\partial \boldsymbol{R}}{\partial x} = \left.\frac{\partial \boldsymbol{R}}{\partial x}\right|_{\boldsymbol{z}=const} + \frac{\partial \boldsymbol{R}}{\partial \boldsymbol{z}}\frac{d\boldsymbol{z}}{dx} = 0, \tag{5-6}$$

where the first term represents the explicit dependence on the design variable and the second term is the implicit dependence on the vector $\boldsymbol{z}$. The explicit part is obtained by deriving the first term of Eq. (5-5), as follows:

$$\left.\frac{\partial \boldsymbol{R}}{\partial x}\right|_{\boldsymbol{z}=const} = \frac{\partial \tilde{\boldsymbol{K}}}{\partial x}\boldsymbol{z} - \frac{\partial \tilde{\boldsymbol{F}}}{\partial x} = \boldsymbol{r} \tag{5-7}$$

considering that the force vector $\tilde{\boldsymbol{F}}$ does not depend on the design variable x; therefore, $\frac{\partial \tilde{\boldsymbol{F}}}{\partial x}$ is zero. The Eq. (5-7), is re-written as

$$\left.\frac{\partial \boldsymbol{R}}{\partial x}\right|_{\boldsymbol{z}=const} = \frac{\partial \tilde{\boldsymbol{K}}}{\partial x}\boldsymbol{z}. \tag{5-8}$$

Substituting Eq. (5-8) and Jacobian matrix $\boldsymbol{J} = \frac{\partial \boldsymbol{R}}{\partial \boldsymbol{z}}$ into Eq. (5-6), we isolate the term $\frac{d\boldsymbol{z}}{dx}$ and we obtain:

$$\frac{d\boldsymbol{z}}{dx} = -\boldsymbol{J}^{-1}\left.\frac{\partial \boldsymbol{R}}{\partial x}\right|_{\boldsymbol{z}=const} = -\boldsymbol{J}^{-1}\frac{\partial \tilde{\boldsymbol{K}}}{\partial x}\boldsymbol{z}. \tag{5-9}$$

Finally, by substituting Eq. (5-9) into Eq. (5-4), the general expression of the sensitivity of the objective function, f, is expressed as

$$\frac{\partial f}{\partial x} = \frac{1}{2}\boldsymbol{z}^T\frac{\partial \boldsymbol{C}}{\partial x}\boldsymbol{z} - \boldsymbol{S}^T\frac{\partial \tilde{\boldsymbol{K}}}{\partial x}\boldsymbol{z}, \tag{5-10}$$

where $\boldsymbol{S}^T = \boldsymbol{z}^T\boldsymbol{C}\boldsymbol{J}^{-1}$ and $\boldsymbol{J}$ is the Jacobian matrix. The vector $\boldsymbol{S}$ is obtained by solving the system of equations $\boldsymbol{J}^T\boldsymbol{S} = \boldsymbol{C}\boldsymbol{z}$ at each step of the optimization process.

We remark that from Eq.(5-10), the sensitivities of $\frac{\partial \boldsymbol{C}}{\partial x}$ and $\frac{\partial \tilde{\boldsymbol{K}}}{\partial x}$ only depend on the sensitivity of the matrix $\boldsymbol{K}_\alpha$, where $\frac{\partial \boldsymbol{K}}{\partial x} = \frac{\partial \overline{\alpha}}{\partial x}\boldsymbol{K}_\alpha$. Therefore, the sensitivity of the objective function only depends of the term that contains the parameter $\overline{\alpha}$ (i.e., $\tilde{\boldsymbol{K}}_\alpha = \overline{\alpha}\boldsymbol{K}_\alpha$).

Re-writing Eq. (5-10), we obtain:

$$\frac{\partial f}{\partial x} = \frac{1}{2}\boldsymbol{u}^T\frac{\partial \overline{\alpha}}{\partial x}\boldsymbol{K}_\alpha\boldsymbol{u} - \boldsymbol{S}^T\frac{\partial \overline{\alpha}}{\partial x}\boldsymbol{K}_\alpha\boldsymbol{u}, \tag{5-11}$$

where, from the expression of the $\overline{\alpha}$, Eq. (5-2), the sensitivity expression $\overline{\alpha}$ with respect to design variable, x, is:

$$\frac{\partial \overline{\alpha}}{\partial x} = (\alpha_L - \alpha_U)q\left[\frac{1+q}{(x+q)^2}\right].$$

5.4
Numerical implementation

According to Talischi, [15], `Polymesher` is a *"simple and robust MATLAB® code for polygonal mesh generation. The main ingredients of Polymesher are the implicit representation of the domain and the use of Centroidal Voronoi diagrams for its discretization. The implicit description offer great flexibility to construct a relatively large class of domains with algebraic expressions. A discretization of the domain is constructed from a Centroidal Voronoi tessellation (CVT) that incorporates an approximation to its boundary. This approximation is obtained by including the set of reflections of the seeds. Additionally, Lloyd's method is used to establish a uniform (optimal) distribution of seeds and thus a high quality mesh (for more details, see reference (Talischi et al., 2012) [15]). Figure 5.3 shows some iterations of the Lloyd's method".*

<div style="text-align:center">(a)   (b)   (c)</div>
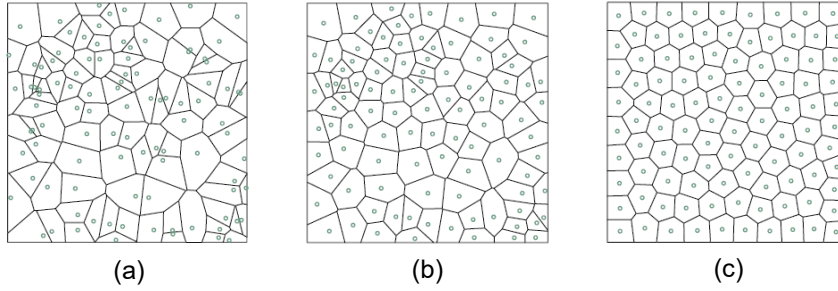
Figure 5.3: Lloyd's method. (a) initial random distribution of seeds and corresponding Voronoi diagram, (b) first iteration, and (c) distribution of seeds after 80 iterations [15].

To generate a mesh using `Polymesher` the user needs to provide the following informations: the `Domain` function (e.g. DoublePipe, PipeBend ChannelFlow, etc.) maximum number of Lloyd's iterations (`MaxIter`), and number of polygonal elements (`NElem`). The command line to call the `Polymesher` function is the following:

```
[Node,Element]=Polymesher[@Domain,NElem,MaxIter].
```

The corresponding output data are `Node`, a vector with the coordinates of all nodes in the mesh and `Element`, a cell array containing the connectivity of each polygonal element, respectively.

`DomainBoundCond` is a function that contains the boundary conditions of the domain and `DofDriveJ` contains information of the degrees of freedom of the polygonal meshes.

`Polytop` is an efficient code developed in MATLAB® for structural topology optimization that includes a general finite element routine based on isoparametric polygonal elements. According to the authors (Talischi *et al.,* 2012b) [19] and from extension on Stokes-Darcy problems (Pereira *et al.,* 2016) [5], the code also features a modular structure in which the sensitivity analysis routine and the optimization algorithm are separated from the specific choice of topology optimization formulation.

Within this framework, FEM and sensitivity analysis routines were adapted and modified using the VEM and lower-order elements. The function `VEMAnalysis` contains formulations to solve the Navier-Stokes-Brinkman fluid flow problem using both Newtonian and non-Newtonian Carreau-Yasuda model fluids. It computes the element residue vector, `getelemR`, Jacobian element matrix, `getelemJ`, and assembles the global vector and matrix (`FormR,FormJ`), respectively. Then we obtain the numerical solution of the velocity and pressure fields by solving these systems of non-linear equations using the function `NewtonRapshon`.

`ObjectiveFnc` is the objective function, f, (e.g. dissipative energy) and `ConstraintFnc` is the constraint function, g, (e.g. volume fraction). These are used during the sensitivity analysis in the function called `SensitivityAnalysis` that computes the gradients, ∇f and ∇g, of the objective function and constraint function, respectively. Note that other formulations can be used and thus the code can be extended, developed, and modified according to the type of problem.

The variables are updated in the MATLAB® `mmasub` routine using the method of moving asymptotes as the main optimizer algorithm, where the objective, constraint, and gradient functions are used. Then, the material interpolation function `MatIntFnc` is used to obtain the solid-fluid distribution in the domain fluid flow.

The main functions required to achieve an optimal topology for a fluid flow problem are illustrated in the code structure depicted in Figure 5.4.
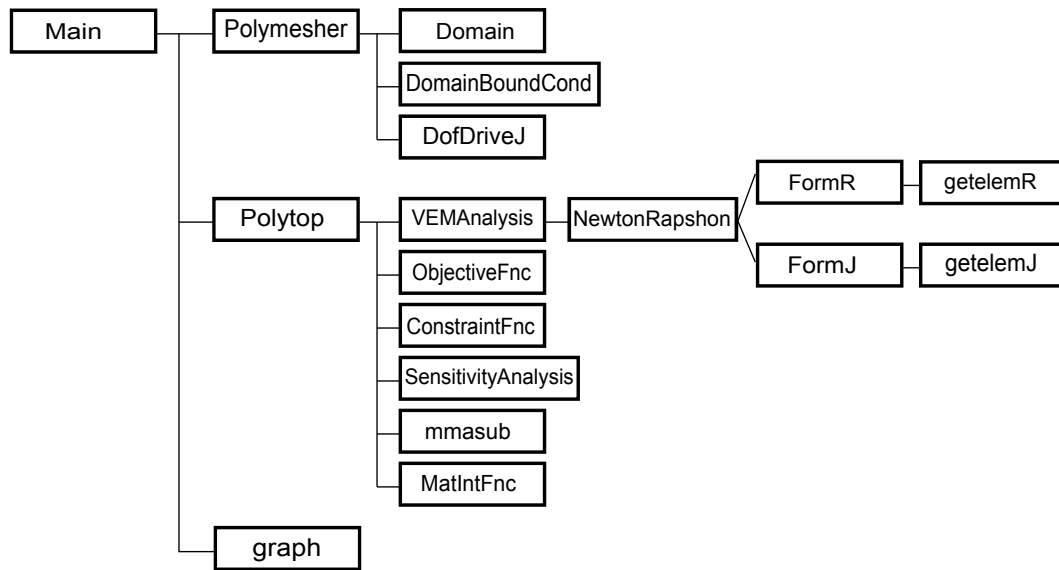
Figure 5.4: Structure of the VEM code implementation.

6
Results and discussion

In this Chapter, we present numerical results applied to optimal topology for fluid flow problems using the proposed VEM with polygonal and non-convex meshes. In Section 6.1 we show the problem of minimization of dissipative energy for the Stokes-Darcy problems, and in Section 6.2 we solve topology optimization problems governed by the Navier-Stokes-Brinkman equation, considering both cases of the Newtonian and non-Newtonian (Carreau-Yasuda model) fluids.

6.1
Optimal topology by Stokes-Darcy fluid flow

We present numerical examples of the typical diffuser, pipe-bend, and double pipe-bend problems (studied by Pereira et al. (2013) [76], (2016) [5] using FEM and polygonal meshes). We used the optimality criteria method (OC) as the optimizer (Groenwold and Etman, 2008) [77]. Some examples were presented in the work by (Suárez et al., 2018) [14] and we added others problems in this work using VEM method as follows.

Diffuser problem

In this typical problem, we present numerical examples of Cartesian and non-Cartesian domains (see Figures 6.1(a) and 6.2(a)) using polygonal elements. The boundary conditions are set as a parabolic velocity inlet $u_{inlet} = 3$ and outlet $u_{outlet} = 1$. The other parameters are shown in Table 6.1.

Table 6.1: Parameters used by the diffuser numerical problem (Cartesian and non-Cartesian domain).

	cartesian	*non-cartesian*
volume fraction	$V = 0.5$	$V = 0.4608473$
viscosity	$\mu = 1$	
number of element	10, 000	
penalty of parameters	$q = \{0.01; 0.1; 1\}$	
optimizer type	OC	
number max Iter.	150	

Figure 6.1: (a) Geometry and boundary conditions for the diffuser (Cartesian domain), (b) optimal topology, (c) velocity field, (d) pressure field, and (e) convergence history [14].
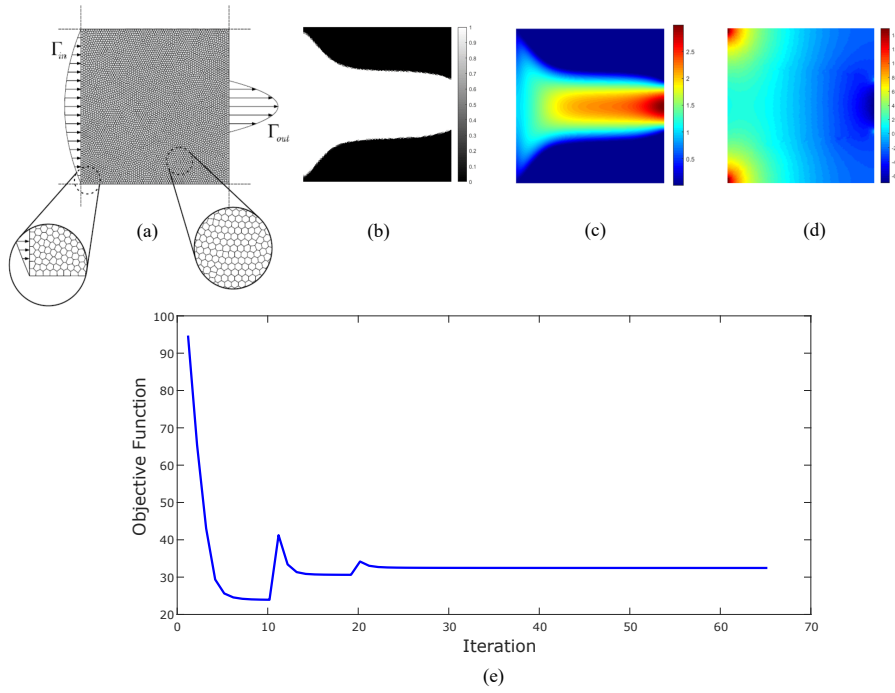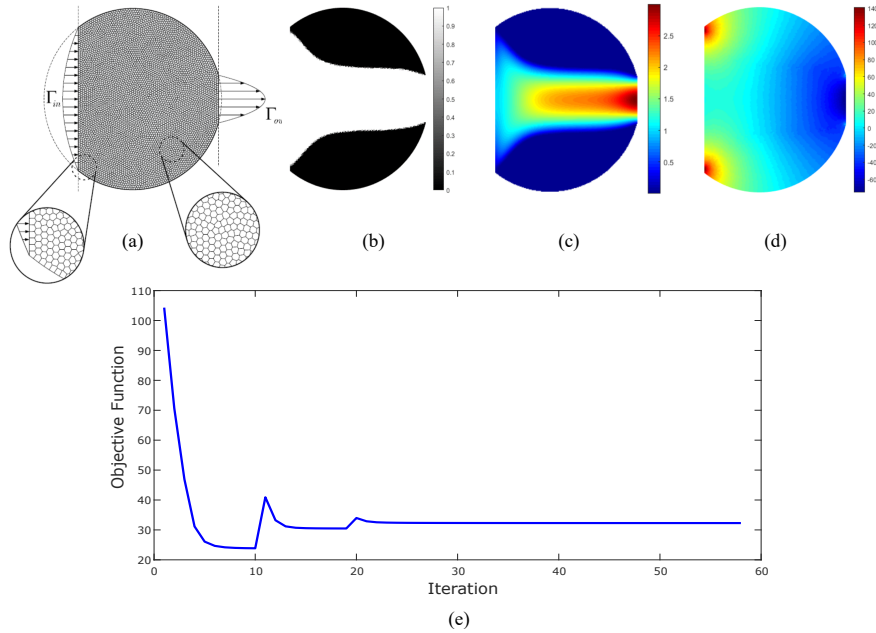

Figure 6.2: (a) Geometry and boundary conditions for the diffuser (non-Cartesian domain), (b) optimal topology, (c) velocity field, (d) pressure field, and (e) convergence history [14].

The solution for the curved domain was obtained for a volume fraction $V = 0.4608473$ (see Figure 6.2(b)) to match the solution for the square domain,

where $V = 0.5$ (see Figure 6.1(b)), as prescribed by Borrvall and Petersson, (2003) [1]. The convergence histories of the objective function, f, are shown in Figures 6.1(e) and 6.2(e).

Pipe-bend problem

In the typical pipe-bend problem, we present numerical examples of Cartesian and non-Cartesian domains (see Figures 6.3(a) and 6.4(b)) using polygonal elements. The boundary conditions are set as parabolic velocity inlet $u_{inlet} = 1$ and outlet $u_{outlet} = 1$. The other parameters are shown in Table 6.2.

Table 6.2: Parameters used by the pipe-bend numerical problem (Cartesian and non-Cartesian domain).

	cartesian	*non-cartesian*
volume fraction	$V = 1/3$	$V = 0.08\pi$
viscosity	$\mu = 1$	
number of element	10,000	
penalty of parameters	$q = \{0.01; 0.1; 1\}$	
optimizer type	OC	
number max Iter.	150	

The solution for the curved domain was obtained for a volume fraction $V = 0.08\pi$ (see Figure 6.4 (b)) to match the solution for the square domain, where $V = 1/3$ (see Figure 6.3 (b)), as prescribed by Borrvall and Petersson, (2003) [1]. The convergence histories of the objective function, f, are shown in Figures 6.3(b) and 6.4(b).

Figure 6.3: (a) Geometry and boundary conditions for the pipe-bend (Cartesian domain), (b) optimal topology, (c) velocity field, (d) pressure field, and (e) convergence history.
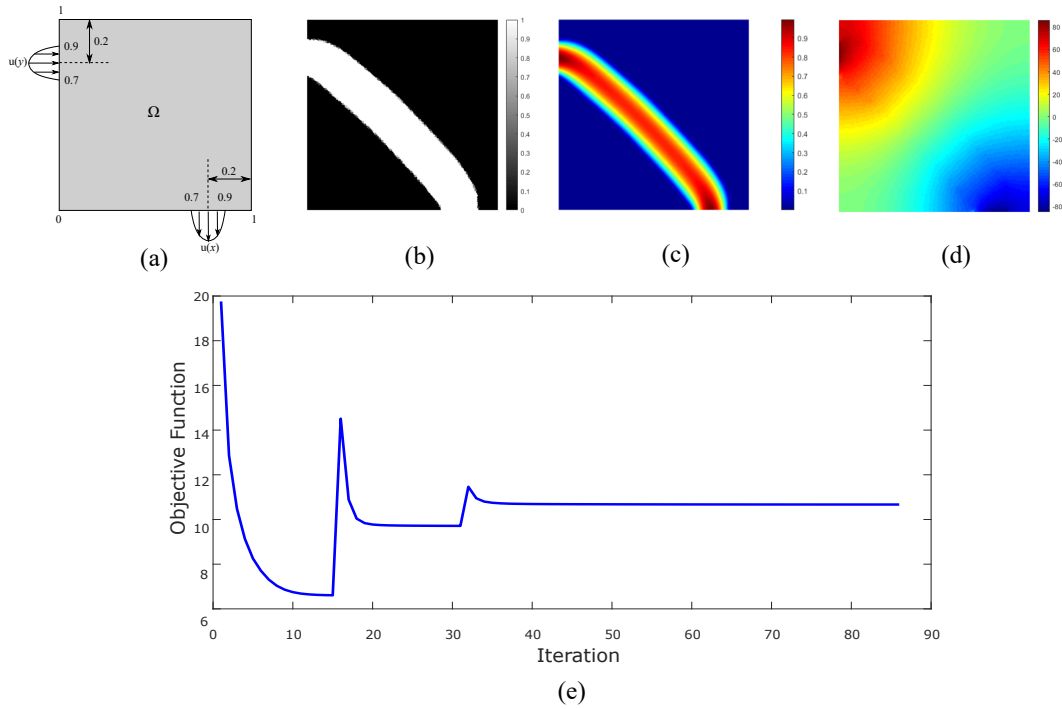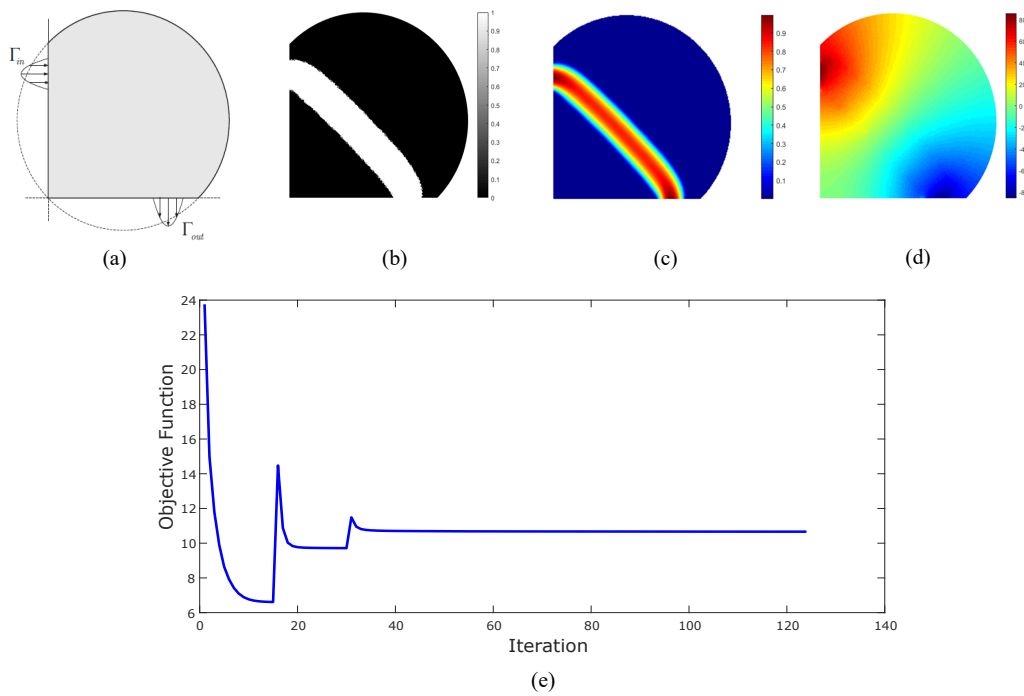

Figure 6.4: (a) Geometry and boundary conditions for the pipe-bend (non-Cartesian domain), (b) optimal topology, (c) velocity field, (d) pressure field, and (e) convergence history.

Double-pipe bend problem

Finally, in this problem, we present numerical examples in both domains of different length, δ, focused on non-convex element (tess12).
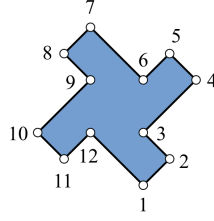
Figure 6.5: Tess12 non-convex element, [8].

The main parameters for the test are shown in Table 6.3.

Table 6.3: Parameters used by the double pipe-bend numerical problem.

length of the domain	$\delta = 1$	$\delta = 1.5$
volume fraction	$V = 1/3$	
viscosity	$\mu = 1$	
number of element	$10,000$	
penalty of parameters	$q = \{0.01; 0.1; 1\}$	
optimizer type	OC	
number max Iter	150	

The boundary conditions are set as parabolic velocity inlet and outlet as $u_1 = u_2 = 1$ for the both cases. Figures 6.6 (a) and (b) show the discretized domain using convex and non-convex (tess12) elements of length δ.
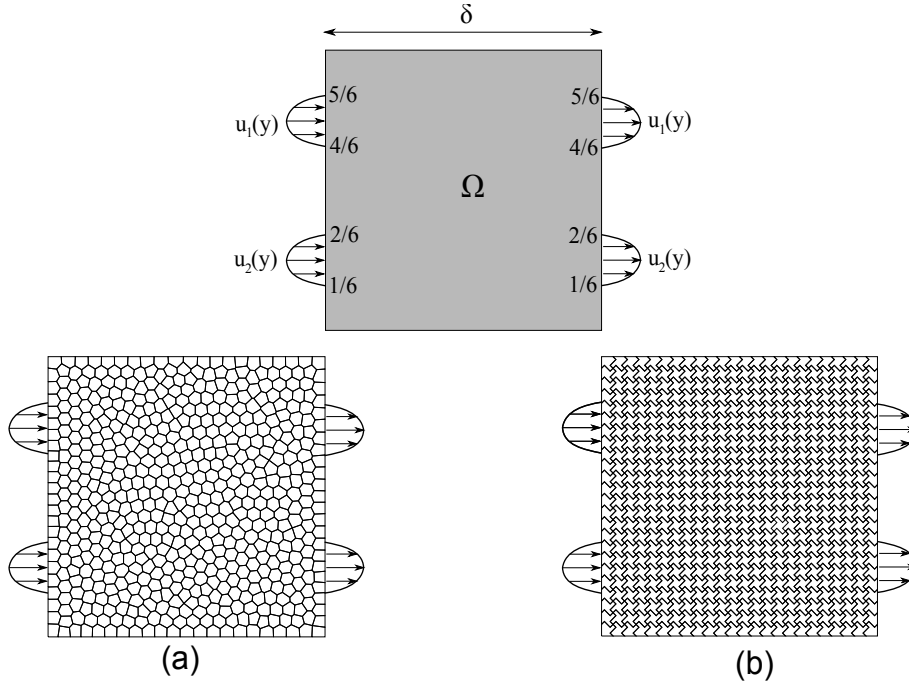
Figure 6.6: Geometry and boundary conditions for the double pipe by using (a) polygonal and (b) non-convex elements (tess12 element).

Two different solutions for the double pipe domain was obtained for a volume fraction $V = 1/3$ using a length of $\delta = 1$ and $\delta = 1.5$ by using convex (see Figure 6.7) and non-convex (see Figure 6.8) polygonal elements as prescribed by Borrvall and Petersson, (2003) [1].
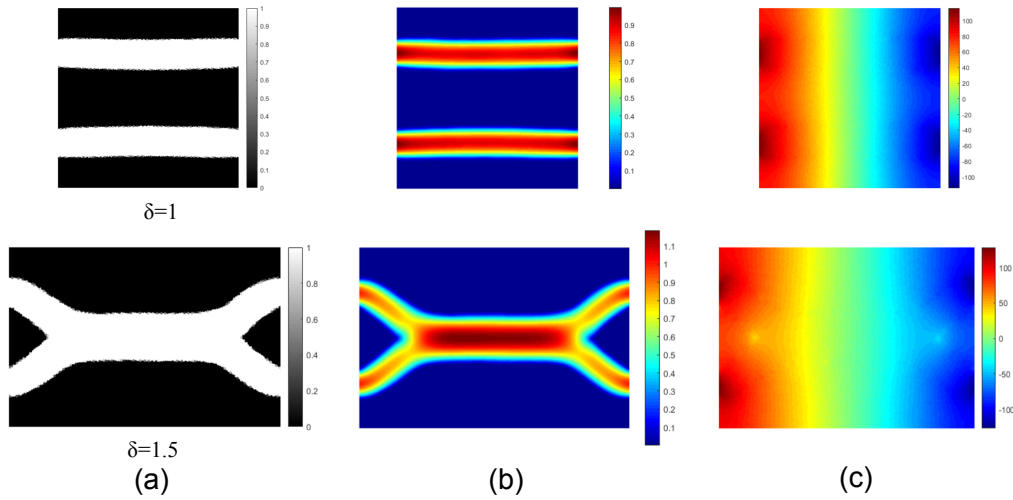
Figure 6.7: (a) Optimal topology, (b) velocity field, and (c) pressure field for the double pipe problem using convex polygonal elements, [14].
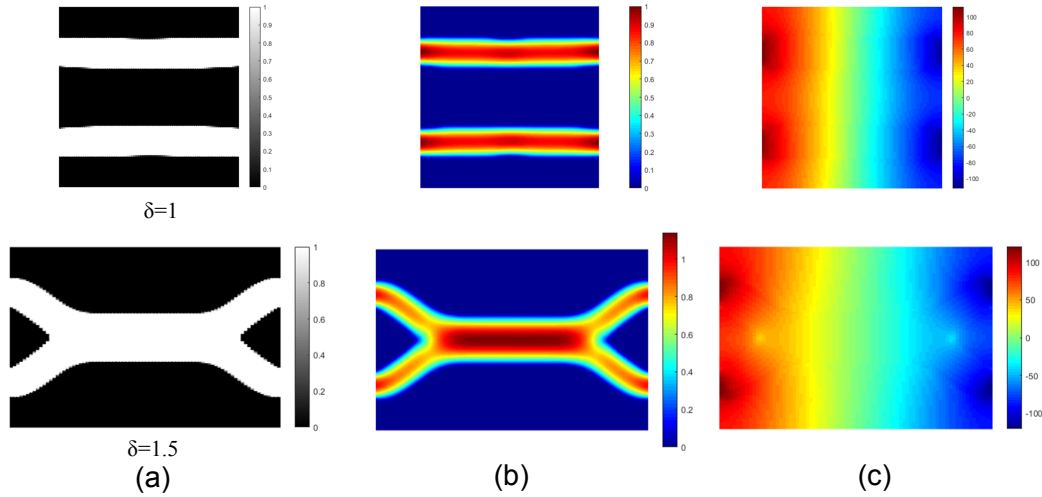
Figure 6.8: Optimal topology (a), velocity field (b) and pressure field (c) for the double pipe by using non-convex polygonal elements (tess12 element). [14]

Somme comments: The proposed VEM was used to solve Stokes-Darcy fluid-flow problems considering polygonal elements and it was integrated into the topology optimization framework. Classic problems as diffuser (see Figures 6.1-6.2), pipe-bend (see Figures 6.3-6.4), and double pipe bend problems (see Figures 6.7-6.8), considering cartesian and non-cartesian domains, were tested and the results obtained demonstrated that the computational time (computing/assemblig matrices + optimization convergence time) associated with the VEM was smaller when compared to the FEM. In addition, non-convex meshes, using tess12 elements were used to show the flexibility of the proposed method, (see Figure 6.8(a)).

6.2
Optimal topology for Navier-Stokes-Brinkman fluid flow

We present various numerical examples considering the minimization of dissipative energy due to the effects of viscous and porous media on blood fluid flow to obtain an optimal channel, focusing on both Newtonian and non-Newtonian (Carreau-Yasuda model) cases. We used the blood fluid properties described in in Table 2.1 of Section 2.1.2. The main parameters for the tests are shown in Table 6.4.

Table 6.4: Parameters used by topology optimization examples.

	Newtonian	*Carreau-Yasuda*
fluid parameters	$\mu = \eta_\infty$	*Table 2.1*
number of element	10,000	
penalty of parameters	$q = 0.1$	
optimizer type	MMA	
number max Iter	100	

Double channel problem

In this problem we considered the non-Newtonian (Carreau-Yasuda model) fluid case for the test, which was studied by Pingen and Maute (2010) [11]. The boundary conditions are set as a parabolic velocity inlet as $u_1 = u_2 = u$ and pressure outlet as $p = 0$. The solution was obtained using a volume fraction of $V = 1/3$ and we used the velocity inlet parameter, u, to increase or decrease the Reynolds number Re. From the results (see Figure 6.9(c)), we remark that for a high Reynolds number (i.e., $u \gg 1$, the optimal topology results obtained are similar to the ones from the Newtonian fluid case.
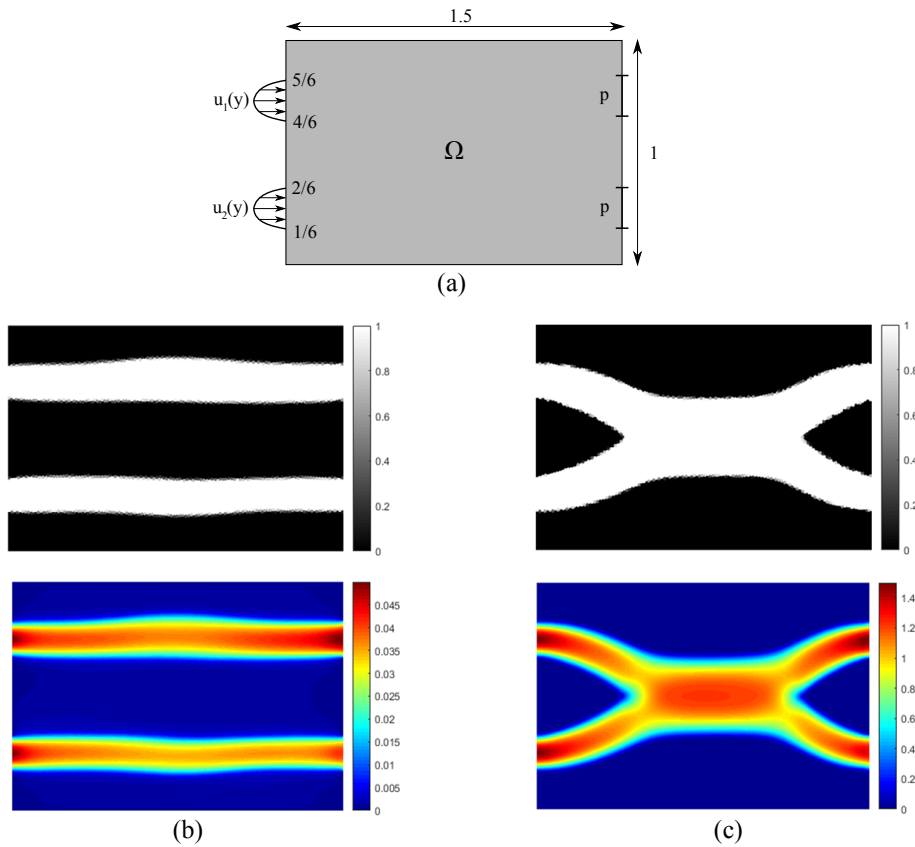

Figure 6.9: (a) Geometry and boundary conditions for the double channel problem; optimal topology for (b) low and (c) high Reynolds number, [16].

Pipe bend problem with obstacle

In the second example we considered both cases, Newtonian and non-Newtonian (Carreau-Yasuda model) fluid cases for the test, which was studied by (Kian, 2017) [12]. The details of the geometry and dimensions of the domain are shown in Figure 6.10(a). The boundary conditions are set as a parabolic velocity inlet as $u = 0.1$ and pressure outlet as $p = 0$. The solution was obtained using the volume fraction $V = 0.08\pi$. The optimal results are shown in Figure 6.10 for the Newtonian case (Figure 6.10(b)) and non-Newtonian (Carreau-Yasuda model) fluid case (Figure 6.10(c)).
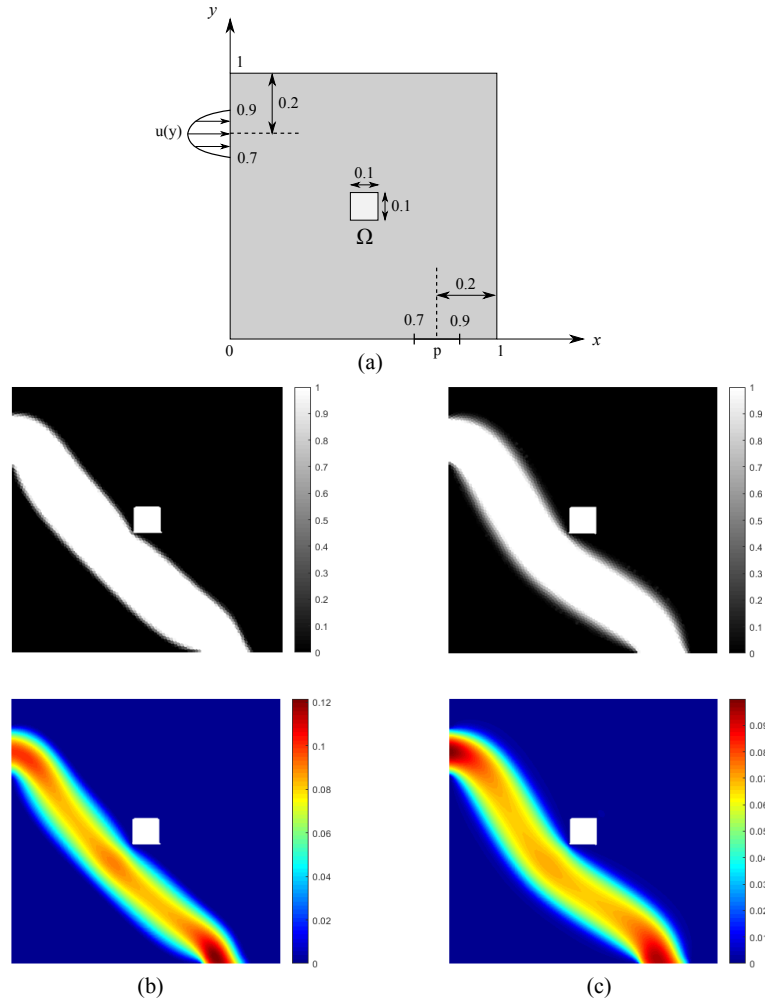
Figure 6.10: (a) Geometry and boundary conditions for the pipe bend problem with obstacle, and optimal topology and velocity field for (b) Newtonian and (c) non-Newtonian (Carreau-Yasuda model) [16].

Some comments: The double channel problem (Figure 6.7), was tested considered non-Newtonian fluid, where for lower velocities (low Reynolds number), the final configuration of the topology is similar to the results of the double-pipe Stokes problems, for the Newtonian case with a shorter domain

length (see Figure 6.7(a) with $\delta = 1$) and for high velocities (high Reynolds number), the configuration is similar to Newtonian case with a longer domain length (see Figure 6.7(b) with $\delta = 1.5$).

For the pipe bend problem with obstacle (see Figure 6.10), when the fluid flows under the obstacle, a slight difference is observed in the final topology of the optimized channel; in the non-Newtonian case (Figure 6.10(b)), the trend is more curved than in the Newtonian case (Figure 6.10(c)), this is due to the low velocities, where the Reynolds number is also low.

Now, we present examples of the optimal arterial graft design domain studied by Zhang and Liu, (2015) [42]. We defined the Reynolds number as $Re = \rho V_{max} L_{inlet}/\eta_\infty$, where V_{max} and L_{inlet} are the maximum value of the velocity inlet and length of the fluid inlet, respectively. The gray region represents the design domain and other regions of the domain are fixed in the optimization process, as follows.

In the following examples, we present optimal arterial grafts design domains for the minimization of the viscous drag of the blood fluid flow, studied by , and illustrated in Figures 6.11a, 6.12a and 6.13a.

Graft design for a blocked artery

Detail of the dimensions are shown in Figure 6.10(a) where, $h = 0.8$, $d = 0.64$, $l_1 = 6$, $l_2 = 3$, $l_3 = 1.9$, $l_4 = d/4$ and $l_5 = l_1 - l_2 + d/2$. The volume fraction is 33% of the total volume. The Reynolds number is $Re = 60$. The results for the velocity field and optimal topology are shown in Figure 6.11 for the Newtonian (Figure 6.11 (b)) and non-Newtonian fluid (Figure 6.11 (c)) cases.

Figure 6.11: (a) Geometry and boundary conditions for the arterial bypass design problem, velocity field corresponding to the optimal design topology for (b) Newtonian and (c) non-Newtonian (Carreau-Yasuda model) fluid cases [16]

Arterial bypass design for a stenosed artery

The optimal design of the joint section between the host and the graft artery is illustrated in Figure 6.12. The arterial bypass design domain has inlet velocities with values of $u_1 = u_2 = 2$ for both fixed and graft arteries, and pressure outlet $p = 0$, respectively. The solution was obtained for a volume fraction $V = 24\%$ of the total volume. The results for the velocity field and optimal topology are shown in Figure 6.11, for the Newtonian (Figure 6.12 (b)) and non-Newtonian fluid (Figure 6.12(c)) cases.
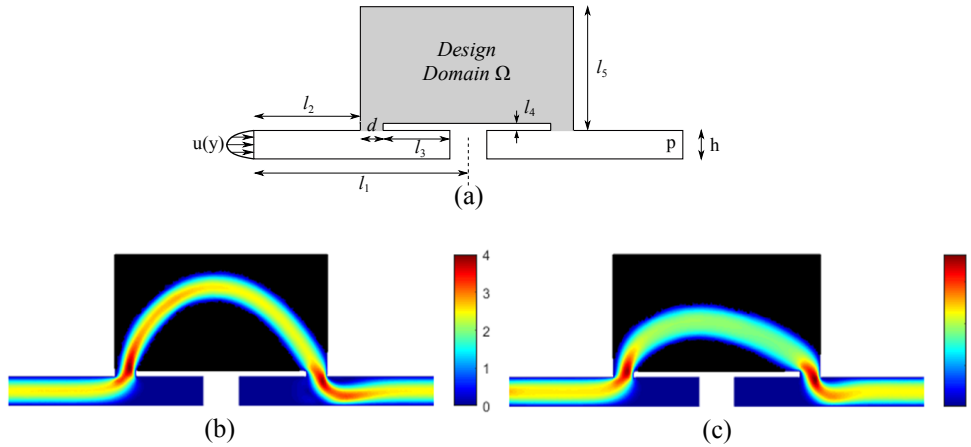

Figure 6.12: (a) Geometry and boundary conditions for arterial bypass design problem, velocity field corresponding to the optimal design topology for (b) Newtonian and (c) non-Newtonian (Carreau-Yasuda model) fluid cases [16].

Graft design for a stenosed artery

In this problem, we present the graft design for a stenosed artery, where the host artery is considered fixed and the graft artery is designed in the gray design domain (see Figure 6.13(a)). The prescribed parabolic inlet velocities for the host and graft arteries and pressure outlet are set to the same value as the previous example. The solution was obtained for a volume fraction $V = 0.10$ and Reynolds number $Re = 100$. The optimal topology and velocity field results for the Newtonian and non-Newtonian cases are shown in Figures 6.13(b) and (c).
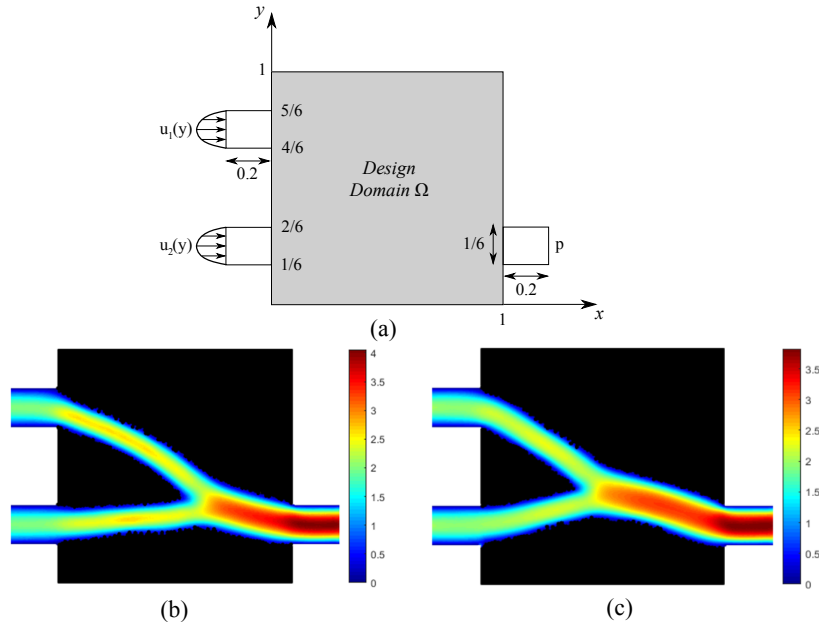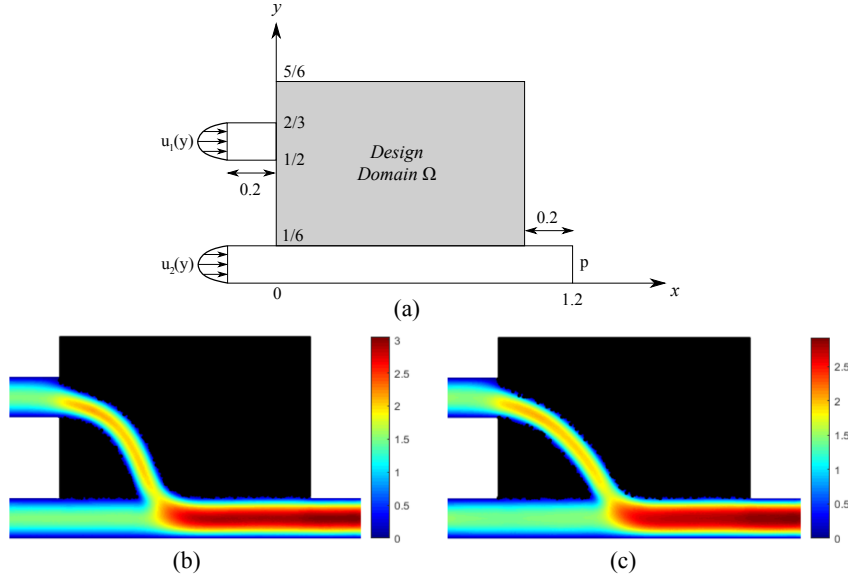
Figure 6.13: (a) Geometry and boundary conditions for the stenosed artery design problem, velocity field corresponding to the optimal design topology for (b) Newtonian and (c) non-Newtonian (Carreau-Yasuda model) fluid cases [16].

Horizontal channel flow with gravity

From the Eq. (5-1), the re-formulation of the objective function, f, (by minimizing dissipated energy) considering an external force vector, f, on the fluid, must be:

$$f = \frac{1}{2}\int_\Omega \eta(\dot{\gamma})\nabla\boldsymbol{u} : \nabla\boldsymbol{u}d\Omega + \frac{1}{2}\int_\Omega \overline{\alpha}(x)\boldsymbol{u}.\boldsymbol{u}d\Omega - \int_\Omega \boldsymbol{f}.\boldsymbol{u}d\Omega,$$

where, the third term represents the velocity maximization at the points of applied force (extracted from Koga, (2010) [2]).

We remark that the sensibility analysis of this additional term can be neglected as the load vector, $\boldsymbol{f}$, does not depend on the design variable, x. Therefore, for this type of problem, the objective gradient function formulation is similar to the expression shown in Eq. (5-11).

Finally, in this non-Newtonian fluid flow problem, studied by Deng et al.,(2013) [38], we presented a horizontal channel flow design that considers the influence of external forces on the fluid (such as gravity). The boundary conditions are set by an inlet velocity $u = 3$ and an outlet pressure $p = 0$ (see Figure (6.13)). The solution was obtained for a volume fraction $V = 0.40$ and a constant gravity vector $\boldsymbol{g} = [0, -10]$. The other parameters are given in Table 6.5.

Table 6.5: Parameters used by the horizontal channel flow with gravity problem.

	Carreau-Yasuda
fluid parameters	*Table 2.1*
number of element	$10,000$
penalty of parameters	$q = 4$
optimizer type	MMA
number max Iter	100
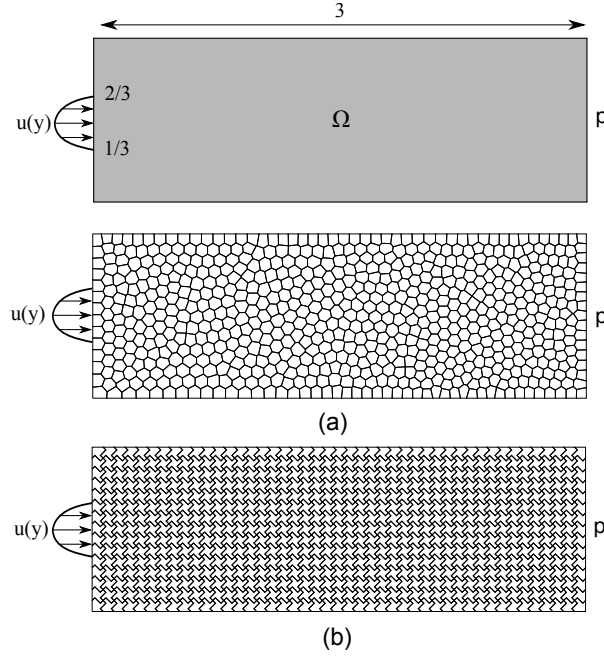
Figure 6.14: Geometry and boundary conditions for the horizontal channel flow domain by using (a) convex and (b) non-convex polygonal elements (tess12 element).

In the test, we use polygonal (Figure 6.14(a)) and non-convex (6.14(b)) meshes (tess12 element, see Figure 6.5). In both cases the optimal topology channel results bend to the direction of the gravity (see Figures 6.15(a) and 6.16(a)).
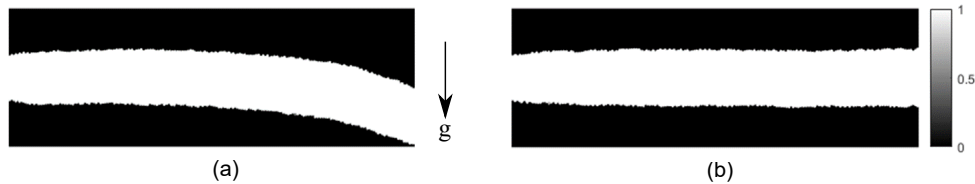
Figure 6.15: Optimized topologies of the horizontal channel (a) with or (b) without gravity using polygonal meshes.
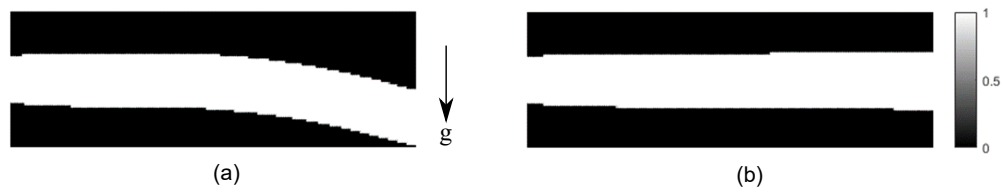
Figure 6.16: Optimized topologies of the horizontal channel (a) with or (b) without gravity using non-convex meshes (tess12 element).

7
Conclusions and extensions

7.1
Concluding remarks

In this work, we presented a topology optimization formulation for solving fluid flow problems considering both Newtonian (Stokes-Darcy and Navier-Stokes-Brinkman equations) and non-Newtonian (using Navier-Stokes-Brinkman equation and Carreau-Yasuda model for the blood flow) cases. The governing equations were solved numerically using the VEM in arbitrary two-dimensional domains discretized using polygonal meshes. Representative examples found in the literature were tested and a comparative study was developed between the FEM and VEM (considering lower-order elements). We showed that the VEM presented better computational performance, and that the VEM is very well suited for use in fluid flow topology optimization problems with complex domains using either convex or non-convex elements.

7.2
Suggestions for future work

The main suggestions for future research are:

- Extend the formulation to consider unsteady state of the Navier-Stokes equation for high Reynolds number;

- Extend the formulation to consider heat transfer problems for steady and unsteady states and combinate with the NVS equation;

- Present a study of convergence and computational time comparison with respect to the FEM method;

- Extend the formulation to consider multiphysics problems coupled with VEM using computational parallel techniques for large-scale problems;

- Extend the formulation to consider three-dimensional domains.

Bibliography

[1] BORRVALL, T.; PETERSSON, J.. **Topology optimization of fluids in stokes flow**. Journal of Numerical Methods, 41:77–107, 2003.

[2] KOGA, A.. **Projeto de dispositivos de microcanais utilizando o método de otimizaçao topológica**.

[3] TALISCHI, C.; PEREIRA, A.; GLAUCIO, P. ; MENEZES, I.. **Polygonal finite elements for incompressible fluid flow**. International Journal for Numerical Methods in Fluids, 74:134–151, 2014.

[4] PEREIRA, A.; TALISCHI, C.; M., M. I. F. ; GLAUCIO, P.. **Checkerboard-free topology optimization using polygonal finite elements**. In: ASOCIACION ARGENTINA DE MECANICA COMPUTACIONAL XXIX, MECOM 2010, p. 1525–1534, Buenos Aires, Argentina, 2010.

[5] PEREIRA, A.; TALISCHI, C.; PAULINO, G.H., M. I. ; CARVALHO, M.. **Fluid flow topology optimization in polytop:stability and computational implementation**. Structural and Multidisciplinary Optimization, 54:1345–1364, 2016.

[6] TORRES, A.. **Estudo comparativo de métodos numéricos para soluçao das equaçoes da elasticidade em problemas de otimizaçao topológica**.

[7] SUTTON, O. J.. **The virtual element method in 50 lines of matlab**. Numerical Algorithms, 75(4):1141–1159, 2017.

[8] PAULINO, G.; GAIN, A.. **Bridging art and engineering using escher-based virtual elements**. Structural and Multidisciplinary Optimization, 51(4):867–883, 2015.

[9] VEIGA, L.; BREZZI, F.; MARINI, L. ; RUSSO, A.. **The hitchhikerś guide to the virtual element method**. Mathematical Models and Methods in Applied Sciences, 24(8):1541–1573, 2014.

[10] BARBER, J.. **Elasticity**. Springer, 2010.

[11] PINGEN, G.; MAUTE, K.. **Optimal design for non-newtonian flows using a topology optimization approach**. Computers and Mathematics with Applications, 59:2340–2350, 2010.

[12] KIAN, J.. **Topology optimization method applied to design channels considering non-newtonian fluid flow.**

[13] Proceeding of the Comsol Conference Boston. **Newtonian and Non-Newtonian Blood Flow over a Backward- Facing Step-A Case Study**, 2009.

[14] SUÁREZ, M.; ROMERO, J. ; MENEZES, I.. **Topology optimization for fluid flow problems using the virtual element method.** In: ASOCIACION ARGENTINA DE MECANICA COMPUTACIONAL, MECOM 2018, p. 2037–2046, Tucumán, Argentina, 2018.

[15] TALISCHI, C.; PAULINO, G.; PEREIRA, A. ; MENEZES, I.. **Polymesher: a general-purpose mesh generator for polygonal elements written in matlab.** Structural and Multidisciplinary Optimization, 45(3):309–328, 2012.

[16] SUÁREZ, M.; ROMERO, J. ; MENEZES, I.. **On the virtual element method for topology optimization of non-newtonian fluid-flow problems,** (*to be submitted*). 2020.

[17] P., C.; A., K.. **An Introduction to Structural Optimization.** Springer, 2009.

[18] TALISCHI, C.; PAULINO, G.; PEREIRA, A. ; MENEZES, I.. **Polygonal finite elements for topology optimization: A unifying paradigm.** International Journal for Numerical Methods in Engineering, 82:671–698, 2010.

[19] TALISCHI, C.; PAULINO, G.; PEREIRA, A. ; MENEZES, I.. **Polytop: a matlab implementation of a general topology optimization framework using unstructured polygonal finite element meshes.** Structural and Multidisciplinary Optimization, 45(3):329–357, 2012.

[20] VEIGA, L.; LOVADINI, C. ; MORA, D.. **A virtual element method for elastic and inelastic problems on polytope meshes.** Computer Methods in Applied Mechanics and Engineering, 295(1):327–346, 2015.

[21] ARTIOLI, E.; VEIGA, L.; LOVADINI, C. ; SACCO, E.. **Arbitrary order 2d virtual elements for polygonal meshes.** Computational Mechanics, 60(3):355–377, 2017.

[22] TAYLOR, R.; ARTIOLI, E.. **VEM for inelastic solids.** Springer, In book: Advances in Computational Plasticity, 2018.

[23] GERSBORG-HANSEN, A.; SIGMUND, O. ; HABER, R.. **Topology optimization of channel flow problems**. Structural and Multidisciplinary Optimization, 30:181–192, 2005.

[24] GUEST, J.; PRÉVOST, J.. **Topology optimization of creeping fluid flows using a darcy-stokes finite element**. Journal of Numerical Methods, 66:461–484, 2006.

[25] BURMAN, E.; HANSBO, P.. **A unified stabilized method for stokes? and darcy?s equations**. J. Comput. Appl. Math., 198:35–51, 2007.

[26] VEIGA, L.; C., L. ; VACCA, G.. **Topology optimization of regions of darcy and stokes flow**. International Journal for Numerical Methods in Engineering, 69:1374–1404, 2007.

[27] CHALLIS, V.; GUEST, J.. **Level set topology optimization of fluids in stokes flow**. International Journal for Numerical Methods in Engineering, 79:1284–1308, 2009.

[28] WANG, S.; LIM, K. ; M.Y., W.. **An extended level set method for shape and topology optimization**. Journal of Computational Physics, 221:395–421, 2007.

[29] OKKELS, F.; OLESEN, L. ; BRUUS, H.. **Applications of topology optimization in the design of micro-and nanofluidic systems**. TechConnect Briefs, 1(4):575–578, 2005.

[30] OLESEN, L.; OKKELS, F. ; BRUUS, H.. **A high-level programming-language implementation of topology optimization applied to steady-state navier-stokes flow**. International Journal for Numerical Methods in Engineering, 65(4):975–1001, 2005.

[31] DENG, Y.; LIU, Z. ; WU, Y.. **Topology optimization of unsteady incompressible navier-stokes flow**. Journal of Computational Physics, 230:6688–6708, 2011.

[32] KREISSL, S.; PINGEN, G. ; MAUTE, K.. **An explicit level set approach for generalized shape optimization of fluids with the lattice boltzmann method**. International Journal for Numerical Methods in Fluids, 65:496–519, 2011.

[33] KREISSL, S.; PINGEN, G. ; MAUTE, K.. **Topology optimization for unsteady flow**. International Journal for Numerical Methods in Engineering, 87:1229–1253, 2011.

[34] CHEN, S.; DOOLEN, G.. **Lattice boltzmann method for fluid flows**. Annu. Rev. Fluid Mech, 30:329–364, 1998.

[35] KREISSL, S.; MAUTE, K.. **Levelset based fluid topology optimization using the extended finite element method**. Structural and Multidisciplinary Optimization, 46:311–326, 2012.

[36] CHESSA, J.; BELYTSCHKO, T.. **An extended finite element method for two- phase fluids**. J. Appl. Mech., 70:10–17, 2003.

[37] DENG, Y.; LIU, Z. ; WU, Y.. **Topology optimization of steady and unsteady incompressible navier-stokes flows driven by body forces**. Structural and Multidisciplinary Optimization, 47:555–570, 2013.

[38] DENG, Y.; LIU, Z.; WU, J. ; WU, Y.. **Topology optimization of steady navier-stokes flow with body force**. Computer Methods in Applied Mechanics and Engineering, p. 306–321, 2013.

[39] ROMERO, J.; SILVA, E.. **A topology optimization approach applied to laminar flow machine rotor design**. Comput. Methods Appl. Mech. Engrg., 279:268–300, 2014.

[40] SÁ, L.; NOVOTNY, A.; ROMERO, J. ; SILVA, E.. **Design optimization of laminar flow machine rotors based on the topological derivative concept**. Structural and Multidisciplinary Optimization, 56:1013–1026, 2017.

[41] HYUN, J.; WANG, S. ; YANG, S.. **Topology optimization of the shear thinning non-newtonian fluidic systems for minimizing wall shear stress**. Computers and Mathematics with Applications, 67:1154–1170, 2014.

[42] ZHANG, B.; LIU, X.. **Topology optimization study of arterial bypass configurations using the level set method**. Structural and Multidisciplinary Optimization, 51:773–798, 2015.

[43] ZHANG, B.; LIU, X. ; SUN, J.. **Topology optimization design of non-newtonian roller-type viscous micropumps**. Structural and Multidisciplinary Optimization, 53:409–424, 2016.

[44] ROMERO, J.; SILVA, E.. **Non-newtonian laminar flow machine rotor design by using topology optimization**. Structural and Multidisciplinary Optimization, 55:1711–1732, 2017.

[45] VEIGA, L.; BREZZI, F. ; MARINI, L.. **Virtual elements for linear elasticity problems**. SIAM Journal on Numerical Analysis, 51(2):794–812, 2013.

[46] GAIN, A.; TALISCHI, C. ; PAULINO, G.. **On the virtual element method for three-dimensional linear elasticity problems on arbitrary polyhedral meshes**. Comput. Methods Appl. Mech. Engrg., 282:132–160, 2014.

[47] ARTIOLI, E.; MIRANDA S., LOVADINI, C. ; PATRUNO, L.. **A stress/displacement virtual element method for plane elasticity problems**. Comput. Methods Appl. Mech. Engrg., 325(1):155–174, 2017.

[48] CHI, H.; VEIGA, L. ; PAULINO, G.. **Some basic formulations of the virtual element method (vem) for finite deformations**. Comput. Methods Appl. Mech. Engrg., 318:148–192, 2017.

[49] BREZZI, F.; MARINI, L.. **Virtual element methods for plate bending problems**. Comput. Methods Appl. Mech. Engrg., 253:455–462, 2013.

[50] WRIGGERS, P.; RUST, W. ; REDDY, B.. **A virtual element method for contact**. Computational Mechanics, 58:1039–1050, 2016.

[51] RIVERA, G.; MORA, D.. **A priori and a posteriori error estimates for a virtual element spectral analysis for the elasticity equations**. IMA Journal of Numerical Analysis, 2018.

[52] BENEDETTO, M.; CAGGIANO, A. ; ETSE, G.. **Applications of the virtual element method for cracking analysis of cement-based composites using interface element**. In: ASOCIACION ARGENTINA DE MECANICA COMPUTACIONAL, MECOM 2016, p. 08–11, Córdova, Argentina, 2016.

[53] ANTONIETTI, P.; VEIGA, L.; MORA, D. ; VERANI, M.. **A stream virtual element formulation of the stokes problem on polygonal meshes**. SIAM Journal on Numerical Analysis, 52(1):386–404, 2014.

[54] CANGIANI, A.; GYRYA, V. ; MANZINI, G.. **The non-conforming virtual element method for the stokes equations**. SIAM Journal on Numerical Analysis, 54(6):3411–3435, 2016.

[55] VEIGA, L.; LOVADINA, C. ; G., V.. **Divergence free virtual elements for the stokes problem on polygonal meshes**. ESAIM Mathematical Modelling and Numerical Analysis, 51(2):509–535, 2017.

[56] ERNESTO, C.; GATICA, G.. **A mixed virtual element method for the pseudostress-velocity formulation of the stokes problem**. IMA Journal of Numerical Analysis, 37:296–331, 2017.

[57] VEIGA, L.; LOVADINA, C. ; VACCA, G.. **Virtual elements for the navier-stokes problem on polygonal meshes**. SIAM Journal on Numerical Analysis, 56(3):1210–1242, 2018.

[58] GAIN, A.; PAULINO, G.; DUARTE, L. ; MENEZES, I.. **Topology optimization using polytopes**. Comput. Methods Appl. Mech. Engrg., 293:411–430, 2015.

[59] ANTONIETTI, P.; BRUGGI, M.; SCACCHI, S. ; VERANI, M.. **On the virtual element method for topology optimization on polygonal meshes: A numerical study**. SIAM Journal on Numerical Analysis, 74(1):1091–1109, 2017.

[60] GARTLING, D.; HICKOX, C. ; GIVLER, R.. **Simulation of coupled viscous and porous flow problems**. International Journal of Computational Fluid Dynamics, 7:23–48, 2007.

[61] R.L., B.; J.D., F.. **Numerical Analysis 9th**. Brooks-Cole, Cengage Learning, 2000.

[62] CARVALHO, S.; VALERIO, V.. **Introduction to the Finite Element Method: Application in Fluid Dynamics (*in portuguese*.** SBMAC, 2012.

[63] CHO, Y.; KENSEY, K.. **Effects of the non-newtonian viscosity of blood on flows in a diseased arterial vessel. part 1: Steady flows**. Biorheology., 28(3-4):241–62, 1991.

[64] ABRAHAM, F.; BEHR, M. ; HEINKENSCHLOSS, M.. **Shape optimization in steady blood flow: A numerical study of non-newtonian effects**. Computer Methods in Biomechanics and Biomedical Engineering, 8:127–137, 2005.

[65] AHMAD, B.; ALSAEDI, A.; BREZZI, F. ; L.D., M.. **Equivalent projectors for virtual element methods**. Comput. Math. with Appl., 66(3):376–391, 2013.

[66] VEIGA, L.; BREZZI, F. ; CANGIANI, A.. **Basic principles of virtual element methods**. Mathematical Models and Methods in Applied Sciences, 23(1):199–214, 2013.

[67] VEIGA, L.; BREZZI, F.; MARINI, L. ; RUSSO, A.. **Serendipity nodal vem spaces**. Comput. Fluids,, 141:2–12, 2016.

[68] BRENNER, S.; GUAN, Q. ; SUNG, L.. **Some estimates for virtual element methods**. Computational Methods in Applied Mathematics, 17(4):553–574, 2017.

[69] FISH, J.; BELYTSCHKO, T.. **A First Course in Finite Elements**. John Wiley and Sons Ltd, 2007.

[70] TALISCHI, C.; PAULINO, G. ; CHAU, H.. **Honeycom wachspress finite elements for structural topology optimization**. Struct Multidisc Optim, 37:596–583, 2009.

[71] SHIH, T.; TAN, C. ; HWANG, B.. **Effects of grid staggering on numerical schemes**. International Journal for Numerical Methods in Fluids, 9:193–212, 1989.

[72] MILLER, W.. **Flow in the driven cavity calculated by the lattice boltzmann method**. Physical Review E., 51(4):1013–1026, 1995.

[73] SVANBERG, K.. **The method of moving asymptotes-a new method for structural optimization**. International Journal for Numerical Methods in Engineering, 24:359–373, 1987.

[74] In Proceeding of the world congress of structural and multidisciplinary optimization, p. 9-16. **A Globally Convergent Version of MMA without Linesearch**, 1995.

[75] SVANBERG, K.. **A class of globally convergent optimization methods based on conservative convex separable approximations**. SIAM J. Optim., 12(2):555–573, 2002.

[76] PEREIRA, A.; TALISCHI, C.; CARVALHO, M. S.; M., M. I. F. ; GLAUCIO, P.. **Fluid topology optimization using polygonal finite elements**. In: CILAMCE 2013, p. 10–13, Pirenópolis, Brazil, 2013.

[77] GROENWOLD, A.; L.F.P., E.. **On the equivalence of optimality criterion and sequential approximate optimization methods in the classical topology layout problem**. Int. J. Numer. Methods Enginnering, 73:297–316, 2008.